Micronization by supercritical antisolvent precipitation processes

Valentina Prosapio

Unione Europea
REGIONE CAMPANIA
P.O.R. Campania FSE 2007-2013
La tua Campania cresce in Europa
UNIVERSITÀ DEGLI STUDI DI SALERNO

P.O. Campania FSE 2007/2013 - Dottorati in azienda

Department of Industrial Engineering

Ph.D. Course in Chemical Engineering
(XIV Cycle - New Series)

Thesis in Chemical Engineering

MICRONIZATION BY SUPERCRITICAL ANTISOLVENT PRECIPITATION PROCESSES

Supervisors
Prof. Ernesto Reverchon

Prof. Iolanda De Marco

Ph.D. student
Valentina Prosapio

Scientific Referees
Priv. Doz. Dr.-Ing. habil. Andreas Braeuer
Ing. Italo Spiotta

Ph.D. Course Coordinator
Prof. Paolo Ciambelli

Acknowledgements

This is probably the most difficult part of the thesis to be written. These three years were critical for my growth, not only from a scientific point of view but also from a personal one. Thanks to this path I overcome my insecurities and weaknesses and become a more confident person. During this process many people helped me, in different moments and different ways, so it’s time to say thanks to each of them!

First of all, I would like to thank Professor Ernesto Reverchon who, taking advantage of my pride and my determination, was able to bring out the best in me. His intelligence, intuition and critical skills were a source of inspiration, teaching me to do better and better and not to leave anything to chance.

A huge thanks goes to Iolanda De Marco, my essential reference point. She thought me to never give up, to look at the big picture and to always be a step ahead. In these years she was not only a valuable supervisor but above all a precious friend. She was always there when I need to be supported and encouraged. She was always on my side and for that I will never thank her enough.

Heartfelt thanks to Roberta, a colleague and a very special friend! During my Ph.D. she was my confidant, counselor and “by the hour diet” partner. She always listened and supported me patiently and gave me good advice with sincerity and sweetness. She was really an important figure for the scientific and personal dialogue, I don’t know how I would have done without her!

A special thanks to Mara, Emilia, Vincenzo, Marco, Miguel and Paolo, the best colleagues you could wish for! The period spent together was full of laughs, jokes and affection. Our genuine friendship is one of the most enjoyable gifts that I have had in these years and helped me to overcome many “bad times”. Thanks also to all the other members of this "supercritical" team: Mariarosa, Alessia, Renata, Giovanna, Stefano, Lucia and Rosita; each of them, in one way or another, taught me something.

I gratefully acknowledge Professor Andreas Braeuer for giving me the opportunity to be part of his research group during my stay in Erlangen and for his constructive advice. I would like also to thank Matthias and Daniel for the fruitful work made together and all the other Ph.D. students of SAOT for their kindness and availability.

A sincere thanks goes to my family for their unconditional love and for supporting me since ever! Without you I wouldn't be the person I am and I wouldn't come so far. I owe all to you!!!

Last, but by no means least, I am heartily thankful to my dear Nando for his love, his advice and constant support. He is my soul mate and meet him was the most beautiful thing in my entire life!!!

Publication list

International journals

1. I. De Marco, **V. Prosapio**, F. Cice, E. Reverchon, Use of solvent mixtures in supercritical antisolvent process to modify precipitates morphology: Cellulose acetate microparticles, The Journal of Supercritical Fluids 83 (2013) 153-160.
2. **V. Prosapio**, E. Reverchon, I. De Marco, Antisolvent micronization of BSA using supercritical mixtures carbon dioxide + organic solvent, The Journal of Supercritical Fluids 94 (2014) 189-197.
3. I. De Marco, M. Rossmann, **V. Prosapio**, E. Reverchon, A. Braeuer, Control of particle size, at micrometric and nanometric range, using supercritical antisolvent precipitation from solvent mixtures: application to PVP, Chemical Engineering Journal (2015) 344-352.
4. **V. Prosapio**, I. De Marco, M. Scognamiglio, E. Reverchon, Folic acid‑PVP nanostructured composite microparticles by supercritical antisolvent precipitation, Chemical Engineering Journal 277 (2015) 286-294.
5. **V. Prosapio**, E. Reverchon, I. De Marco, Control of powders morphology in the supercritical antisolvent technique using solvent mixtures, Chemical Engineering Transactions 43 (2015) 763-768.
6. **V. Prosapio**, E. Reverchon, I. De Marco, Coprecipitation of PVP/β-carotene by supercritical antisolvent processing, Industrial & Engineering Chemistry Research 54 (2015) 11568-11575.
7. **V. Prosapio**, E. Reverchon, I. De Marco, Production of Lysozyme Microparticles to be used in Functional Foods, using an Expanded Liquid Antisolvent Process, The Journal of Supercritical Fluids 107 (2016) 106-113.
8. **V. Prosapio**, E. Reverchon, I. De Marco, Polymers' ultrafine particles for drug delivery systems precipitated by supercritical carbon dioxide + organic solvent mixtures, Powder technology 292 (2016) 140-148.
9. **V. Prosapio**, I. De Marco, E. Reverchon, PVP/corticosteroid microspheres produced by supercritical antisolvent coprecipitation, Chemical Engineering Journal 292 (2016) 264-275..

Book chapter

D. Bassing, M. Rossmann, I. De Marco, V. Prosapio, E. Reverchon, E. Schlücker, A. Braeuer, Manuscripts for Final

Reporting of SPP Process Spray Projects. Tailored Powder Particles in Spray Processes – Process Spray, *In press*.

Proceedings

1. **V. Prosapio,** E. Reverchon, I. De Marco, Expanded Liquid Antisolvent Micronization of BSA, 10th Conference on Supercritical Fluids and Their Applications, Naples April 29 - May 6 2013, Naples, Italy.
2. I. De Marco, **V. Prosapio**, F. Cice, E. Reverchon, Cellulose acetate micronization using solvent mistures in SAS process, 10th Conference on Supercritical Fluids and Their Applications, Naples April 29 - May 6 2013, Naples, Italy.
3. **V. Prosapio,** E. Reverchon, I. De Marco, Bovine Serum Albumin micronization from aqueous solutions using Expanded Liquid Antisolvent process, 14th European Meeting on Supercritical Fluids, May 18-21 2014, Marseille, France.
4. **V. Prosapio,** S. Cardea, E. Reverchon, I. De Marco, Supercritical carbon dioxide + organic solvent misture for the antisolvent micronization of sodium alginate, 21st International Congress of Chemical and Process Engineering CHISA August 23-27 2014 Prague, Czech Republic.
5. **V. Prosapio,** E. Reverchon, I. De Marco, Micronization of Lysozyme by Expanded Liquid Antisolvent process, 21st International Congress of Chemical and Process Engineering CHISA August 23-27 2014 Prague, Czech Republic.

CONTENTS

FIGURE INDEX..V

TABLE INDEX...XI

ABSTRACT...XIII

INTRODUCTION...XV

CHAPTER I...1

AIM OF THE WORK..1

CHAPTER II..3

STATE OF THE ART OF SAS PROCESS..3

II.1 HIGH-PRESSURE PHASE EQUILIBRIA..3
II.2 JET FLUID DYNAMICS...5
II.3 MASS TRANSFER...7
II.4 INTERACTIONS OF PHASE EQUILIBRIA, JET FLUID DYNAMICS AND MASS TRANSFER DURING SUPERCRITICAL ANTISOLVENT MICRONIZATION...9

CHAPTER III..15

ANALYTICAL METHODS...15

III.1 MORPHOLOGY ANALYSES...15
III.1.1 SCANNING ELECTRON MICROSCOPE FIELD EMISSION.....................15
III.2 SOLID STATE ANALYSES..16
III.2.1 X-RAY DIFFRACTION (XRD)..16
III.2.2 DIFFERENTIAL SCANNING CALORIMETRY (DSC)..........................16
III.3 STABILITY AND DENATURATION ANALYSES...............................16
III.3.1 FOURIER TRANSFORM INFRARED FT-IR......................................16
III.3.2 HIGH PERFORMANCE LIQUID CHROMATOGRAPHY.......................16

III.3.3 ENZYMATIC ACTIVITY..17
III.3.4 ACTIVE PRINCIPLE INGREDIENT ENTRAPMENT EFFICIENCY AND RELEASE...17
III.4 SOLVENT RESIDUE ANALYSIS 17

CHAPTER IV...19

STUDY OF THE PRECIPITATION MECHANISMS INVOLVED IN SAS PROCESS..19

IV.1 STUDY OF JET BEHAVIOR OF SOLVENT MIXTURES.......................19
IV.1.1 ELASTIC LIGHT SCATTERING..19
IV.1.2 COMBINED ELASTIC AND INELASTIC LIGHT SCATTERING 25
IV.2 SAS PRECIPITATION EXPERIMENTS 31
IV.2.1 SAS PRECIPITATION EXPERIMENTS ON PVP.................................32
IV.2.2 SAS PRECIPITATION EXPERIMENTS ON CA 40

CHAPTER V 51

COPRECIPITATION IN SAS PROCESS...51

V.1 BACKGROUND 51
V.2 PRECIPITATION EXPERIMENTS..52
V.2.1 PVP/FOLIC ACID...52
V.2.2 PVP/B-CAROTENE COPRECIPITATES 65
V.2.3 PVP/CORTICOSTEROIDS COPRECIPITATES 76
V.2.4 INTERPRETATION OF RESULTS 92
V.2.5 CONCLUSIONS...95

CHAPTER VI...97

PROCESSING OF WATER SOLUBLE COMPOUNDS BY ELAS PROCESS...97

VI.1 BACKGROUND..97
VI.2 PRECIPITATION EXPERIMENTS 100
VI.2.1 BOVINE SERUM ALBUMIN (BSA).. 102
VI.2.2 LYSOZYME FROM CHICKEN EGG WHITE 113
VI.2.3 SODIUM ALGINATE AND POLYVINYL ALCOHOL (PVA)................ 123
VI.2.4 INTERPRETATION OF RESULTS OF ELAS EXPERIMENTS............... 133

CHAPTER VII..139

CONCLUSIONS 139

REFERENCES...141

LIST OF SYMBOLS..157

Figure index

Figure II.1 *VLE of a binary system of type I (Konynenburg and Scott, 1980).* 4
Figure II.2 *Morphologies obtained by SAS: a) nanoparticles; b) microparticles; c) expanded microparticles; d) crystals.* 5
Figure II.3 *Reynolds number vs. Ohnesorge number for the system* CO_2-H_2O *(from (Riestenberg et al., 2004)).* 6
Figure II. 4 *Scattering phenomena related to jet mixing (from(Reverchon et al., 2010)).* 10
Figure II. 5 *Jet images of CHF, AC, NMP, EtOH and DMSO injected at 313 K with a flow rate of 2.5 mL/min through the Ø = 80 µm nozzle into* $scCO_2$ *(from(De Marco et al., 2012)*..11
Figure II. 6 *Principle of Raman scattering, h: Planckis constant, v: frequency of the light wave, hv: energy of the light wave (from(Dowy et al., 2009))*..12
Figure II. 7 *Crosstalk correction of the* CO_2 *Raman signal interfered by the ethanol Raman signal (from (Dowy et al., 2009))*....................................13
Figure II. 8 *Evaluation procedure for the identification of the location of first detectable particle generation (LFDPP) (from (Rossmann et al., 2012))*..14
Figure IV. 1 *Schematics of the optical setup(from (Reverchon et al., 2010))*..20
Figure IV. 2 *Jet images of solvent mixtures of DMSO and AC injected at 313 K with a flow rate of 2.5 mL/min through a Ø = 80 µm nozzle into* $scCO_2$ *(De Marco et al., 2012).* 22
Figure IV. 3 *Jet images of solvent mixtures of EtOH and AC injected at 313 K with a flow rate of 2.5 mL/min through a Ø = 80 µm nozzle into* $scCO_2$ *(De Marco et al., 2015).* 23
Figure IV. 4 *Jet images of solvent mixtures of NMP and AC injected at 313 K with a flow rate of 2.5 mL/min through a Ø = 80 µm nozzle into* $scCO_2$ *(De Marco et al., 2015)*..24
Figure IV. 5 *Schematic of the experimental setup, (M: mirror, BS: beam splitter, SL: spherical lens, CL: cylindrical lens, BD: beam dump, DM: dichroitic mirror, NDF: neutral density filter, BPF: band pass filter, LPF: long pass filter, EMCCD-C: electron multiplying charge coupled device camera) (from (Dowy et al., 2010))*...25
Figure IV. 6 *LFDPP of PVP in EtOH/AC 30/70 % obtained at 313 K, with a PVP concentration of 0.5 % wt, a solution flow rate of 2 mL/min, a* CO_2 *flow rate of 200 g/min and varying the operating pressure from 7.5 MPa to 14 MPa*..28

Figure IV. 7 *Length of the LFDPP of PVP in EtOH/AC 30/70 % obtained at 313 K, with a PVP concentration of 0.5 % wt, a solution flow rate of 2 mL/min, a CO_2 flow rate of 200 g/min and varying the operating pressure from 7.5 MPa to 14 MPa.* 29

Figure IV. 8 *LFDPP of PVP in different mixtures of EtOH and AC at 313K, 10 MPa, with a PVP concentration of 0.5 % wt, a solution flow rate of 2 mL/min and a CO_2 flow rate of 200 g/min.* 29

Figure IV. 9 *Length of the LFDPP of PVP varying the AC content in the mixture EtOH/AC at 313K, 10 MPa, with a PVP concentration of 0.5 % wt, a solution flow rate of 2 mL/min and a CO_2 flow rate of 200 g/min* 30

Figure IV. 10 *CO_2 molar fraction (X_{CO2}) varying the AC content in the mixture EtOH/AC* 30

Figure IV. 11 *Schematic representation of a SAS apparatus. S1: CO_2 supply; S2: liquid solution; RB: refrigerating bath; P1, P2: pumps; TC: thermocouple; M: manometer; PV: precipitation vessel; MV: micrometering valve; LS: liquid separator; BPV: back pressure valve; R: rotameter; DM: dry test meter.* 32

Figure IV. 12 *FESEM images of PVP precipitated at 313 K, 10 MPa, 1% wt from different AC/EtOH mixtures percentages: (a) 0/100 (w/w); (b) 30/70 (w/w); (c) 50/50 (w/w); (d) 70/30 (w/w)* 35

Figure IV. 13 *Volumetric particle size distributions of PVP precipitated at 313 K, 10 MPa, 1% wt from pure EtOH and from different AC/EtOH mixtures percentages* 36

Figure IV. 14 *PVP precipitated at 313 K, 10 MPa, 1% wt. (a-b) FESEM images from pure NMP (a) and AC/NMP 50/50 (b); (c) volumetric particle size distributions* 38

Figure IV. 15 *Differential scanning calorimetry thermograms for unprocessed and SAS processed PVP using the different mixtures* 39

Figure IV. 16 *XRD analysis of unprocessed and SAS processed PVP using the different mixtures* 40

Figure IV.17 *FESEM images of cellulose acetate precipitated at 9.0 MPa, 40°C, 60 mg/mL at different DMSO/Acetone mixtures percentages; (a) 25/75 (v/v); (b) 50/50 (v/v); (c)75/25 (v/v).* 44

Figure IV.18 *Volumetric particle size distributions of cellulose acetate precipitated at 9.0 MPa, 313 K and at different concentrations for different mixtures; (a) c = 20 mg/mL;(b) c = 40 mg/mL; (c) c = 60 mg/mL.* 45

Figure IV. 19 *FESEM images of cellulose acetate precipitated at 313 K, 40 mg/mL, DMSO/Acetone 25/75 (v/v) at different pressures; (a) P = 8.5 MPa; (b) P = 9.0 MPa; (c) P = 10.0 MPa.* 47

Figure IV.20 *Volumetric particle size distributions of cellulose acetate precipitated at 313 K and 40 mg/mL at different pressures.* 48

Figure IV.21 *Differential scanning calorimetry thermograms for unprocessed and SAS processed CA, Exo indicates exothermic flow.* 49

Figure IV.22 *XRD analysis of unprocessed and SAS processed CA* 50

Figure V. 1 *FESEM image of FA precipitated from DMSO at 15 MPa, 313 K, 20 mg/mL.* 54
Figure V. 2 *FESEM image of PVP precipitated from DMSO at 15 MPa, 313 K, 20 mg/mL.*..........55
Figure V.3 *FESEM images of PVP–FA particles precipitated from DMSO at 15.0 MPa and 313 K at different polymer/drug ratios: (a) 1/1 w/w, (b) 5/1 w/w, (c) 20/1 w/w*..........57
Figure V.4 *Volumetric cumulative PSDs of PVP–FA nano and sub-microparticles precipitated from DMSO at 15.0 MPa and 313 K at different polymer/drug ratios*..........58
Figure V.5 *FESEM images of PVP–FA particles precipitated from DMSO at 9 MPa and 313 K with different polymer/drug ratio: (a) 5/1 w/w, (b) 10/1 w/w, (c) 20/1 w/w*..........59
Figure V.6 *Volumetric cumulative PSDs of PVP-FA microparticles precipitated from DMSO at 9 MPa and 313 K at different polymer/drug ratios, using FESEM images analysis and DLS analysis*..........60
Figure V.7 *Volumetric cumulative PSDs of PVP-FA particles precipitated from DMSO: effect of the operating pressure* 61
Figure V.8 *Volumetric cumulative PSDs of PVP-FA particles precipitated from DMSO: effect of the operating temperature.*..........62
Figure V.9 *XRD analysis of unprocessed and processed powders*..........63
Figure V.10 *HPLC traces of unprocessed and processed powders.*..........64
Figure V.11 *Dissolution profiles of FA in PBS at 310 K and pH 7.0*..........65
Figure V.12 *FESEM image of BC precipitated from AC/EtOH 70/30 at 8.5 MPa, 313 K and 5 mg/mL.* 68
Figure V.13 *FESEM image of PVP precipitated from AC/EtOH 70/30 at 8.5 MPa, 313 K and 5 mg/mL.*..........69
Figure V.14 *Photos of the filter of PVP/BC 10:1 processed at 8.5 MPa, 313 K, 5 mg/mL: a) PVP molecular weight of 40000 g/mol; b) PVP molecular weight of 10000 g/mol.*..........70
Figure V.15 *FESEM images of PVP/BC 10:1 processed at 8.5 MPa, 313 K, 5 mg/mL: a) PVP* 71
Figure V.16 *FESEM images of PVP/BC particles precipitated from AC/EtOH 70/30 at 85 MPa and 313 K at different polymer/drug ratios: (a) 15/1 w/w, (b) 20/1 w/w*..........72
Figure V.17 *FESEM images of PVP/BC particles precipitated from AC/ETOH 70/30 at 313 K and different pressures: (a) 9.0 MPa; (b) 10.0 MPa.* 73
Figure V.18 *Volumetric particle size distributions of PVP/BC 10/1 coprecipitates obtained at different pressures*..........74
Figure V.19 *Dissolution profiles of BC in PBS at 310 K and pH 7.0*..........75
Figure V. 20 *FESEM images of corticosteroids precipitated from EtOH at 15MPa, 313 K and a concentration of 20 mg/mL: a) DMS, b) PDN; c) BDS. Large crystals were obtained in all cases*..........79

Figure V. 21 *FESEM image of PVP microparticles precipitated from EtOH at 15 MPa, 313 K and 20 mg/mL.* ... 80

Figure V. 22 *FESEM images of PVP/corticosteroids 2:1 particles precipitated from EtOH at 9 MPa, 313 K and 20 mg/mL: a) PVP/DMS, b) PVP/PDN; c) PVP/BDS* ... 82

Figure V. 23 *FESEM images of PVP/corticosteroids 5:1 particles precipitated from EtOH at 9 MPa, 313 K and 20 mg/mL: a) PVP/DMS, b) PVP/PDN; c) PVP/BDS* ... 83

Figure V. 24 *Volumetric cumulative PSDs of microparticles precipitated from EtOH at 9MPa and 313 K at different polymer/drug ratios: a) PVP/DMS, b) PVP/PDN* ... 84

Figure V. 25 *PVP/PDN 10:1 particles precipitated from EtOH at 15 MPa, 313 K and 20 mg/mL: a) FESEM image; b) particle size distribution.* ... 85

Figure V. 26 *FE-SEM images of PVP/PDN 10:1 particles precipitated from EtOH at 9 MPa, 313 K and different concentrations: a) 10 mg/mL; b) 20 mg/mL; c) 30 mg/mL.* ... 87

Figure V. 27 *Volumetric cumulative PSDs of PVP/PDN 10:1 particles precipitated from EtOH at 9 MPa and 313 K at different concentrations.* ... 87

Figure V. 28 *FT-IR spectra of unprocessed, physical mixtures and SAS processed PVP/corticosteroids: a) dexamethasone; b) prednisolone; c) budesonide.* ... 89

Figure V. 29 *Dissolution profiles in PBS at 310 K and pH 7.4: a) DMS; b) PDN; c) BDS* ... 92

Figure VI.1 *VLE of the binary system* CO_2-H_2O *(Takenouchi and Kennedy, 1964).* ... 97

Figure VI.2 *High pressure phase equilibria diagram for the system* CO_2–EtOH–H_2O *at 313 K and different pressures (Durling et al., 2007).* ... 99

Figure VI.3 *Schematic representation of ELAS apparatus. S1:* CO_2 *supply; S2: co-antisolvent supply; S3: aqueous solution supply; RB: refrigerating bath; P1, P2, P3: pumps; TC: thermocouple; M: manometer; PM: pre-mixer; PC:* ... 101

Figure VI. 4 *FESEM images of BSA particles obtained at 15.0 MPa and 313 K using an ethanol flow rate of: (a) 10 mL/min; (b) 15 mL/min; (c) 25 mL/min* ... 104

Figure VI.5 *Volumetric cumulative BSA particle size distributions obtained at 15.0 MPa and 313 K at different ethanol flow rates* ... 105

Figure VI.6 *FESEM images of BSA particles obtained at 15.0 MPa and 313 K using an acetone flow rate of: (a) 15 mL/min; (b) 25 mL/min.* ... 106

Figure VI.7 *Volumetric cumulative BSA particle size distributions, obtained at 15.0 MPar and 313 K using acetone as co-antisolvent, at different water flow rates* ... 107

Figure VI. 8 *FESEM images of BSA particles obtained at 15.0 MPa and 313 K using an isopropyl alcohol flow rate of: (a) 10 mL/min; (b) 15 mL/min; (c) 25 mL/min* ... 109

Figure VI.9 *Volumetric cumulative PSDs of the BSA particles obtained at 15.0 MPa and 313 K at different isopropyl alcohol flow rates* 110
Figure VI.10 *XRD analysis of unprocessed and ELAS processed BSA particles obtained using the different co-antisolvents.* 111
Figure VI.11 *FT-IR traces for unprocessed and ELAS processed BSA particles obtained using the different co-antisolvents.* 112
Figure VI.12 *HPLC traces for unprocessed and ELAS processed BSA, using* 113
Figure VI.13 *FESEM images of Lysozyme particles obtained adding an Acetone flow rate of 25 mL/min to* CO_2 *and operating at different enzyme concentrations: (a) 10 mg/mL; (b) 20 mg/mL; (c) 50 mg/mL.* 117
Figure VI.14 *Volumetric cumulative PSDs of Lysozyme particles obtained at different lysozyme concentrations in water (10-50 mg/mL) using an Acetone flow rate of 25 mL/min.* 117
Figure VI.15 *FESEM images of Lysozyme microparticles obtained using an Isopropyl alcohol flow rate of: (a) 10 mL/min; (b) 15 mL/min; (c) 25 mL/min.* 119
Figure VI. 16 *Volumetric cumulative PSDs of Lysozyme precipitated from water at 20 mg/mL at different Isopropyl alcohol flow rates.* 119
Figure VI.17 *Volumetric cumulative PSDs of Lysozyme particles obtained from water at different concentrations (20-50 mg/mL) using an Isopropyl alcohol flow rate of 25 mL/min.* 120
Figure VI.18 *XRD analysis of unprocessed and ELAS processed Lysozyme particles obtained using the different co-antisolvents.* 121
Figure VI.19 *FT-IR traces for unprocessed and ELAS processed Lysozyme particles obtained using the different co-antisolvents.* 122
Figure VI.20 *FESEM image of nanostructured SA EMP obtained using an ethanol flow rate of 10 mL/min.* 126
Figure VI.21 *FESEM images of PVA particles precipitated using an ethanol flow rate of: (a) 10 mL/min, (b) 15 mL/min.* 127
Figure VI.22 *Volumetric cumulative PSDs of PVA particles obtained at different ethanol flow rate.* 128
Figure VI.23 *FESEM images of microparticles obtained using an acetone flow rate of 25 mL/min: (a) SA; (b) PVA.* 129
Figure VI.24 *FESEM images of SA particles obtained using an isopropyl alcohol flow rate of: (a) 10 mL/min; (b) 15 mL/min.* 130
Figure VI.25 *Volumetric cumulative PSDs of sodium alginate particles obtained at different iPrOH flow rates.* 131
Figure VI.26 *FESEM image of PVA particles obtained using an iPrOH flow rate of 10 mL/min.* 131
Figure VI.27 *Volumetric cumulative PSDs sodium alginate particles obtained at different concentrations using iPrOH as co-antisolvent.* 132
Figure VI.28 *High pressure phase equilibria for the systems* CO_2/H_2O*/co-antisolvent, at 313 K and different pressures, adapted from literature*

(Durling et al., 2007, Traub and Stephan, 1990, Bünz et al., 1994, Chun and Wilkinson, 1999): a) ethanol; b) acetone; c) isopropyl alcohol. I indicates the homogeneous region, II the two-phase region..................... 136

Table index

Table IV.1 *SAS experiments performed on PVP at 40 °C, 10 MPa and 1% wt (NP: nanoparticles; MP: microparticles; SMP: sub-microparticles).*.....33
Table IV.2 *SAS experiments performed on CA at 40 °C (NP: nanoparticles; MP: microparticles).*...41
Table V.1 *SAS experiments performed on PVP/FA mixtures (MP: microparticles, SMP: sub-microparticles; NP: nanoparticles).*54
Table V.2 *Summary of SAS experiments performed on PVP/BC (MP: microparticles; NP: nanoparticles; C:crystals).*......................................67
Table V.3*: Summary of SAS experiments (MP: microparticles, SMP: sub-microparticles; C: crystals; m.d.: mean diameter; s.d.: standard deviation)*...77
Table V.1 *SAS experiments performed on PVP/FA mixtures (MP: microparticles, SMP: sub-microparticles; NP: nanoparticles)*...................54
Table V.2 *Summary of SAS experiments performed on PVP/BC (MP: microparticles; NP: nanoparticles; C:crystals).*......................................67
Table V.3*: Summary of SAS experiments (MP: microparticles, SMP: sub-microparticles; C: crystals; m.d.: mean diameter; s.d.: standard deviation).* 77
Table VI. 1 *ELAS experiments performed on BSA at 15.0 MPa and 40 °C (NP:nanoparticles; SMP: sub-microparticles; MP: microparticles).*........102
Table VI. 2 *Summary of ELAS experiments performed on lysozyme (MP: microparticles; u.*: unsuccessful).*...115
Table VI. 3 *ELAS experiments performed on sodium alginate and PVA (NP: nanoparticles; MP: microparticles; NMP: Nanostructured microparticles; u.*: unsuccessful; m.d.: mean diameter; s.d.: standard deviation)*...125

Abstract

In the last decade, the application of microparticles, nanoparticles and composite microparticles involved several industrial fields. Conventional micronization techniques, such as jet milling, spray drying, liquid antisolvent precipitation and solvent evaporation are sometimes not suitable, since the produced particles are irregular, with broad size distribution, could be degraded due to mechanical or thermal stresses and polluted with organic solvents or other toxic substances. In this context, supercritical fluids (SCFs) based techniques have been proposed as an alternative to traditional processes thanks to the specific characteristics of SCFs, mainly solvent power and liquid-like densities with gas-like transport properties, that can be tuned varying pressure and temperature. Among supercritical assisted micronization techniques, Supercritical Antisolvent (SAS) precipitation has been successfully used to obtain microparticles and nanoparticles of several kinds of compounds, such as pharmaceuticals, coloring matters, polymers and biopolymers. In this process carbon dioxide (CO_2) is used as an antisolvent at supercritical conditions: a solution containing the product to be micronized is injected into the precipitation chamber, saturated with supercritical carbon dioxide under the chosen conditions of temperature and pressure. CO_2, in contact with the solution, forms a mixture in which the product is insoluble, causing the precipitation.

Some aspects of SAS process that are still little examined have been investigated in depth: the influence of the kind of solvent on particle morphology, the polymer/drug coprecipitation and the processing of water soluble compounds.

In order to identify the correlation between the kind of solvent and particle morphology, the jet behavior of solvent mixtures in contact with CO_2 was studied using elastic light scattering and Raman scattering techniques. It has been observed that for some solvents, like dimethylsulfoxide (DMSO), N-methyl-2-pyrrolidone (NMP) and ethanol (EtOH), the transition from the two-phase mixing (subcritical conditions) to the single-phase mixing (supercritical conditions) with the bulk CO_2 occurrs on a large pressure range; whereas, for other solvents, like acetone (AC) and chloroform (CHF), the transition occurs on a narrow pressure range. Analyzing the evolution of the interface between the injected solvent and bulk CO_2 for solvent mixtures AC/DMSO, AC/EtOH and AC/NMP, it was observed that they show intermediate behaviors between the two solvents during SAS processing. Moreover, precipitation experiments performed on two model compounds, cellulose acetate (CA) and polyvinylpirrolidone (PVP), demonstrated that it is possible to modulate the morphology of SAS precipitates using the appropriate

solvent mixture. This part of the thesis was carried out on in collaboration with the Applied Raman Scattering (ARS) Laboratory of the Erlangen Graduate School of Advanced and Optical Technology (SAOT) of the Friedrich-Alexander-Universität (FAU) Erlangen-Nürnberg.

SAS coprecipitation applicability, limitations and the possible precipitation mechanisms were investigated studying the effect of all the operating parameters, to elucidate the conditions for a successful coprecipitation. Well separated microspheres for the systems PVP/folic acid, PVP/β-carotene and PVP/corticosteroids were obtained. Moreover, a coprecipitation mechanism was postulated: using PVP as carrier to retard crystal growth and working near above the mixture critical point (MCP) of the binary system solvent/antisolvent, i.e. when microparticles are produced, coprecipitation is successful because all the content of the droplet concurs the formation of the final particle. Dissolution tests confirmed the occurred coprecipitation: the produced composite microspheres showed a significant increase of the active compound dissolution rate with respect to the dissolution rate of the unprocessed compound.

In order to process water soluble compounds, a modification of SAS process, called Expanded Liquid Antisolvent precipitation (ELAS), was used because of the limited solubility of water in CO_2 at ordinary SAS operating conditions (313-333 K, 10-25 MPa). ELAS allows the processing of hydrosoluble compounds using a mixture of CO_2 and a polar organic solvent, called co-antisolvent, at expanded liquid conditions. In this work the applicability of this technique was tested on bovine serum albumin, lysozyme, sodium alginate and polyvinyl alcohol using different co-antisolvents, like ethanol, acetone and isopropanol (iPrOH). For each compound, it has been investigated the effect of all the operating parameters on morphology, mean size and particles size distribution. Nanoparticles, microparticles and expanded microparticles were successfully produced varying the kind of co-antisolvent and the process parameters. In particular, it was found that the use of $EtOH/CO_2$ antisolvent mixtures led to the production of micro and nanoparticles with narrow particle size distributions; the use of AC/CO_2 and $iPrOH/CO_2$ as antisolvent mixtures, instead, led mainly to the production of microparticles and expanded micro-particles. Moreover, it was hypothesized that the distance of the operating point with respect to the ternary high pressure vapor-liquid equilibria (VLE) can condition the morphology of the precipitates: increasing the co-antisolvent mole fraction, this distance increases, the mean size of the particles decreases and the particle size distribution become narrower. The analyses confirmed that the obtained particles are characterized by good biological activity, unaltered conformational structure and negligible solvent residue.

Introduction

Over the past decade, the interest in the production of microparticles, nanoparticles and composite microparticles has increased significantly since they are largely used in several industrial fields.

Microparticles have widespread applications in pharmaceutical field for aerosol and injectable formulations, in chromatography as stationary phases, in catalysis as supports, in coloring industry for the production of inks, toners and paints with improved duration and brightness, in the electro-technical industry for the production of high-temperature superconductors (Reverchon et al., 2008a).

Nanoparticles show even more applications since at nanoscale matter properties can change considerably. Indeed, it is possible to produce explosives with a higher potential, pigments with shining colors and drugs for targeted delivery (Reverchon et al., 2007).

Composite microparticles can be produced in form of microspheres or microcapsules; in the first case the polymer and the drug are uniformly dispersed within the same particle, whereas in the second case the drug is surrounded by a polymeric shell. This kind of particles have been found to be particularly useful in food and nutraceutical fields to protect the active compound from degradation and in pharmaceutical field for the drug controlled delivery (Montes et al., 2011).

There are several micronization techniques, which can be divided in two categories: “top down” and “bottom up”. In the “top-down” approach the micronized material is obtained reducing the dimensions of the original material; whereas, in the “bottom-up” approach particles are obtained starting from the molecular scale, such as for example the precipitation from a fluid phase (Reverchon and Adami, 2006).

Conventional micronization processes

Conventional micronization techniques suffer from several drawbacks, such as the production of coarse particles with broad particle size distribution, possible degradation of the product due to mechanical or thermal stresses and contamination of particles with organic solvents or other toxic substances. The processes mainly used are briefly described below.

Spray drying

In the spray drying process, the feed solution containing the solute is atomized through an injector into droplets that dry rapidly due to their high surface area and to the intimate contact with the drying gas (compressed air or nitrogen). The rapid removal of the solvent from the dried area protects the dried powder from overheating. Using cyclones or filters it is possible to recover the final product from the air stream (Shoyele and Cawthorne, 2006).

The obtained powders have dimensions in the order of 100 microns. The main limitations of this technique lie in the difficulty of control the particle size distribution (which is very wide), in the poor yields of the process and in the possible degradation of the product due to the high temperatures used.

Spray freeze drying

In the spray freeze drying process, the solution formed by solvent and solute is sprayed into a vessel containing a cryogenic liquid such as liquid nitrogen or a cold gas stream. The frozen droplets are then lyophilized, leading the formation of fine particles. The low temperature and pressure conditions allow to minimize the degradation of the product and also promote the production of highly porous particles (Liapis and Bruttini, 2009).

Jet milling

In the jet milling process, a high velocity medium gas (air or nitrogen) passing through a nozzle carries coarse particles into the jet mill and causes their fracture by inter-particle collision and impacting against the walls of the vessel. In this way, particles in the range 1–20 μm are produced.

This technique show several drawbacks, such as the lack of control over particle size and particle size distribution, and the high energy input which can promote chemical degradation (Shoyele and Cawthorne, 2006).

Liquid antisolvent precipitation

The liquid antisolvent precipitation consists of successive steps in which the solution containing the solute to micronized is mixed with and antisolvent; since the solute is not soluble in this mixture it precipitates. The main driving force for precipitation is the rapid and high supersaturation (Thorat and Dalvi, 2012). The disadvantages of this process are: wide size distribution of the crystals; high residual solvent in the final product; long residence times required.

Emulsion/Solvent evaporation

Emulsion/Solvent evaporation is a process mainly focused on the production of composite particles. In this technique, the polymer is dissolved in a suitable water immiscible solvent and the drug is dispersed or dissolved in this polymeric solution. The resultant solution or dispersion is then emulsified in an aqueous continuous phase to form discrete droplets. The emulsion is continuously stirred at a fixed temperature so that causes the evaporation of the solvent and the consequent hardening of the microspheres. The properties of the final particles depend on different variables, such as drug solubility, kind of solvent, diffusion rate, temperature, polymer composition and viscosity (Zhang et al., 2009).

This technique, however, generally provide limited control over the particles size and particle size distribution and high residual solvent.

Supercritical fluids based processes

Supercritical fluids (SCFs) based techniques have been proposed as an alternative to conventional processes thanks to their specific characteristics, mainly solvent power and liquid-like densities with gas-like transport properties, which can be tuned varying pressure and temperature.

The mostly used supercritical fluid is carbon dioxide (CO_2) since it has an easily accessible critical points of 304.25 K and 7.38 MPa and it is non-combustible, non-toxic as well as being relatively environmentally benign. These properties offer many advantages in the use of supercritical CO_2 ($scCO_2$): the use of organic solvents is reduced or eliminated; in separation operations the product is easily obtained through depressurizing and the recovered CO_2 can be recycled, minimizing consumption; the process can be carried out at a temperature close to room temperature, thus preventing the degradation of thermolabile compounds and reducing the energy costs; CO_2 is also a suitable inert medium to process easily oxidizable substances.

A possible general classification of SCF based techniques can be proposed according to the role played by SCF in the process. Indeed, SCFs can be used as solvents, solutes, antisolvents and reaction media.

RESS (Rapid Expansion of Supercritical Solutions)

The Rapid Expansion of Supercritical Solutions (RESS) consists of the dissolution of a solid substrate in the supercritical fluid; then, this solution is depressurized into a low pressure chamber produces through an injector producing a rapid nucleation of the substrate in form of small particles (Jung and Perrut, 2001). The advantage of this process is the total absence of organic solvents but the main limitation consists in the difficulty of controlling the particle size of the precipitates.

A variation of the RESS process is the rapid expansion of a supercritical solution into a liquid solvent (RESOLV) that consists of spraying the supercritical solution into a liquid: in this way, it is possible to quench particles growth in the precipitator.

RESS and RESOLV processes, however, can be used only to micronize products that show a reasonable solubility in the selected supercritical fluid; moreover, in RESOLV the presence of a liquid make the process no more solventless (Reverchon and Adami, 2006).

PGSS (Precipitation from Gas Saturated Solution)

Particles from Gas Saturated Solution (PGSS) process, a low-melting point polymer is dissolved in carbon dioxide causing a strong reduction of their viscosities and a reduction of their melting and glass transition temperatures. This saturated gas is then expanded to atmospheric pressure and the release of the dissolved gas causes a drastic reduction of the temperature and an increase of the melting temperature (up to the usual value at ambient pressure), which lead to a fast solidification of the polymer (Fraile et al., 2013).

SAA (Supercritical Assisted Atomization)

In Supercritical Assisted Atomization (SAA) carbon dioxide is used as a co-solute to enhance droplets formation during atomization. In this process, within a saturator $scCO_2$ is dissolved in the solution containing the compound to be micronized, forming an expanded liquid that is characterized by reduced viscosity and surface tension (i.e. reduced cohesive forces); this solution is then injected into the precipitator in which the solvent evaporation, achieved using hot nitrogen, leads to the production of particles (Martin et al., 2013).

The limitations of this process are: the inability to produce nanoparticles since the dimensions of the particles produced depend on the dimensions of the droplets generated and the high temperatures required. In order to process thermolabile compounds a vacuum system downstream the precipitator is needed since the temperature necessary to allow the evaporation of the solvent changes with the precipitation pressure.

SAS (Supercritical Antisolvent)

Supercritical Antisolvent (SAS) precipitation represents an innovative alternative to the traditional liquid antisolvent technique since it allows to completely separate the solvent and the antisolvent by pressure reduction, avoiding post-process treatments. Moreover, the supercritical antisolvent is characterized by diffusivities that can be up to two orders of magnitude larger than those of liquids. At the process conditions, the supercritical fluid should be completely miscible with the liquid solvent; whereas, the solute should be insoluble in the mixture solvent/antisolvent. The solution is atomized in a bulk CO_2 and the fast mixing/diffusion of $scCO_2$ into the liquid solvent produces the supersaturation of the solute and its precipitation in micronized particles (Reverchon and De Marco, 2004).

This technique allows the production of different morphologies, such as microparticles, nanoparticles and expanded microparticles, and to accurately control of the particle size distribution (PSD).

ELAS (Expanded Liquid AntiSolvent)

Expanded Liquid Antisolvent precipitation (ELAS) is a modification of the SAS process that allows the processing of hydrosoluble compounds using a mixture of carbon dioxide and an organic solvent in expanded liquid conditions (Caputo et al., 2012). Indeed, water soluble compounds cannot be micronized using the SAS process, because water shows a very reduced solubility in CO_2 at ordinary SAS operating conditions. Adding an organic solvent as co-antisolvent, water solubility is widely enhanced and, as a consequence, the solute saturates and precipitates.

SAILA (Supercritical Assisted Injection in a Liquid Antisolvent)

Supercritical Assisted Injection in Liquid Antisolvent (SAILA) is a technique used for the production of stable aqueous nanodispersion. In this process, $scCO_2$ dissolved in the solution containing the solute to micronized into a saturator forming an expanded liquid solution, which is. depressurized directly into water (in which a surfactant can be added) where the solute is not soluble and the organic solvent is miscible; in this manner, nanoparticles can be generated (Campardelli et al., 2012).

Chapter I
Aim of the work

Supercritical Antisolvent (SAS) is a well-known micronization process, that has been successfully used to obtain micro and nanoparticles of many compounds belonging to different categories, such as pharmaceuticals, superconductors, coloring matters, explosives, polymers and biopolymers (Shariati and Peters, 2003, Hakuta et al., 2003, Tabernero et al., 2012). Although this technique has been extensively studied, some process aspects are still unexplored.

Firstly, from SAS literature it has been observed that microparticles of some compounds can be obtained only using solvents for which the transition from the two-phase to the single-phase mixing with supercritical carbon dioxide occurred on a large pressure range, like for dimethylsulfoxide (DMSO), N-methyl-2-pyrrolidone (NMP) and ethanol (EtOH). On the other hand, nanoparticles are mainly obtained from solvents for which the transition occurs on a narrow pressure range (like acetone, AC), since using solvents with a broad transition zone, very higher pressure values are needed to reach single-phase mixing. In order to overcome this limitation, attention has been focused on the study of the jet behavior of solvent mixtures, using elastic light scattering and Raman scattering techniques, to understand if the transition between multi-phase and single-phase mixing of a solvent (such as AC) can be modified by the presence of a second solvent with a completely different behavior (such as DMSO, NMP, EtOH). Moreover, some precipitation experiments have been performed to verify if using solvent mixtures it is possible to obtain micro and nanoparticles for all the solutes.

Another aspect still little studied in SAS literature regards the polymer/drug coprecipitation, due to the difficulty to produce composite microparticles using this technique. Indeed, some authors attempted SAS coprecipitation but, the obtained particles were generally irregular or coalescing, with broad particle size distributions, low drug entrapment efficiency and, in most cases, the demonstration of the effective coprecipitation was at least questionable. An explanation of the coprecipitation mechanism is also missing. In order to overcome these constraints, the aim of this work was to test the applicability of SAS process to produce microcomposite coprecipitates and to understand the possible precipitation mechanisms. For this reason, some precipitation experiments were carried out to study the effect of all the operating parameters in order to elucidate the ideal conditions for a successful coprecipitation using the SAS process.

At last, a further limitation concerns the impossibility of water soluble compounds processing, because of the very reduced solubility of water in CO_2 at ordinary SAS operating conditions. In order to overcome this limitation, De Marco and Reverchon proposed a modification of SAS process, called Expanded Liquid Antisolvent precipitation (ELAS), which allows the processing of hydrosoluble compounds using a mixture of carbon dioxide and a co-antisolvent, in expanded liquid conditions (Caputo et al., 2012). On the basis of preliminary studies performed on bovine serum albumin, the aim of this work was to extend the applicability of this technique to other hydrosoluble materials, like proteins, enzymes and polymers and to use different co-antisolvents, like ethanol, acetone and isopropanol. For each compound, it has been investigated the effect of all the operating parameters on morphology, mean size and particles size distribution.

Chapter II
State of the art of SAS process

The Supercritical Antisolvent (SAS) precipitation has been successfully used to micronize many compounds belonging to different categories, such as pharmaceuticals, superconductors, cosmetics, coloring matters, explosives, polymers and biopolymers (Shariati and Peters, 2003, Hakuta et al., 2003, Tabernero et al., 2012).

Several particle morphologies have been recurrently obtained by SAS: nanoparticles with mean diameters in the 30–200 nm range (Reverchon et al., 2007), microparticles in the 0.25–20 µm range (Reverchon et al., 2008a), expanded hollow microparticles (called balloons) with diameters between about 10 and 200 µm (E. Reverchon, 2008) and crystals with micrometric dimensions and various habits (Park et al., 2007).

In order to describe the SAS process, three aspects and their interactions have to be considered, which are:

1. high-pressure vapor liquid equilibria (VLEs) of the system formed by solute, solvent and antisolvent;
2. fluid dynamics of the injected solution in contact with compressed carbon dioxide;
3. mass transfer to and from the injected solution that causes the generation of the solute particles.

II.1 High-pressure phase equilibria

SAS process is based on two prerequisites: the solvent and the antisolvent must be completely miscible at the process conditions and the solute must be insoluble in the mixture solvent/antisolvent. If this last condition is verified, the presence of solute can be neglected and the fluid phase system formed in the precipitator can be treated as a binary one.

According to the classification proposed by Van Konynenburg and Scott (Konynenburg and Scott, 1980), CO_2 and organic solvents usually form type-I systems, as shown in Figure II.1:

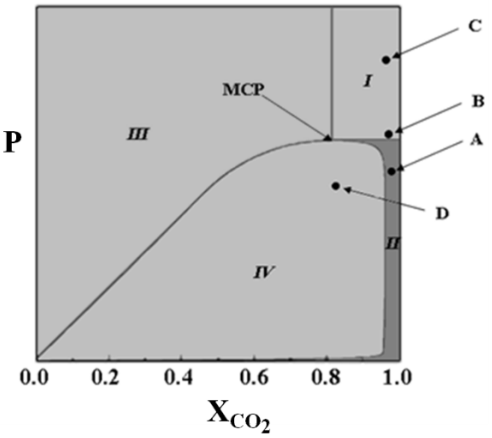

Figure II.1 *VLE of a binary system of type I (Konynenburg and Scott, 1980).*

Looking at this diagram, it is possible to identify four different regions: a supercritical region, which is located at pressures above the mixture critical point (MCP) of the system solvent–antisolvent and in correspondence of a molar fraction larger than that of the MCP (region I); a subcritical gaseous region, located in region II; an expanded liquid region located in region III; a two-phase region located in region IV. Operating in different regions of the VLE diagram, obviously different results can be obtained (as shown in Figure II.2): generally, the precipitation of nanoparticles has been observed far above the MCP at fully developed supercritical conditions (point C in Figure II.1) (Reverchon et al., 2007); microparticles are obtained near above the MCP in the transition zone between two and single-phase mixing (point B in Figure II.1) (Reverchon et al., 2008a); expanded microparticles are observed working in subcritical conditions (point A in Figure II.1) (E. Reverchon, 2008); crystals are obtained when the operating point falls within the miscibility hole.

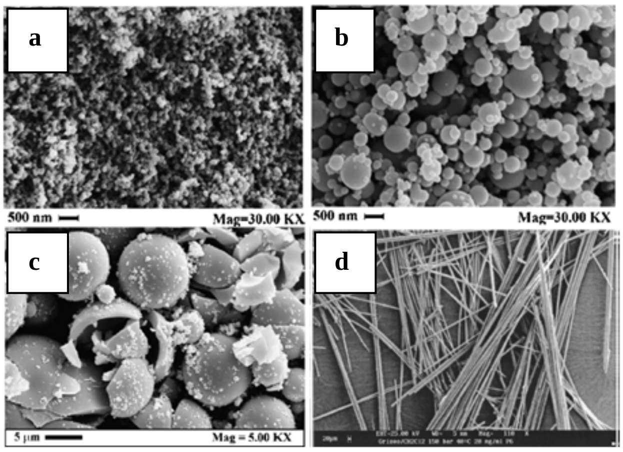

Figure II.2 *Morphologies obtained by SAS: a) nanoparticles; b) microparticles; c) expanded microparticles; d) crystals.*

II.2 Jet fluid dynamics

For liquid-liquid or liquid-gas systems, depending on the liquid flow rate, three main regimes of liquid phase dispersion through a nozzle can be identified: (1) the "dripping" regime, in which drops are formed at the orifice of the nozzle because of an equilibrium of gravitational and capillary forces which does not produce atomization; (2) the laminar regime, in which the jet has a smooth and continuous aspect at the outlet of the nozzle and there is a quasi-periodic emission of droplets identical in size at the break-up; (3) the turbulent regime, in which the jet surface presents irregularities and the droplets formed have different sizes (Badens et al., 2005). In the case of low Reynolds numbers, the jet is characterized by axially symmetric disturbances (varicoses) which produce the break-up. Increasing the Reynolds number, the break-up follows a lateral motion with increasing amplitude, which leads to the formation of an asymmetrical jet (E. Carretier, 2003).

The effect of liquid properties and jet velocity on the mechanism of disintegration of the jet can be studied with a dimensional analysis approach, using two dimensionless numbers:

- the Reynolds number ($Re=Dv\rho/\mu$) which gives a measure of the ratio of inertial forces ($v\rho$) to viscous forces (μ/D), and, consequently, it quantifies the relative importance of these two kind of forces for given flow conditions;
- the Ohnesorge number ($Oh=\mu/\sqrt{D\rho\sigma}$) which relates the viscous and the surface tension forces, by dividing the square root of Weber number ($We=\rho v^2 D/\sigma$) by Reynolds number.

D is the droplet diameter, ρ is the density of the fluid, v is its velocity, μ is its viscosity and σ is the surface tension.

The best known classification of the free jet flow regimes is the one proposed by Ohnesorge (1936). He plotted the Ohnesorge number, in logarithmic scale versus the logarithm of the Reynolds number and obtained straight boundary lines for the borders "Rayleigh disintegration/ wavy disintegration" and "wavy disintegration/ spray disintegration" at atmospheric pressure (Figure II.3).

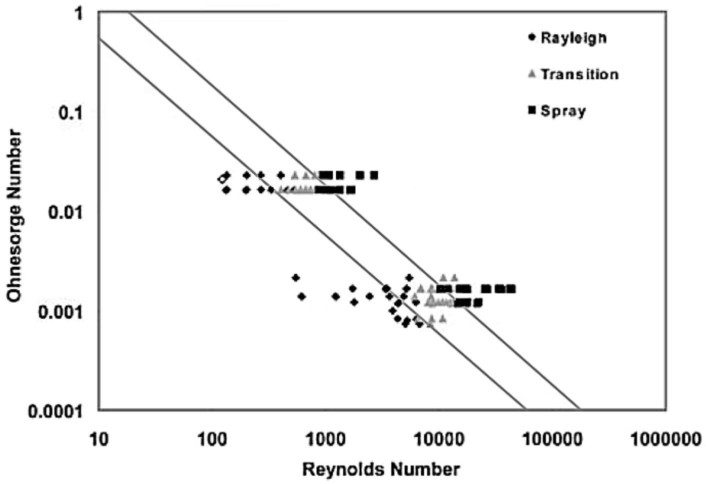

Figure II.3 *Reynolds number vs. Ohnesorge number for the system* CO_2*-*H_2O *(from (Riestenberg et al., 2004)).*

As shown in Figure II.3, at constant Re number break-up can be changed from the Rayleigh to the spray regime by decreasing the injector orifice, since in this manner the Oh number increases. On the other hand, at constant Oh number, spray or atomization can be achieved only by increasing flow rate (D. Riestenberg, 2004).

A fluid dynamic interpretation of the SAS process was firstly proposed by Lengsfeld et al. (Lengsfeld et al., 2000), that studying the evolution of the liquid surface tension in jets of immiscible, partially miscible and miscible fluids injected into compressed carbon dioxide, found that in conditions above the mixture critical point liquid droplets never form, because the surface tension vanishes before the jet break-up occurs. Afterwards, Sarkari et al. (Sarkari et al., 2000), Dukhin et al. (Dukhin et al., 2005, Dukhin et al., 2003), Badens et al. (Badens et al., 2005), Gokhale et al. (Gokhale et al., 2007), and Obrzut et al. (Obrzut et al., 2007) studied the jet atomization in pressurized gases, observing that at pressures slightly above the MCP, a transition between multi-phase (formation of droplets after jet break-up) and single phase mixing (no formation of droplets) takes place, whereas at completely developed supercritical conditions, turbulent single-phase mixing dominates.

II.3 Mass transfer

In SAS process the mass transfer between the antisolvent and the liquid solvent is promoted by jet break-up and atomization of the liquid phase in order to produce a very large contact surface. For this purpose, different kind of injection devices are described in literature (Teipel, 2006). Droplets diameter depends mainly on Reynolds number, viscosity, surface tension, operating pressure and temperature. The mass transfer of $scCO_2$ into the droplets is particularly fast, since CO_2 is highly soluble in organic solvents and shows gas-like diffusion properties that are characteristic for supercritical fluids (De Marco et al., 2012).

Micrometric spherical particles are generated from the micrometric droplets formed after jet break-up and subsequent atomization of the liquid phase. The very fast sorption of $scCO_2$ in the liquid phase (and, in a minor extent, the evaporation of the solvent into the antisolvent) produces the precipitation of the solid. The process is very fast and the precipitates are amorphous spherical particles since each droplet works as a micro-precipitator, confined from the surroundings (at least at the beginning of the process) by the surface tension of the liquid phase that forces all the material to maintain its original shape. Spherical microparticles morphology was observed by SAS only in a limited range of pressure and temperature conditions, positioned relatively near above the MCP pressure of the system solvent-antisolvent. At these operating conditions, the interfacial tension of the injected solution starts from the value typical of the liquid and progressively reduces to zero when equilibrium conditions are achieved.

In some cases, expanded microparticles were observed, when SAS process was operated at gaseous conditions, below the MCP of the system solvent-antisolvent. The formation mechanism for this particle morphology can be considered a variation of the one proposed for microparticle formation. At these process conditions, when droplets are formed by atomization, the diffusion of CO_2 into the droplets is larger than the evaporation of the solvent into the bulk CO_2; as a consequence, droplets expand. Therefore, as soon as the mass transfer continues, the volume of the droplet increases while the residual surface tension allows the droplets to keep their spherical shape. The solid starts to precipitate near the internal droplet surface and, then, accumulates forming a solid shell. In this manner, empty core, expanded microparticles (also called “balloons”) can be formed. Expanded microparticles (EMP) can be characterized by a uniform surface and internal structure or by a nanostructured surface formed by nanometric particles inter-connected to form the final structure: these different microstructures can be formed as a result of different nucleation and mass transfer times (Chávez et al., 2003b). EMP with the nanostructured surface are also less stable than the ones with the uniform, smooth structure; therefore, they are more frequently observed as broken. The nanostructured EMPs tend to break in form of disconnected nanoparticles; whereas, uniform surface EMPs break in pieces that maintain the recollection of the spherical structure. When nucleation is faster than diffusion, the process is characterized by a diffusion limited precipitation front. In this case, expanded microparticles with a discontinuous structure, formed by nanoparticles, were obtained. On the contrary, when the diffusion is fast and the nucleation slow, the process is characterized by a uniform precipitation throughout the droplet, that leads to the formation of expanded microparticles with a continuous surface (E. Reverchon, 2008).

When SAS operation was performed far above the critical pressure, nanoparticles are formed. Several authors showed that, at these process conditions, the mixing mechanism between the liquid flow and the bulk CO_2 is gas mixing followed by precipitation. In this case, droplets are not formed at the exit of the injector, since the liquid solution mixes with the antisolvent in a single phase mixing process, from which solids can nucleate and grow.

The analysis of microparticle and nanoparticle formation mechanisms by SAS is, therefore, in favor of jet break-up and mutual diffusion between the solvent and the antisolvent when microparticles are formed, and in favor of gas mixing and particle nucleation and growth, in the case of nanoparticle formation. Since these two mechanisms operate at two contiguous pressure levels, a competition occurs between them. To analyze this competition, two characteristic times were defined: the time of jet break-up (τ_{jb}) and the time necessary for the complete vanishing of the surface tension between the injected solution and the surrounding antisolvent (τ_{st}). When $\tau_{jb} < \tau_{st}$, the jet breaks-up into droplets and, as a final result, spherical microparticles are produced; when $\tau_{st} < \tau_{jb}$, the jet breaks-up (widens) into a single-phase mixing steam and no droplets are formed and the precipitation is obtained by gas-to-particles nucleation and growth.

II.4 Interactions of phase equilibria, jet fluid dynamics and mass transfer during supercritical antisolvent micronization

Elastic light scattering technique

In order to elucidate the interactions of phase equilibria, jet fluid dynamics, mass transfer and the characteristics of the generated particles, jet behaviors during SAS precipitation have been studied using elastic light scattering (De Marco et al., 2012, Reverchon et al., 2010) technique. The advantages of optical measurement techniques are their non-invasive measurement principle (they do not alter the investigated processes), their high temporal (down to ns) and spatial resolution (down to µm) and their high sampling rates (up to kHz) (Braeuer et al., 2011).

Elastic light scattering technique was used to investigate the evolution of the interfacial tension between the injected solvent and the bulk CO_2 (De Marco et al., 2012).

In the elastic light scattering, the wavelength of the scattered light is not altered by the scattering process. When light is scattered from phase boundary, like for example the formation of a multi-phase flow in SAS process, this mechanism is called Mie scattering; whereas, when light is scattered from inhomogeneity, such as composition inhomogeneities, the mechanism is called Rayleigh scattering.

When the injected solvent into the bulk CO_2 breaks-up into drops at a certain distance from the nozzle (Figure II.4), the first section of the jet is homogeneous and cannot be detected by the microscope (part a); after that, the jet begins to be disturbed and Rayleigh scattering signals are detected (part b); eventually, when drops are formed, Mie scattering signals from phase boundaries are detected (part c).When the solvent injected into the bulk CO_2, instead, is atomized into small droplets, Mie scattering signal allows to obtain the image of a white jet (Figure II.4-2). On the other hand, when gas mixing occurs, Mie scattering signals are not produced since there are not phase boundaries, whereas Rayleigh scattering signal is detected at the edges of the jet and at a certain distance from the nozzle, since close to it the solvent has not yet mixed with the bulk CO_2 and the signal is not observed (Figure II.4-3).

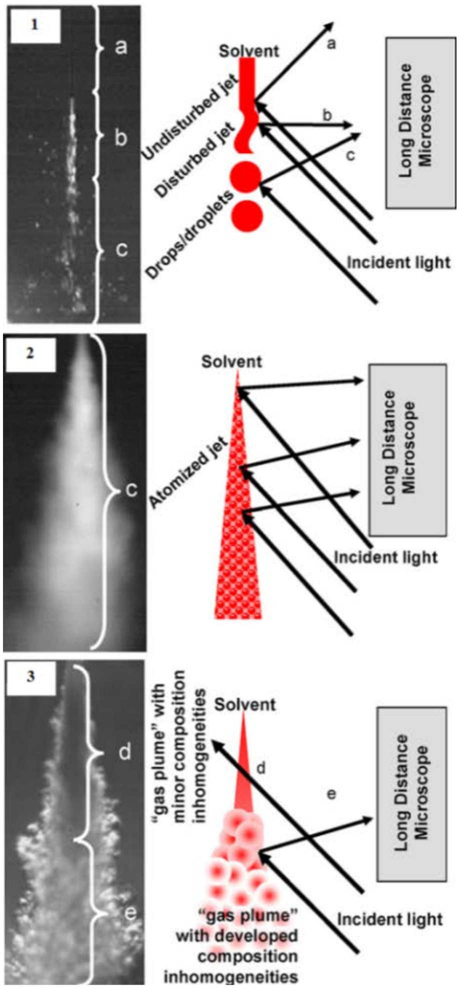

Figure II. 4 *Scattering phenomena related to jet mixing (from(Reverchon et al., 2010)).*

With the light scattering technique, De Marco et al. *(De Marco et al., 2012)* performed jet experiments to analyze fluid dynamic behavior of the solvents most frequently used in SAS processing: chloroform (CHF), acetone (AC), N-methylpyrrolidone (NMP), ethanol (EtOH) and dimethylsulfoxide (DMSO). The jets images that they obtained are summarized in Figure II.5:

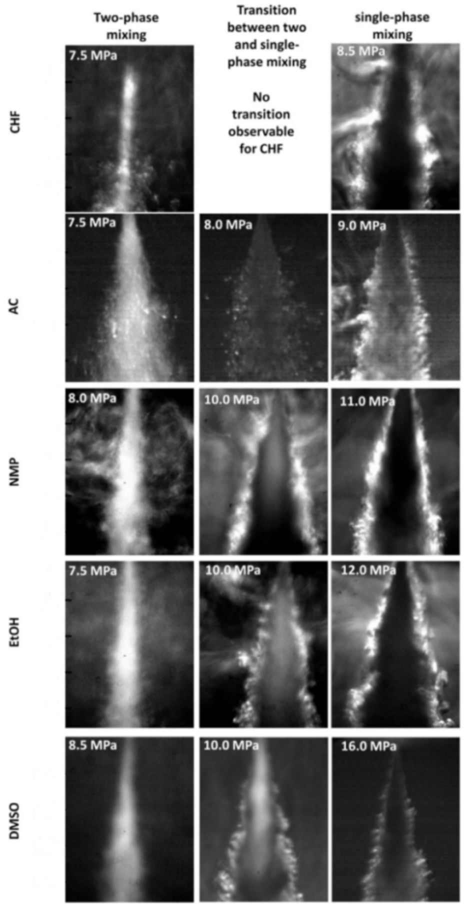

Figure II. 5 *Jet images of CHF, AC, NMP, EtOH and DMSO injected at 313 K with a flow rate of 2.5 mL/min through the Ø = 80 µm nozzle into* $scCO_2$ *(from(De Marco et al., 2012).*

In Figure II.5, the left column shows the jet at subcritical conditions, where the liquid is atomized into drops; the middle column shows the jet at conditions near above the MCP of the system solvent/antisolvent, where there is a transition from a multi-phase to a single-phase mixing between the liquid and the bulk CO_2; the right column shows the jet at conditions far above the MCP, i.e. in a single-phase mixing. As it is possible to observe from Figure II.5,the pressure range at which the transition takes place depends on the type of the solvent used. Indeed, for CHF the transition is absent and for AC it is very sharp, therefore, microparticles cannot be produced with SAS process using these solvents. For the other investigated solvent, instead, the transition occurs on a wide pressure range, especially in the case of DMSO.

Combined elastic and inelastic scattering

Elastic light scattering technique is useful to study the jet behavior of solvents in contact with compressed CO_2 (Reverchon et al., 2010), but if a solution is injected instead of a solvent, in addition to the signals from the liquid/fluid interface, there is the presence of the signals from the solid/fluid interface. In this case, a combination of elastic and inelastic (Raman) light scattering techniques has to be applied (Braeuer et al., 2011). These techniques qualify for in situ, two-dimensional and temporally resolved detection of the location of first particle precipitation, the partial density of all species in the system, the supersaturation and the overall mixture composition (Dowy et al., 2011, Braeuer et al., 2010).

When photons are scattered from a molecule, a part of them is scattered elastically and a part is scattered inelastically. In this last case the light is scattered with a higher or a lower wavelength with respect to the incident light (Raman shift), as shown in Figure II.6 (Dowy et al., 2009).

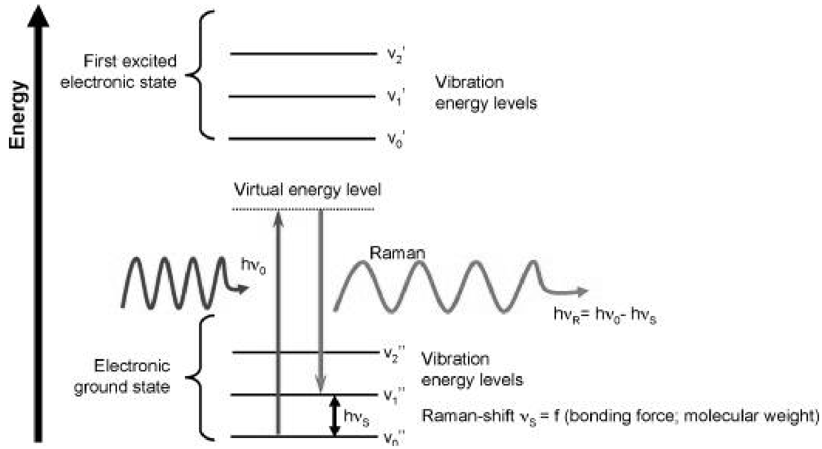

Figure II. 6 *Principle of Raman scattering, h: Planckis constant, ν: frequency of the light wave, hν: energy of the light wave (from(Dowy et al., 2009)).*

Since a specific “finger print” is associated to each molecule, it is possible to identify different species from a Raman spectrum.

From the Raman scattering working equation it is possible to deduce that the Raman signal intensity is a linear function of the molecular number density n and, therefore, of the partial density ρ *(Decker et al., 1998, Gu et al., 2000, Mayer et al., 2003, Eckhardt and Wagner, 1966)*:

$$I \propto n \propto \rho \quad (1)$$

Determination of the partial density

In order to determine the CO_2 partial density, the Raman signals of the solvent and of CO_2 are measured simultaneously with two cameras. However, since the Raman signals of the solvent can interfere with the Raman signal of CO_2, a crosstalk correction is carried out. Firstly the Raman signal of the solvent is detected; then, the Raman signal of CO_2 is determined and, finally, from this last value the solvent signal is subtracted to obtain the pure CO_2 signal, as shown in Figure II.7 *(Dowy et al., 2009)*.

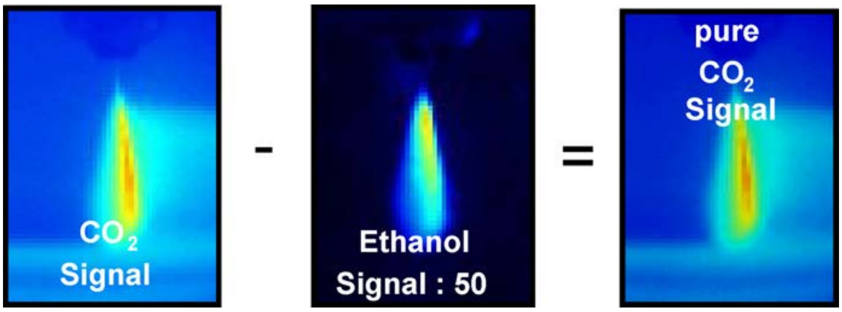

Figure II. 7 *Crosstalk correction of the CO_2 Raman signal interfered by the ethanol Raman signal (from (Dowy et al., 2009)).*

Determination of mole fraction

In order to quantitatively characterize the mixing process, a calibration has to be performed to correlate the measured Raman signal intensities with the mixture composition.

During the calibration, the temperature and the pressure values are chosen in order to have a homogeneous system above the MCP. For each measurement point, a known amount of solvent is sent into the chamber and the vessel is pressurized with CO_2 up to the chosen pressure. Knowing the exact mass of solvent and CO_2, measured by a coriolis flow meter for CO_2, it is possible to calculate the mole fraction of the homogeneous mixture inside the SAS. For each mole fraction, 100 single-shot images were taken simultaneously with the CO_2 and solvent Raman cameras. In the case of a solvent mixture AC/EtOH in contact with compressed CO_2, the detected Raman signal intensities are I_{CO2} for CO_2 and $I_{EtOH}+I_{AC}$ for the solvent mixture. The 100 background corrected single-shot images were used to calculate a mean Raman intensity image $I_{CO2}/(I_{CO2}+I_{EtOH}+I_{AC})$ and its standard deviation. As all Raman intensities are directly proportional to the molecular number densities of the probed species, the Raman intensity ratio is a function of the CO_2 mole fraction x_{CO2} (Dowy et al., 2009):

$$\frac{I_{CO2}}{I_{CO2}+I_{EtOH}+I_{AC}} = f\left(\frac{n_{CO2}}{n_{CO2}+n_{EtOH}+n_{AC}}\right) = f(x_{CO2}) \qquad (2)$$

Plotting each value of the Raman intensity ratio as a function of the corresponding CO_2 mole fraction, it is possible to obtain the calibration curve. Having calibrated the signal intensity ratio, the calibration data can be used to determine the mole fraction distribution along the probe volume during the injection experiment.

Location of first detectable particle generation

When pure solvent is injected into the bulk CO_2, the liquid/fluid interface of the droplets provide elastic light scattering signals, as shown in Figure II.8a. when a solution is injected instead of pure solvent the presence of a new phase boundary, the solid/fluid interface, make the elastic light scattering signal stronger, as reported in Figure II.8b. In order to identify the location of first detectable particle precipitation (LFDPP) the figures with and without solute are compared: only the pixels in Figure II.8b that have an intensity value between 10 and 20% higher than the intensity value of the same pixel in Figure II.8a are taken into account *(Rossmann et al., 2012).* The resulting image is shown in Figure II.8c.

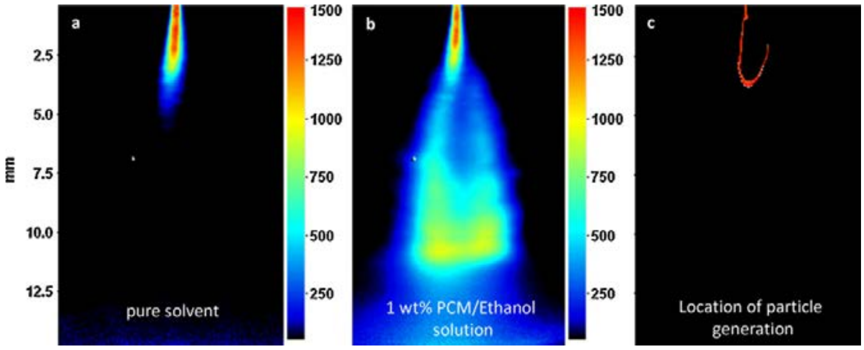

Figure II. 8 *Evaluation procedure for the identification of the location of first detectable particle generation (LFDPP) (from (Rossmann et al., 2012)).*

Chapter III
Analytical methods

III.1 Morphology analyses

III.1.1 Scanning electron microscope field emission

A Field Emission Scanning Electron Microscope (FESEM model LEO 1525; Carl Zeiss SMT AG, Oberkochen, Germany) was used to study the morphology of the produced particles. Samples were dispersed on a carbon tab, previously stuck to an aluminum stub and covered with gold (layer thickness 250 Å) using a sputter coater (model 108 A; Agar Scientific, Stansted, United Kingdom).

III.1.2 Particle size analysis

Particle size distribution (PSD) of the powders were measured from FESEM photomicrographs using the Sigma Scan Pro Software (release 5.0, Aspire Software International Ashburn, VA). Approximately 1000 particles, taken at high enlargements and in various locations inside the precipitator, were analyzed in the elaboration of each particle size distribution. Histograms representing the particle size distribution were fitted using Microcal Origin Software (release 8.0, Microcal Software, Inc., Northampton, MA).

The PSDs of the particles were also calculated by dynamic laser scattering (DLS) using a Zetasizer (NanoZS Malvern Instrument, UK) equipped with a He-Ne laser operating at 4.0 mW and 633 nm, that measures the hydrodynamic diameter of the particles. To perform these measurements, particles were suspended in a dispersant solvent, which varies depending on the analyzed solute.

III.2 Solid state analyses

III.2.1 X-Ray Diffraction (XRD)

X-ray diffractograms of the samples were recorded using an X-ray powder diffractometer (model D8 Discover; Bruker, USA) with a Cu sealed tube source. Samples were placed in the holder and flattened with a glass slide to ensure a good surface texture. The measuring conditions were: Ni-filtered CuKα radiation, λ=1.54 Å, 2θ angle varying in a range which depend on the kind of solute, with a scan rate of 0.3 s/step and a step size of 0.02°.

III.2.2 Differential scanning calorimetry (DSC)

Thermograms of the samples were obtained using a differential scanning calorimeter (DSC, model TC11, Mettler Toledo, Inc., Columbus, USA) using Mettler STARe system. Fusion temperature and enthalpy were previously calibrated with an indium standard (melting point, 429.6 K, enthalpy of fusion 28.52 J/g). Powder samples (5 ± 0.5 mg), prepared in duplicates, was accurately weighed, crimped in an aluminum pan and heated in a temperature range depending on the analyzed material at 5 K/min under a nitrogen purge (50 mL/min).

III.3 Stability and denaturation analyses

III.3.1 Fourier transform infrared FT-IR

Fourier transform infrared (FT-IR) spectra were obtained via M2000 FTIR (MIDAC Co, Costa Mesa, CA), at a resolution of 0.5 cm^{-1}. The scan wavenumber range was 4000–400 cm^{-1}, and 16 scan signals were averaged to reduce the noise. The powder samples were ground and mixed thoroughly with potassium bromide (KBr) as infrared transparent matrix. KBr discs were prepared by compressing the powders in a hydraulic press. Composition bands of the amide I band were determined using the inverted second derivative and all spectra were smoothed using a 13-point Savitzky–Golay smoothing function to remove white noise.

III.3.2 High Performance Liquid Chromatography

The influence of the process on the solute degradation was measured using HPLC analysis (model 1200 series; Agilent Technologies Inc., Italy). The elution was obtained using a column filled with a solid adsorbent material, whose model varies according to the analyzed material. The column was equilibrated with a mobile phase consisting of one or more eluents. The solute was dissolved in a proper solvent, filtered with a 0.2 μm membrane syringe and detected at a wavelength that is specific for the analyzed material. All chromatographic analyses were carried out at room temperature.

III.3.3 Enzymatic activity

Enzymatic activity was determined using the decrease in the optical dispersion at 450 nm of a *Micrococcus lysodeikticus* suspension, according to the method proposed by Shugar (Shugar, 1952). It consists of the preparation of a dispersion of Micrococcus lysodeikticus in a 66 mM phosphate buffer pH 6.2 (0.36 g/L); 0.1 mL of the enzyme containing solution (1 mg/mL) were added to 2.7 mL of this suspension. The decrease in 3 min of the OD_{450nm} was monitored. Absorption spectra were acquired using a UV-vis Cary 50 spectrophotometer (Varian, Milan, Italy).

III.3.4 Active principle ingredient entrapment efficiency and release

Drug entrapment efficiency and powder dissolution studies were performed using an UV-vis spectrophotometer (model Cary 50, Varian, Palo Alto, CA). Accurately weighted samples containing an equivalent amount of API were suspended in 1.5 mL of phosphate buffered saline solution (PBS) with 0.5% of Tween-80 and placed into a dialysis sack; it was then incubated in 300 mL of PBS at pH 7.0, continuously stirred at 250 rpm and 310 K. Each analysis was carried out in triplicate and the proposed curves are the mean profiles. API entrapment efficiency was calculated by UV–vis analysis, measuring the absorbance obtained in the release medium at the end of the drug release; i.e., when all API was released from the microspheres to the outer water phase. The absorbance was, then, converted into API concentration, using a calibration curve.

III.4 Solvent residue analysis

Solvent residues were measured using a headspace sampler (model 7694E, Hewlett Packard, USA) coupled to a gas chromatograph equipped with a flame ionization detector (GC-FID, model 6890 GC-SYSTEM, Hewlett Packard, Agilent Technologies Mfg. Gmbh & Co. KG, USA). The solvents were separated using two fused silica capillary columns connected in series by press-fit: the first column (model Carbowax EASYSEP, Stepbios, Italy) connected to the detector, 30 m length, 0.53 mm i.d., 1 µm film thickness and the second (model Cp Sil 5CB CHROMPACK, Stepbios, Italy) connected to the injector; 25 m length, 0.53 mm i.d., 5 µm film thickness. GC conditions were: oven temperature at 433 K for a total time equal to 8.8 min. The injector was maintained at 523 K (split mode, ratio 5:1), and helium was used as the carrier gas (2 mL/min). Headspace conditions were: equilibration time, 9 min at 443 K; pressurization time, 0.3 min; loop fill time, 0.4 min. Head space samples were prepared in 20 mL vials filled with 50 mg of drug dissolved in water. Analyses were performed on each batch of processed drug, in triplicates.

Chapter IV
Study of the precipitation mechanisms involved in SAS process

IV.1 Study of jet behavior of solvent mixtures

Materials

Acetone (AC, purity 99.8 %), ethanol (EtOH, purity 99.8 %), dimethylsulfoxide (DMSO, purity 99.5 %), N-methyl-2-pyrrolidone (NMP, purity 99.0 %), were supplied by Sigma-Aldrich (Italy). Carbon dioxide (CO_2, purity 99 %) was purchased from S.O.N. (Società Ossigeno Napoli). All materials were used as received.

IV.1.1 Elastic light scattering

Elastic light scattering setup

A light scattering setup was used to investigate the behavior of the injected solvent and the evolution of the interfacial tension between the injected solvent and the bulk CO_2; it was coupled to the SAS apparatus as schematized in the right part of Figure IV.1. The description of the apparatus is taken from *(Reverchon et al., 2010*). The solvent jet was illuminated by a high power white light source from a certain angle from below via a mirror. A long distance microscope was used to image the jet on the camera by detecting the light scattered elastically in backward direction. The exposure time of the camera had to be set below 50 µs to acquire sharp images. Longer exposure times are too long to freeze the turbulent motion of the jet and consequently result in smeared images. To compensate the low signal levels detectable during exposure times shorter than 50 µs, 4 pixels of the camera chip were binned together to one superpixel (two in horizontal direction and two in vertical direction). After binning, the camera chip of 1376 (vertical) times 1056 (horizontal) single pixels can be considered to be composed of 688 (vertical) times 528 (horizontal) pixels. With the long distance microscope 25 cm away from the jet center axis, an approximately 1.7 mm wide and 2.3 mm high section of the jet center plane directly below the nozzle exit could be observed. Consequently, an area of 3.3 times 3.3 μm^2 is imaged onto one binned superpixel. Summarizing all, these measures allowed the detection of reliable signal levels at sufficiently short exposure times with a still sufficiently high local resolution.

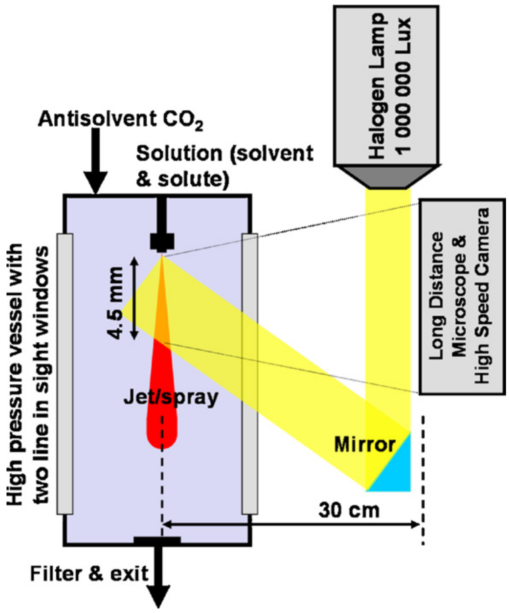

Figure IV. 1 *Schematics of the optical setup(from (Reverchon et al., 2010)).*

Comparison of jet behavior of solvent mixtures AC/DMSO, AC/EtOH and AC/NMP

The evolution of the interface between the injected solvent and the $scCO_2$ was analyzed for the solvent mixtures AC/DMSO, AC/EtOH and AC/NMP for different mixture compositions and varying the operating pressure from subcritical to supercritical conditions using the elastic light scattering technique, previously discussed. All the experiments were carried out at 313 K, using an 80 µm diameter nozzle, with a liquid flow rate of 2.5 mL/min and with a CO_2 flow rate equal to 7 kg/h (to obtain a mole fraction of CO_2 in the precipitator equal to 0.99). These process conditions assure that, independently of the pressure, the operating point is located outside the miscibility gap of the system CO_2-mixture of solvents. Figure IV.2, IV.3 and IV.4 show jet images of solvent mixtures of AC/DMSO, AC/EtOH and AC/NMP, respectively, in $scCO_2$ at the previously indicated process conditions. The left column shows jet images at subcritical conditions (pressures lower than the mixture critical point) at which a two-phase mixing between the liquid phase and the bulk CO_2 takes place. At subcritical conditions, when the jet break-up occurs, the liquid jet is atomized into droplets; the interfacial tension vanishing time τ_i is higher than the jet break-up time τ_{jb}, therefore, mixing occurs in a two-phase flow (liquid droplets mixed with bulk carbon dioxide). The right column shows jet images where mixing occurs in a single-phase flow, typical of completely developed supercritical conditions. Indeed, in this case, the interfacial tension between the solvent and the bulk CO_2 has reached the zero value before the jet break-up. Therefore, liquid droplets do not form and a completely developed single-phase mixing can be observed. The minimum pressure at which no phase boundaries (droplets) are detectable is the one indicated in the images represented in the right column of Figure IV.2, IV.3 and IV.4. The jet images reported in the middle column are related to the transition from a two-phase to a single phase mixing flow that, in terms of pressure range, depends on the kind of solvent. In the region of transition, the two-phase mixing flow can be observed in the vertical center of the jet (high elastic light scattering intensities can be detected from interfaces), whereas a single-phase mixing flow can be observed in the outer jet mixing regions (low elastic light scattering intensities can be detected from refractive-index-gradients).

Summarizing, adding a narrow transition solvent (AC) to another solvent (like DMSO, EtOH or NMP), the pressure at which the transition from a two-phase to a single-phase mixing flow takes place decreases, if compared to the pressure at which this transition occurs when these solvents are used alone.

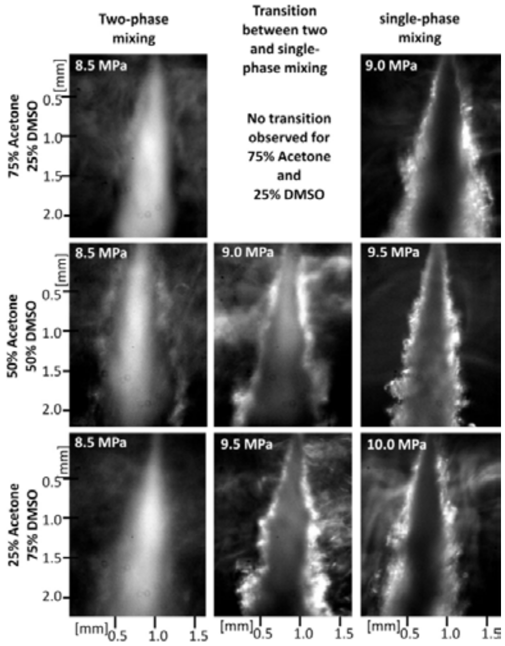

Figure IV. 2 *Jet images of solvent mixtures of DMSO and AC injected at 313 K with a flow rate of 2.5 mL/min through a Ø = 80 µm nozzle into* $scCO_2$ *(De Marco et al., 2012).*

In order to observe the differences in the mixing behavior between the pure solvents and the AC/DMSO mixtures in contact with compressed CO_2, Figure II.6 and Figure IV.2, have to be compared. From this comparison emerges that at 8.5 MPa, while pure AC jet was in the transition region, all mixtures are still in the two-phase region; on the other hand, at 10.0 MPa, while pure DMSO was in transition, the mixtures are already in single-phase region. Moreover, comparing the width of the transition region among the different AC/DMSO mixtures, it was possible to observe that this range enlarges increasing the DMSO content. Therefore, at pressures near above the MCP the mixing behavior is governed by DMSO, whereas far above the MCP the mixing behavior is governed by AC.

AC/EtOH mixtures

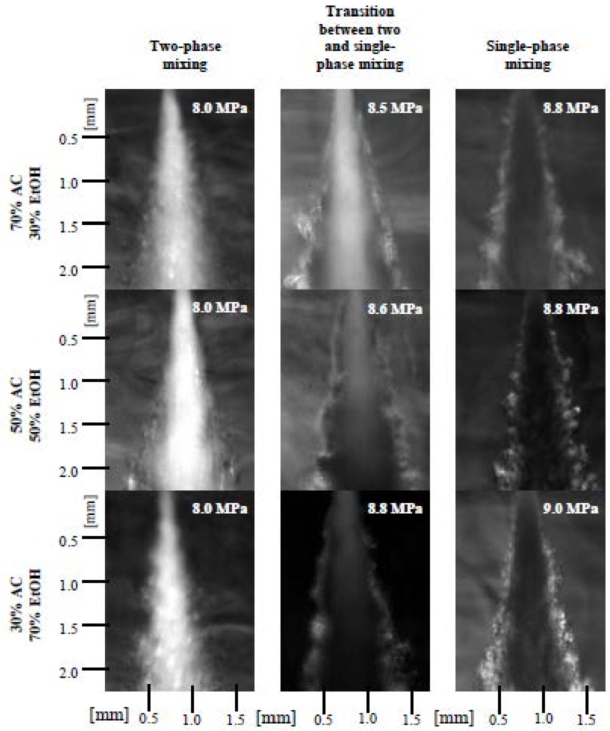

Figure IV. 3 *Jet images of solvent mixtures of EtOH and AC injected at 313 K with a flow rate of 2.5 mL/min through a Ø = 80 µm nozzle into* $scCO_2$ *(De Marco et al., 2015).*

In Figure IV.3, it can be observed that all the mixtures formed by AC and EtOH at 8.0 MPa are in the two-phase mixing region. Increasing EtOH content, the transition region from two-phase to one-phase behavior widens from 8.6 MPa for pure AC to 9.0 MPa for pure EtOH and the mixture containing 70 % EtOH.

AC/NMP mixtures

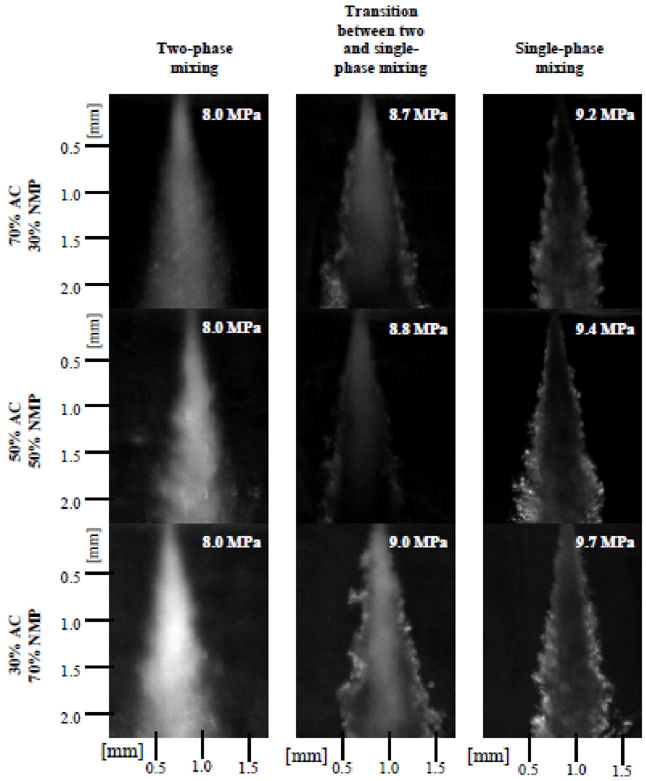

Figure IV. 4 *Jet images of solvent mixtures of NMP and AC injected at 313 K with a flow rate of 2.5 mL/min through a Ø = 80 µm nozzle into* $scCO_2$ *(De Marco et al., 2015).*

In Figure IV.4, the jets of the mixtures formed by acetone and NMP, when in contact with $scCO_2$, are shown. Also in the case of the mixture formed by these two solvents, at 8.0 MPa, a two-phase mixing can be detected for all the mixture compositions. Increasing NMP content (whose transition region from two-phase to one-phase mixing behavior is wider with respect to pure EtOH), it can be noted that the span of the transition region from two-phase to one-phase behavior increases from 8.6 MPa (pure AC) to 9.7 MPa (for 70 % NMP). For pressures larger than 9.2 MPa (in the case of AC-rich mixture) and 9.7 MPa (in the case of the NMP-rich mixture) no signals originating from two-phase mixing zones are detectable; therefore, one-phase mixing occurred.

IV.1.2 Combined elastic and inelastic light scattering

Combined elastic and inelastic light scattering setup

In combined elastic and inelastic light scattering setup a three-camera system is used. The description of the apparatus is taken from *(Dowy et al., 2010)*. Two cameras are required to detect the inelastic Raman signals, which are scattered from the organic solvent and the CO_2 molecules and, therefore, indicate the distribution of the solvent and the antisolvent. The third camera is taken to detect the elastic light scattering, which comes from phase boundaries and, therefore, indicates the presence of a multi-phase flow. The light scattering processes are excited with a pulsed frequency-doubled Nd:YAG laser with maximum irradiation of 650 mJ per laser pulse at a wavelength of 532 nm, a temporal pulse width of 10 ns (FWHM) and a beam diameter of 9 mm.

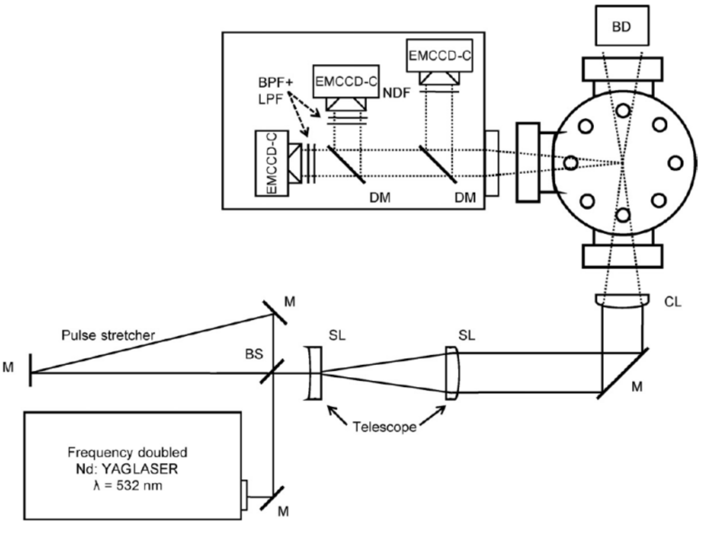

Figure IV. 5 *Schematic of the experimental setup, (M: mirror, BS: beam splitter, SL: spherical lens, CL: cylindrical lens, BD: beam dump, DM: dichroitic mirror, NDF: neutral density filter, BPF: band pass filter, LPF: long pass filter, EMCCD-C: electron multiplying charge coupled device camera) (from (Dowy et al., 2010)).*

On the detection side, three electron multiplying charge coupled device (EMCCD) cameras equipped with CCD chips of 658×496 pixels were used with a 2×2 binning for image acquisition. The area of 135 µm×135 µm from the observation plane (laser light sheet) inside the SAS chamber was imaged onto one binned pixel of the CCD-chip. For the separation of the Raman and the Mie signals, two dichroitic long pass beam splitters were integrated into the detection path. The first beam splitter separates the elastically scattered light at 532 nm from the Raman signals of organic solvent and CO_2 which are shifted to larger wavelengths. The second dichroitic long pass beam splitter separates the CO_2 vibrational Raman signal at 574.4 nm from the CH vibrational Raman signal of ethanol at 630.2 nm. As the elastic scattering process is more intense by several orders of magnitude than the inelastic Raman scattering process, the elastically scattered light was attenuated by neutral density filters mounted onto the object lens of the respective camera. The suppression of interferences from elastically scattered and reflected laser light is one of the main challenges in Raman imaging. Therefore, each Raman camera is equipped with a combination of a long pass filter and a narrow band pass filter, which is adjusted to the particular Raman signal wavelength of CO_2 and solvent. The long pass filter suppresses the elastic light scattering interferences, whereas the narrow band pass filter assures the pure detection of the corresponding Raman signal. The CO_2 band pass filter has a bandwidth (FWHM) of 1 nm with a transmission of 31 % and the CH band pass filter has a bandwidth (FWHM) of 10 nm with a transmission of 17 %. In order to obtain information on the composition distributions and phase boundaries in the highly dynamic SAS mixing process, a two dimensional Raman and an elastic light scattering technique is applied.

For the experimental determination of the jet breakup, the phase boundary or interface between the injected liquid solution and the supercritical CO_2 is the most appropriate variable that can be considered. The relaxation of this phase boundary from the nozzle exit hole downstream is a transient process and depends on the diffusion between the solvent and the compressed CO_2 (Dukhin et al., 2003). According to equilibrium thermodynamics, the phase boundary does not exist above the mixture critical point. Due to non-equilibrium conditions during mixing, the transient phase boundary weakens between the inlet of the liquid and its transformation to a gas-like mixture. Parallel with the decrease of the phase boundary, jet breakup of the destabilized jet and disintegration of the liquid solution takes place (Bellan, 2000). In the performed experiments, the transient interface of the injected liquid solution disappears within a short distance to the nozzle exit.

From a thermodynamic perspective, nucleation from a homogenous supersaturated solution is described by an increase in the Gibbs free energy for the formation of the nucleus solid surface and a decrease in free energy for the phase transformation (Myerson, 1993). The rate of nucleation and the critical size of the stable nucleus are related to the level of supersaturation, which – under these circumstances - is the driving force for particle formation (Bristow et al., 2001, Mukhopadhyay and Dalvi, 2005). Crystallization is a two-step process, which incorporates nucleation and growth. The critical nucleus is a threshold size for which the smaller ones disappear and the larger ones grow (Debenedetti, 1990). The optical Mie scattering method applied does not allow to resolve individual nuclei and their origin. Nevertheless, it is able to provide evidence of the presence of particles in fluids down to 50 nm. The light intensity from a particle-laden bulk fluid is dependent on the size and the number density of the solid scatters. Information about the location of particle nucleation and growth can be extracted from the Mie signals (Dowy et al., 2010, Rossmann, 2015).

Combined elastic and inelastic scattered light measurements

With the combined elastic and inelastic light scattering setup, it is possible to study the behavior of the system solvent mixture+CO_2+solute during SAS process. During the experiments, it was measured the CO_2 molar fraction (x_{CO2}) over the detected area (in and around the jet) and the location of first detectable particle precipitation (LFDPP), varying the pressure from 7 to 16 MPa at 313 K. The PVP concentration was fixed equal to 0.5 % wt, whereas different mixtures of ethanol and acetone were used as solvent. Indeed, ethanol is a good solvent for PVP whereas acetone a poor one; the solvation power of the EtOH/AC 50/50 wt % mixture is between the ones of the pure solvents. In particular, it was analyzed the behavior of the jet for injected solutions containing PVP in: pure EtOH, EtOH/AC 50/50 % mixture, EtOH/AC 30/70 % mixture, EtOH/AC 5/95 % mixture. The solution flow rate was fixed at 2 mL/min with a CO_2 flow rate of 200 g/min and, in order to have a constant CO_2 molar fraction x_{CO2}, it was considered only the second click of the cameras after taking the background (100 photos were taken for a good resolution of the images).

Effect of the operating pressure

The first effect taken into account was the pressure; in fact, experiments from 7.5 to 16 MPa were performed, injecting a solution of PVP dissolved in the mixture EtOH/AC 30/70 %. In Figure IV.6 it is possible to observe the different shape and length of the LFDPP in correspondence of some pressure values.

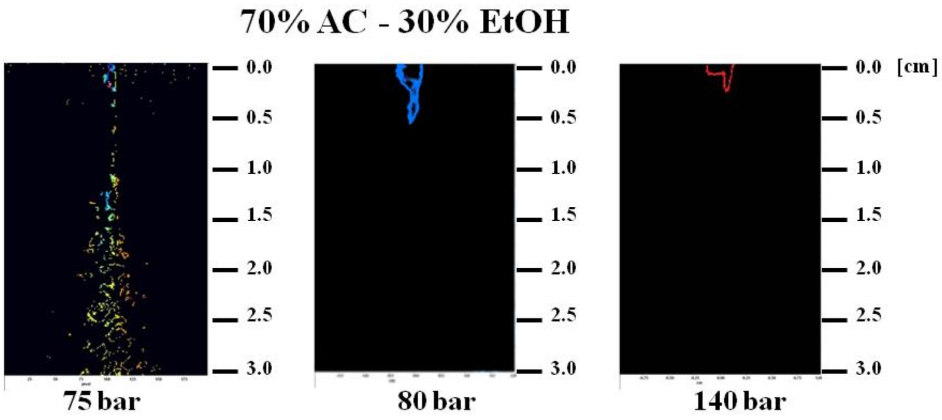

Figure IV. 6 *LFDPP of PVP in EtOH/AC 30/70 % obtained at 313 K, with a PVP concentration of 0.5 % wt, a solution flow rate of 2 mL/min, a* CO_2 *flow rate of 200 g/min and varying the operating pressure from 7.5 MPa to 14 MPa.*

At 7.5 MPa, the operating point is located below the mixture critical point (MCP) of the system solvent/CO_2; indeed the jet disintegrates into large drops after jet break-up. Looking at the other pressures, we can observe that the liquid/fluid interface disappears faster when we have a higher pressure; in fact, the LFDPP at 14 MPa is smaller than that obtained at 8.0 MPa. We can conclude that at higher pressure the formation of the particles occurred closer the nozzle exit.

Plotting the length of the LFDPP as a function of the pressure, we can see a decrease of the LFDPP when the pressure increases, as reported in Figure IV.7.

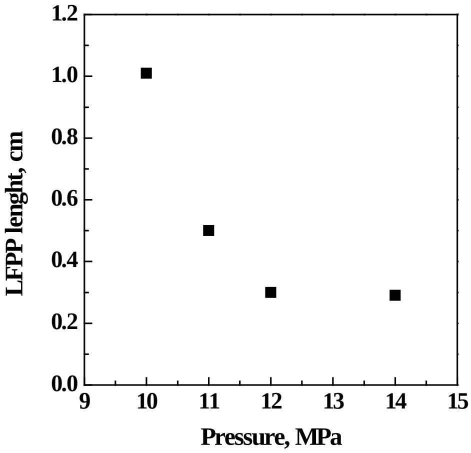

Figure IV. 7 *Length of the LFDPP of PVP in EtOH/AC 30/70 % obtained at 313 K, with a PVP concentration of 0.5 % wt, a solution flow rate of 2 mL/min, a CO_2 flow rate of 200 g/min and varying the operating pressure from 7.5 MPa to 14 MPa.*

Effect of the mixture composition

Afterwards, the effect of the mixture composition was studied, keeping constant the pressure at 10 MPa. In this set of experiments, the LFDPP of PVP in pure EtOH, in the mixture EtOH/AC 50/50 % and in EtOH/AC 5/95 was determined. The images obtained elaborating the data of these experiments are reported in Figure IV.8.

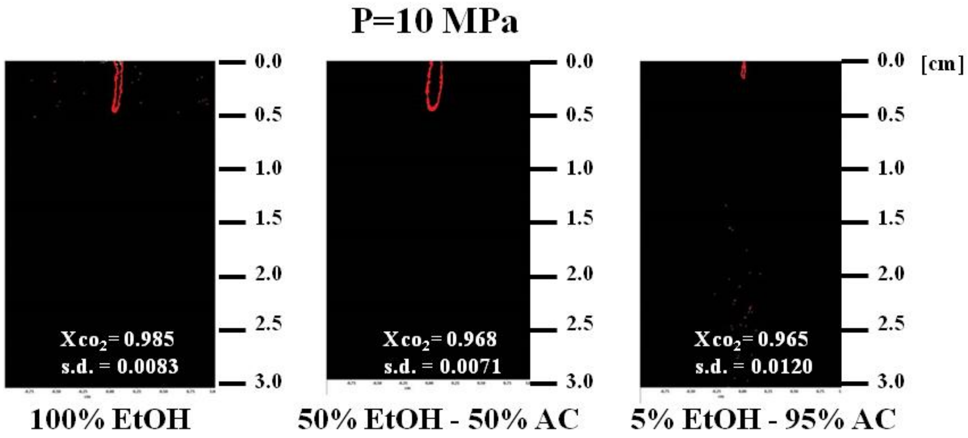

Figure IV. 8 *LFDPP of PVP in different mixtures of EtOH and AC at 313K, 10 MPa, with a PVP concentration of 0.5 % wt, a solution flow rate of 2 mL/min and a CO_2 flow rate of 200 g/min.*

In the diagram reported in Figure IV.9 the length of the LFDPP as a function of the mixture composition is reported. It is possible to observe that the length decreases when the amount of AC increases, probably this depends on the poor affinity of PVP towards acetone.

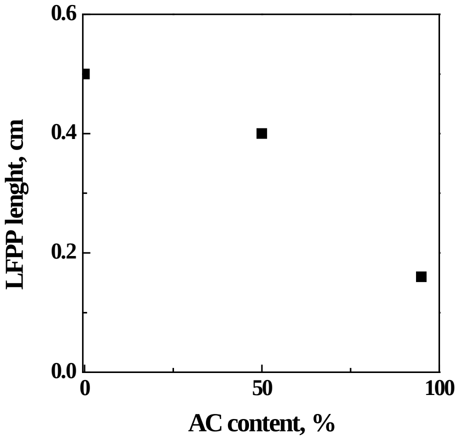

Figure IV. 9 *Length of the LFDPP of PVP varying the AC content in the mixture EtOH/AC at 313K, 10 MPa, with a PVP concentration of 0.5 % wt, a solution flow rate of 2 mL/min and a* CO_2 *flow rate of 200 g/min*

Plotting the CO_2 molar fraction measured into the jet as a function of AC content, it was observed that x_{CO2} decreases when the amount of acetone in the mixture increases.

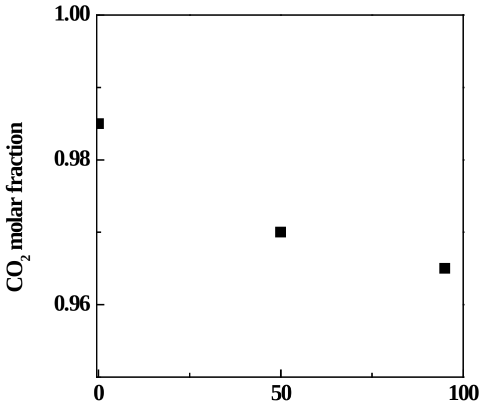

Figure IV. 10 CO_2 *molar fraction* (X_{CO2}) *varying the AC content in the mixture EtOH/AC.*

CO_2 molar fraction in the acetone jet is $x_{CO2} = 0.965$, whereas the molar fraction in the ethanol jet is $x_{CO2} = 0.985$. From these information it is possible to deduce that in presence of a good solvent for the solute, the amount of antisolvent needed for particle precipitation is higher than the amount of CO_2 needed in presence of a poor solvent. The value of CO_2 molar fraction when EtOH/AC 50/50 % is used as solvent is not intermediate between the values obtained for the pure solvent, but it is close to the one of acetone, i.e. $x_{CO2} = 0.968$. This experimental evidence is probably due to the fact that the solubility of PVP in the solvent mixture is affected more by acetone than ethanol.

IV.2 SAS precipitation experiments

Materials

Cellulose acetate (CA, MW ≈ 50000 g/mol), polyvinylpirrolidone (PVP, MW ≈ 10000 g/mol), acetone (AC, purity 99.8 %), ethanol (EtOH, purity 99.8 %), dimethylsulfoxide (DMSO, purity 99.5 %), N-methyl-2-pyrrolidone (NMP, purity 99.0 %), were supplied by Sigma-Aldrich (Italy). Carbon dioxide (CO_2, purity 99 %) was purchased from S.O.N. (Società Ossigeno Napoli). All materials were used as received.

SAS apparatus

In Figure IV.11, a scheme of the SAS laboratory plant used for the experiments is reported. It consists of two high pressure pumps used to deliver the liquid solution and supercritical CO_2, respectively. A cylindrical vessel of 500 cm^3 internal volume (I.V.) (i.d. = 5 cm) is used as the precipitation chamber. The liquid mixture is delivered to the precipitator through a thin wall 100 µm internal diameter stainless steel nozzle. Supercritical CO_2, after a preheating, is co-currently delivered to the precipitator through another port located on the top of the vessel. Pressure is measured by a test gauge manometer and regulated by a micrometering valve located at the exit of the precipitator. Temperature is set by a PID controller connected with electrically thin bands. A stainless steel frit (pore diameter of 0.1 µm) located at the bottom of the precipitator is used to collect the produced powder, allowing the CO_2-solvent-solution to pass through. A second collection vessel located downstream the micrometering valve, whose pressure is regulated by a backpressure valve, is used to recover the liquid solvent. At the exit of the second vessel, CO_2 flow rate and the total quantity of antisolvent delivered, are measured by a rotameter and a dry test meter, respectively.

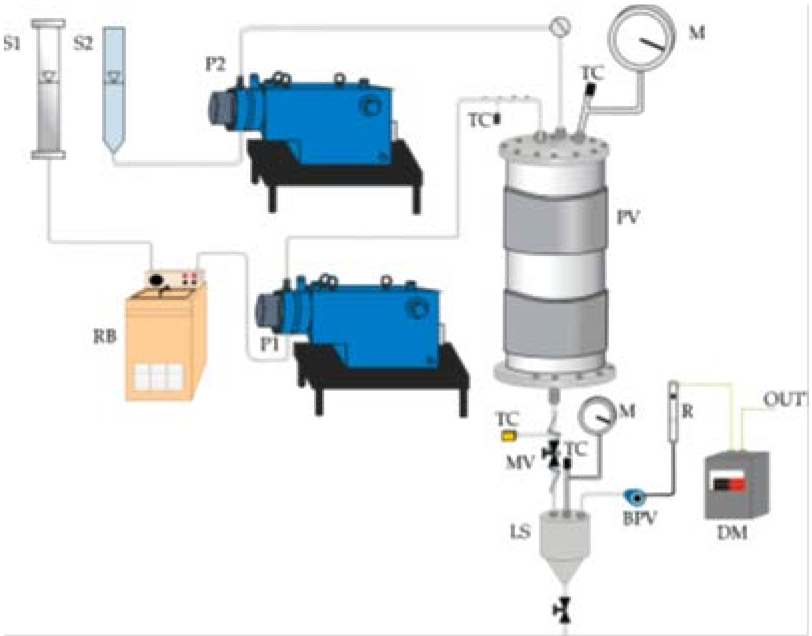

Figure IV. 11 *Schematic representation of a SAS apparatus. S1:* CO_2 *supply; S2: liquid solution; RB: refrigerating bath; P1, P2: pumps; TC: thermocouple; M: manometer; PV: precipitation vessel; MV: micrometering valve; LS: liquid separator; BPV: back pressure valve; R: rotameter; DM: dry test meter.*

SAS procedure

A SAS experiment begins delivering CO_2 to the SAS vessel until the desired pressure is reached; then, pure solvent is sent through the nozzle to the vessel for at least 15 min. When a quasi-steady state composition of solvent and antisolvent is realized inside the SAS vessel, the flow of the solvent is stopped and the liquid solution is delivered through the nozzle, producing the precipitation of the solute.

At the end of the solution delivery, supercritical CO_2 continues to flow, to wash the precipitator, eliminating the solution formed by the liquid solubilized in the supercritical antisolvent. If the final purge with pure CO_2 is not performed, the organic solvent contained in the fluid phase condenses during the depressurization step and can solubilize or modify the precipitates. At the end of the washing step, CO_2 flow is stopped and the precipitator is depressurized down to atmospheric pressure.

IV.2.1 SAS precipitation experiments on PVP

Solubility tests performed at room temperature showed that PVP solubility in AC, identified as a “poor solvent”, is about 10 mg/mL;

whereas, its solubility in the so-called “good solvents” is about 200 mg/mL in EtOH, 250 mg/mL in DMSO and 350 mg/mL in NMP. SAS experiments were, then, performed, precipitating PVP from mixtures, at different compositions, of AC/EtOH, AC/NMP and AC/DMSO. Preliminary tests showed that, when processed by SAS using EtOH, DMSO or NMP (solvents in which PVP is very soluble), PVP always precipitated in the form of microparticles, even at pressures well above the mixture critical point (MCP) of the systems organic solvent/carbon dioxide, corresponding to well-developed supercritical conditions. We may hypothesize that the addition of PVP strongly modifies the mixing behaviour and enlarges the transition region from two-phase to one-phase mixing regime. To control PVP particle size and eventually produce nanoparticles, we added acetone that features two characteristics as previously mentioned:

(1) AC is a “poor solvent” with respect to PVP;

(2) AC shows a sharp transition region between two-phase and one-phase mixing behavior.

The experiments were carried out at 10 MPa, 313 K, PVP concentration in the liquid solution (50 mL injected for each experiment) equal to 1 % wt, liquid flow rate equal to 2.5 mL/min, and a CO_2 molar fraction of 0.99. A list of the experiments performed indicating the solvent-mixtures used (and the related compositions), the morphology obtained, the mean diameter (m.d.) and the standard deviation (s.d.), is reported in Table IV.1. All the experiments were performed in triplicates.

Table IV.1 *SAS experiments performed on PVP at 313 K, 10 MPa and 1% wt (NP: nanoparticles; MP: microparticles; SMP: sub-microparticles).*

#	Solvent	Solvent mixture composition mass %	Morph	m.d. µm	s.d. µm
1	AC/EtOH	pure ETOH	MP	2.42	1.54
2		30/70	SMP	0.58	0.26
3		50/50	SMP	0.43	0.21
4		70/30	NP	0.22	0.16
5	AC/DMSO	pure DMSO	MP	3.80	2.41
6		30/70	NP	0.28	0.04
7		50/50	NP	0.25	0.09

8		70/30	NP	0.16	0.04
9	AC/NMP	pure NMP	MP	1.55	0.48
10		30/70	NP	0.31	0.14
11		50/50	NP	0.22	0.03
12		70/30	NP	0.11	0.03

The first set of experiments was performed using pure ethanol and the mixtures AC/EtOH at different percentages of the two solvents (# 1-4 in Table IV.1), to evaluate the effect of the content of AC in the mixture on PVP morphology and on the mean size of the particles. It is possible to observe that using pure ethanol (Figure IV.12a), well separated spherical microparticles were obtained; whereas, using EtOH/AC mixtures (the images reported in Figures IV.12b-IV.12d are taken at the same magnification), sub-microparticles and nanoparticles were produced; in particular, increasing the content of AC, the mean particle sizes decreases and the particle size distributions shrinks.

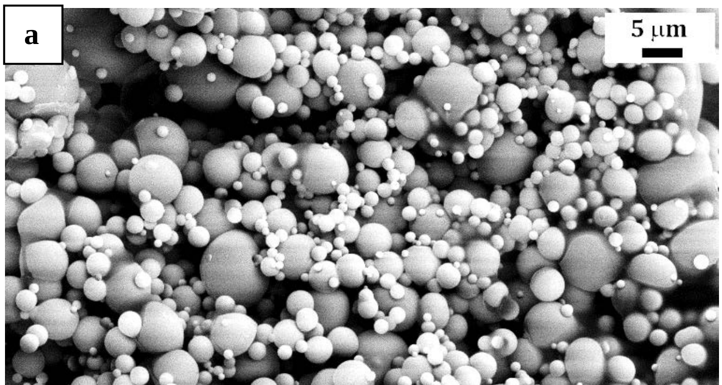

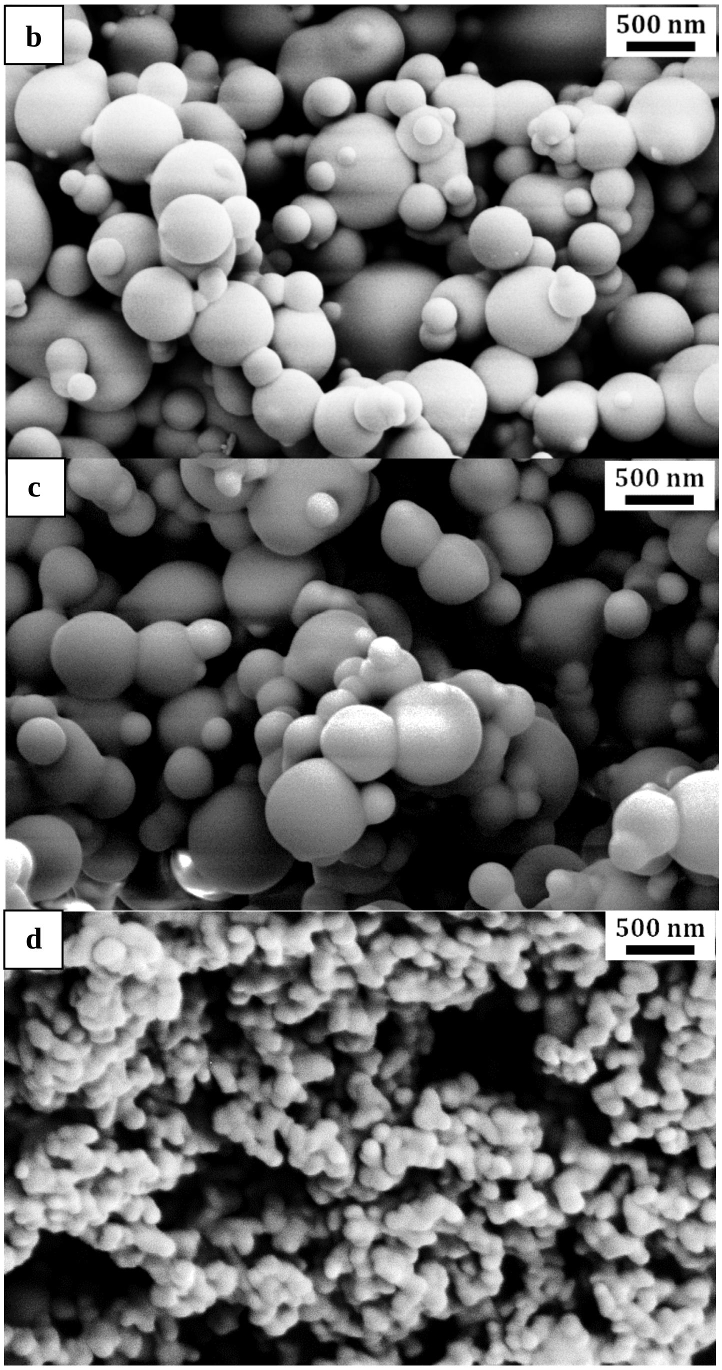

Figure IV. 12 *FESEM images of PVP precipitated at 313 K, 10 MPa, 1% wt from different AC/EtOH mixtures percentages: (a) 0/100 (w/w); (b) 30/70 (w/w); (c) 50/50 (w/w); (d) 70/30 (w/w).*

The contribution of Acetone in the reduction of particles mean size is also evident from the particle size distributions (PSDs) reported in Figure IV.13.

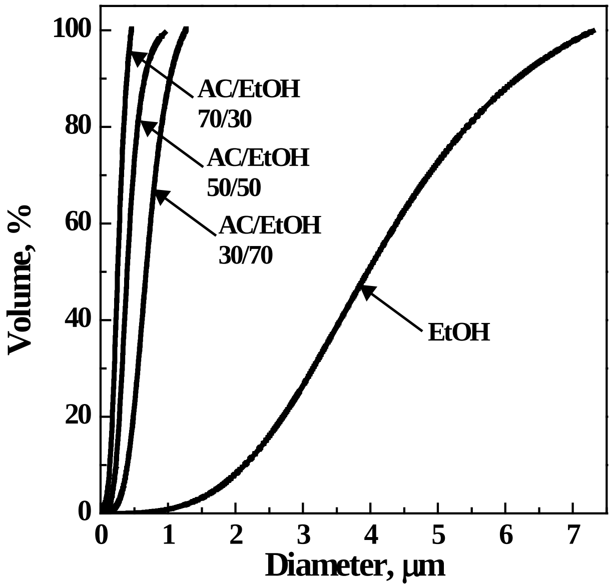

Figure IV. 13 *Volumetric particle size distributions of PVP precipitated at 313 K, 10 MPa, 1% wt from pure EtOH and from different AC/EtOH mixtures percentages.*

When DMSO and AC/DMSO mixtures were used (# 5-8 in Table IV.1), we also observed that acetone acted as a morphology modifier, leading to the production of nanoparticles; again, increasing acetone content in the mixture, the mean size of PVP particles decreased.

In the case of PVP precipitated from NMP and from AC/NMP mixtures, the same proportions of the two solvents were used (# 9-12 in Table IV.1), as in the previous set of experiments. The obtained results followed the same trend of the particles obtained from the mixtures AC/EtOH and AC/DMSO. Particle mean diameter decreased and PSDs sharpened, increasing the percentage of AC in the solvent mixture. A comparison of FESEM images and PSDs of particles obtained from pure NMP and from the mixture AC/NMP 50/50 is reported in Figures IV.14a-IV.14c.

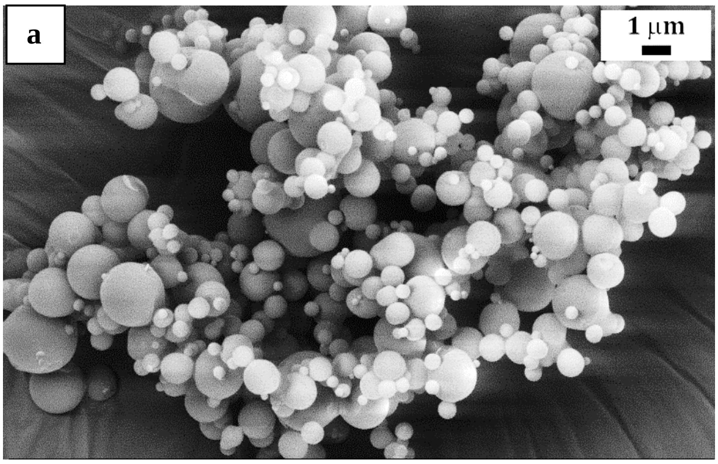
a
1 μm

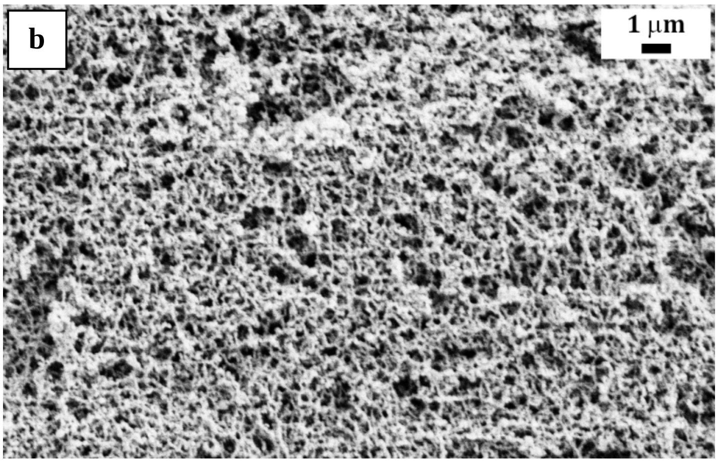
b
1 μm

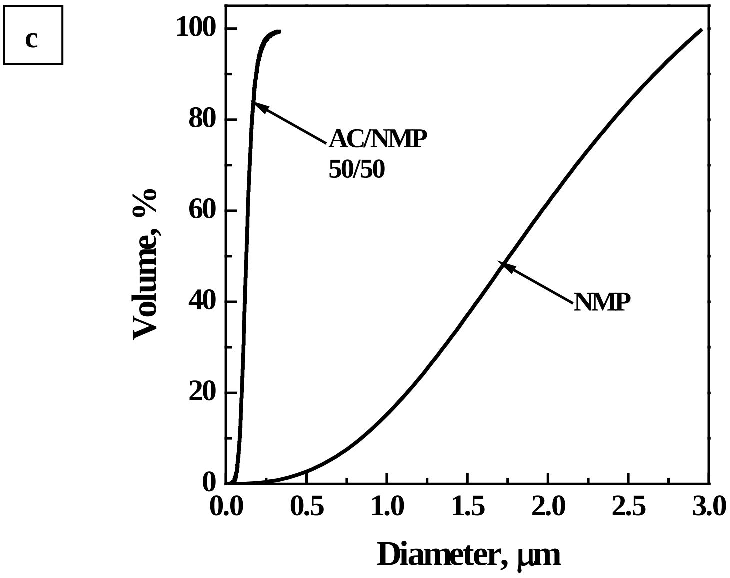

Figure IV. 14 *PVP precipitated at 313 K, 10 MPa, 1% wt. (a-b) FESEM images from pure NMP (a) and AC/NMP 50/50 (b); (c) volumetric particle size distributions.*

For all the performed experiments, the yield of the process was about 90 %.

Summarizing the results, these experiments showed that the use of proper solvent mixtures is effective in the production of nanoparticles of PVP that have never before been obtained by SAS, using pure solvents.

In particular, ethanol and acetone show a similar behavior from the point of view of mixing regimes. Therefore, the decrease of PVP mean particle size and the shrinkage of the particle size distribution is in agreement with the "poor solvent"-"good solvent" interpretation (Dukhin et al., 2003). Adding acetone, that is a "poor solvent" with respect to PVP, the polymer tends to reject acetone molecules, precipitating in a more compact conformation; therefore, particles with a smaller mean particle size were obtained.

In the case of the AC/DMSO and AC/NMP mixtures, the addition of acetone has a double-effect: it is a "poor solvent" with respect to PVP and it is a "narrow transition solvent" from two-phase to one-phase mixing, if compared to DMSO and NMP. Therefore, adding acetone to DMSO and NMP produced a more distinct effect. As indicated in Table IV.1, in these cases, smaller nanoparticles, compared to the ones obtained for PVP precipitated from the AC/EtOH mixture, were produced. This more distinct effect can be explained also considering that PVP solubility in DMSO and NMP (and, consequently, in DMSO/AC and NMP/AC mixtures) is higher with respect to PVP solubility in EtOH and EtOH/AC mixtures. Therefore, when precipitated from EtOH/AC mixtures, PVP nucleation early occurs, because the supersaturation is earlier reached with respect to DMSO/AC and NMP/AC mixtures; therefore, growth phenomenon is favored and higher mean diameters are obtained.

Analyses

Differential scanning calorimetry (DSC) thermograms of untreated and SAS processed PVP samples are shown in Figure IV.15. The DSC diagrams show a broad endothermic peak ranging from 323 to 403 K for all the samples, which indicates the loss of water due to the hygroscopic nature of PVP. This analysis indicates that the SAS process did not alter the product structure.

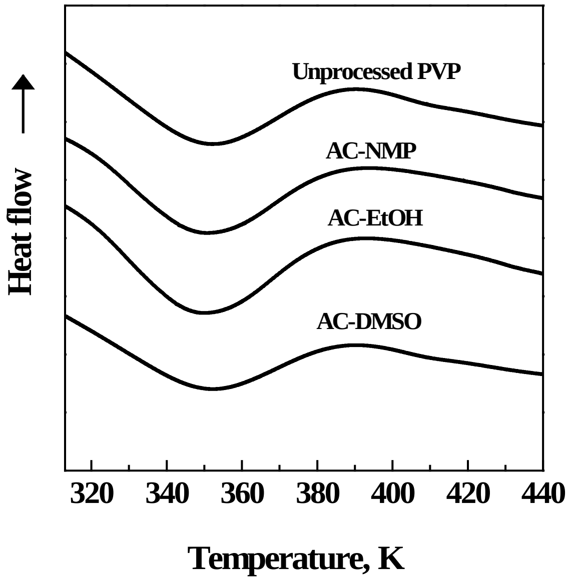

Figure IV. 15 *Differential scanning calorimetry thermograms for unprocessed and SAS processed PVP using the different mixtures.*

X-ray diffraction (XRD) analyses of untreated and SAS processed PVP samples were carried out to evaluate the presence of possible crystalline modification as a consequence of the processing. XRD patterns are reported in Figure IV.16; they show very broad peaks, suggesting that no changes occurred in the amorphous structure of the polymer.

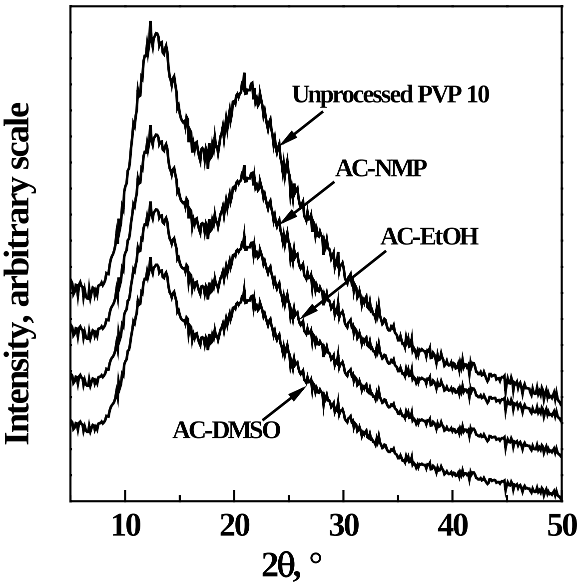

Figure IV. 16 *XRD analysis of unprocessed and SAS processed PVP using the different mixtures.*

Solvent residue was analyzed to verify that it was lower than the Food and Drug Administration (FDA) limit, that, according to the USP 467 for the residual solvents, is equal to 530 for NMP (belonging to class 2), and to 5000 ppm for AC, DMSO and EtOH (belonging to class 3). These analyses revealed that the solvent residue was around 1300 ppm in the case of AC, 2000 ppm in the case of EtOH, 3000 ppm in the case of DMSO and 100 in the case of NMP, therefore, it is, in any case, below the allowed limits.

IV.2.2 SAS precipitation experiments on CA

The aim of this part of the thesis was to verify if solvent mixtures of DMSO/AC can produce microparticles of a model compound, cellulose acetate (CA), thus extending the versatility of SAS in terms of morphologies produced to other solutes. This polymer, when SAS processed using acetone, never produced microparticles (De Marco and Reverchon, 2011b).

SAS experiments were performed at pressures ranging between 85 and 15.0 MPa, concentrations between 20 and 60 mg of CA per mL of liquid solvent, temperature of 313 K, and a nozzle diameter for the liquid solution of 100 μm. The liquid solution flow rate was fixed at 1 mL/min, the ratio between CO_2 flow rate and liquid flow rate (R) was set equal to 30 on a mass basis and the CO_2 molar fraction was equal to 0.98. Table IV.2 reports a list of the experiments performed, indicating all the operating conditions (mixture percentages are expressed as volume/volume), the morphology obtained, the mean diameter and the standard deviation of the particles.

Table IV.2 *SAS experiments performed on CA at 313 K (NP: nanoparticles; MP: microparticles).*

#	**Solvent**	**C, mg/mL**	**P, MPa**	**Morph**	**m.d., µm**	**s.d., µm**
1	AC	20	9.0	NP	0.095	0.024
2	DMSO			-	-	-
3	DMSO/AC 25/75			NP	0.184	0.054
4	DMSO/AC 50/50			MP	0.233	0.050
5	DMSO/AC 75/25			MP	-	-
6	AC	40	9.0	NP	0.170	0.110
7	DMSO/AC 25/75			MP	0.353	0.166
8	DMSO/AC 50/50			MP	0.405	0.167
9	DMSO/AC 75/25			MP	-	-
10	AC	60	9.0	NP	0.210	0.059
11	DMSO/AC 25/75			MP	0.512	0.444
12	DMSO/AC 50/50			MP	0.672	0.059
13	DMSO/AC 75/25			MP	-	-
14	AC	40	8.5	NP	0.206	0.093
15	DMSO/AC 25/75			MP	0.403	0.160
16	DMSO/AC 50/50			MP	0.424	0.155
17	DMSO/AC 75/25			MP	-	-
18	AC	40	10.0	NP	0.099	0.029
19	DMSO/AC 25/75			NP-MP	0.198	0.078
20	DMSO/AC 50/50			MP	0.300	0.188
21				MP	-	-
22	DMSO/AC 75/25		12.0	NP-MP	0.235	0.091
23			15.0	NP-MP	0.218	0.089

Effect of solvent mixture at different liquid concentration

The effect of the different percentages of DMSO/AC in the solvent mixture and at different liquid solution concentrations was evaluated at a pressure of 9.0 MPa.

Experiments at 20 mg/mL

Considering that, in correspondence of this concentration, cellulose acetate is also soluble in DMSO, we performed this set of experiments for AC, DMSO and at all the mixture ratios; i.e., DMSO/AC 75/25, 50/50 and 25/75 (v/v).

Nanoparticles with a narrow size distribution were precipitated from pure acetone on the bottom of the chamber (#1 in Table IV.2). In correspondence of the nozzle nanostructured filaments were recovered; this result confirmed results previously proposed in literature (De Marco and Reverchon, 2011b) for cellulose acetate precipitated from acetone. SAS experiment performed using DMSO as the liquid solvent (# 2 in Table IV.2), produced micrometric particles characterized by a strong coalescence; due to this phenomenon, it was not possible to obtain a reliable measure of the mean diameter and distributions of these particles.

The use of mixtures AC/DMSO (#5 in Table IV.2) produced, instead, intermediate results in terms of morphology. Indeed, increasing the content of DMSO in the processed solution, the mean diameter of the particles increased and microparticles were obtained from the mixtures formed by DMSO/AC 50/50 and 75/25 (v/v). However, the particles obtained from the latter mixture were coalescing and cannot be characterized in terms of dimensions. Coalescence is due to the fact that a quantity of DMSO contained in the mixture was retained by microparticles, inducing the formation of solid bridges.

Experiments at 40 mg/mL

At a concentration of the liquid solution of 40 mg/mL (–9 in Table V.2), CA is no soluble in pure DMSO (the solubility of CA in DMSO is, indeed, equal to 20 mg/mL), but it resulted soluble in correspondence of all the mixture ratios between the solvents tested. From the point of view of the powder recovered on the frit, in the case of acetone only, CA precipitated in form of nanoparticles; whereas, using the DMSO/AC mixtures, it precipitated in form of microparticles, that, as in the case of the experiments performed at 20 mg/mL, were strongly coalescing using the mixture DMSO/AC 75/25 (v/v).

Experiments at 60 mg/mL

A further increase of the liquid solution concentration up to 60 mg/mL (#13 in Table IV.2) confirmed the previous results: particle mean diameter increased; but, an higher number of nanostructured filaments was recovered inside the precipitator, in correspondence of the injector and inside the chamber for acetone.

To visualize the effect of the solvent mixture percentage on the obtained morphology and to visualize the coalescence between particles, in Figure IV.17, FESEM images of the CA particles precipitated from the different mixtures DMSO/AC at 60 mg/mL of liquid solution concentration are reported. FESEM image in Figure IV.17c is particularly interesting, since solid bridges among CA particles are clearly visible.

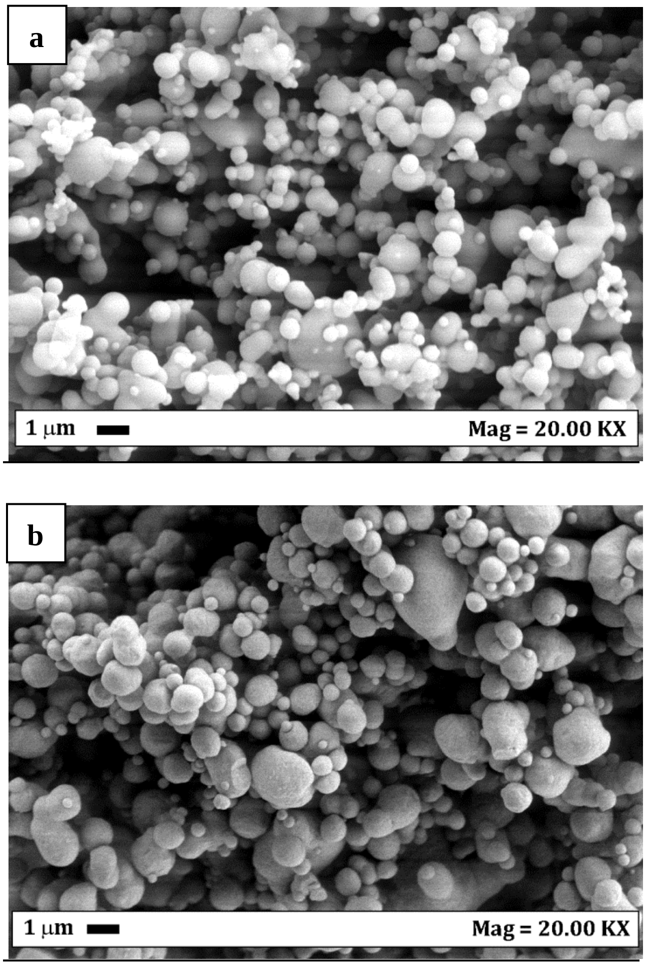

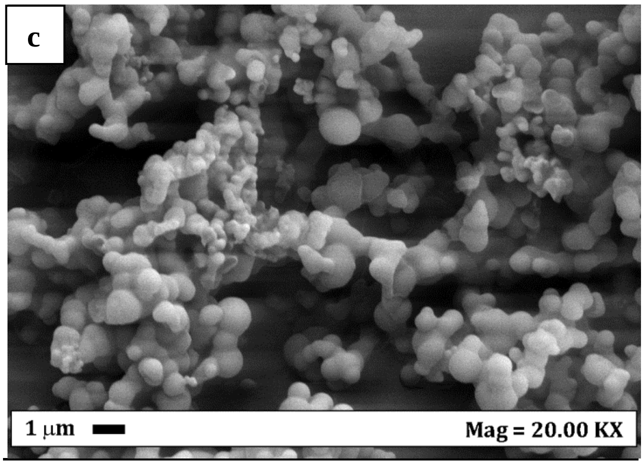

Figure IV.17 *FESEM images of cellulose acetate precipitated at 9.0 MPa, 40°C, 60 mg/mL at different DMSO/Acetone mixtures percentages; (a) 25/75 (v/v); (b) 50/50 (v/v); (c)75/25 (v/v).*

The effect of the liquid solution concentration and of the solvent mixture percentage is shown in Figure IV.17, where the volumetric particle size distribution of the powders obtained from pure AC and from the mixtures DMSO/AC 25/75 and 50/50 (v/v) at 9.0 MPa, 313 K and at different liquid solution concentration, are reported.

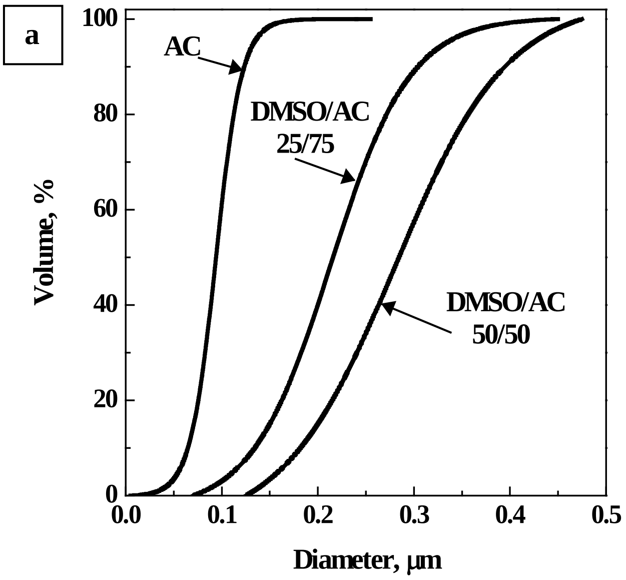

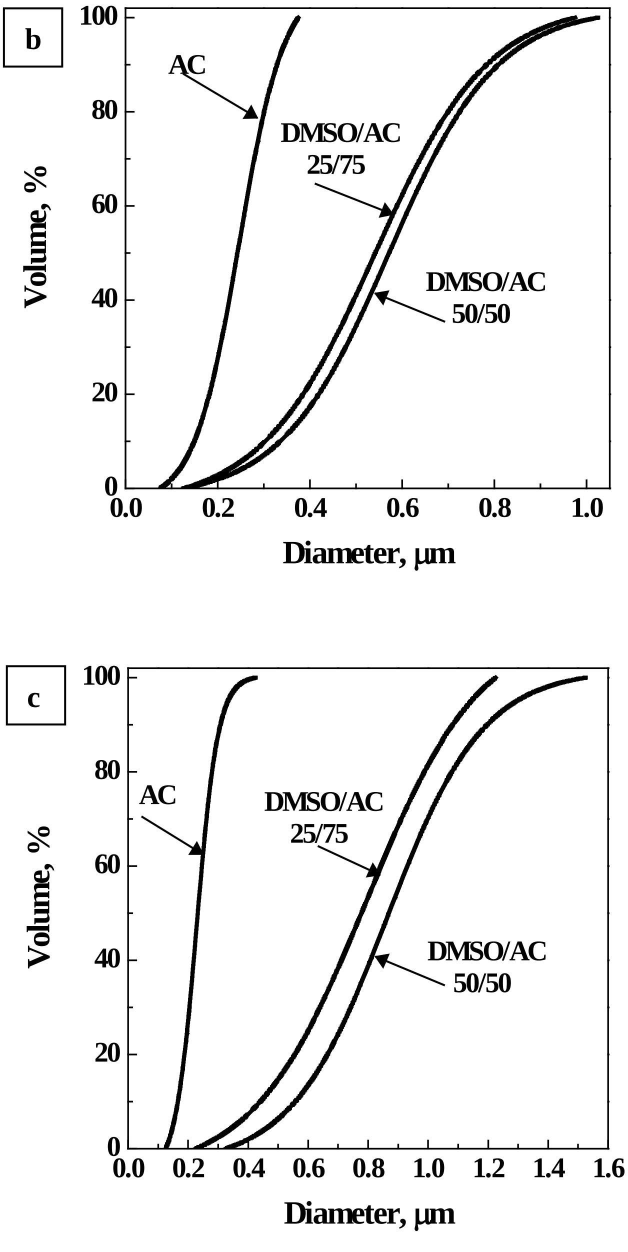

Figure IV.18 *Volumetric particle size distributions of cellulose acetate precipitated at 9.0 MPa, 313 K and at different concentrations for different mixtures; (a) c = 20 mg/mL;(b) c = 40 mg/mL; (c) c = 60 mg/mL.*

From Figs. IV.17 and IV.18, it is possible to observe that not only the mean diameter of the particles increases, but, also the particle size distribution enlarges: increasing the amount of DMSO in the liquid mixture; increasing the concentration of the liquid solution (in the case of pure AC and for both the mixtures DMSO/AC).

Moreover, it is possible to observe that the distributions obtained for the two mixtures DMSO/AC 25/75 and 50/50 (v/v) are very similar, except for the experiments performed at the lower concentration.

Two main considerations may be developed observing these results:

- in the case of the mixture DMSO/AC 75/25 (v/v), the recovered powders are always characterized by a strong coalescence between the particles; indeed, in correspondence of this solvent mixture, residual quantities of this solvent are still present;
- in correspondence of the other two solvent mixtures; i.e., DMSO/AC 50/50 and 27/75 (v/v) and especially at 40 and 60 mg/mL, non-coalescing microparticles, that were the aim of this work, were successfully precipitated.

To better evaluate the modification of the precipitated morphology due to the addition of DMSO, in presence of a solute, the set of experiments that follows was performed at different pressures.

Effect of pressure

The concentration of the liquid solution was fixed at 40 mg/mL and the effect of pressure was studied in the range 8.5-15.0 MPa, keeping unchanged all the other operating conditions.

At 8.5 MPa, the tested solvent mixtures showed two-phase mixing behavior, in absence of solute, when tested using elastic light scattering technique (De Marco et al., 2012); using CA, microparticles with an higher mean diameter with respect to the ones precipitated at 9.0 MPa were obtained. At 10.0 MPa, corresponding to completely developed supercritical conditions for all the solvent mixtures (De Marco et al., 2012) was, then, evaluated the effect of the presence of the solute. In correspondence of all the mixture ratios; i.e., pure acetone, DMSO/AC 25/75 and DMSO/AC 50/50 (v/v), it was observed that, increasing the pressure, the mean particle size decreased and the particle size distribution shrank. This trend can be qualitatively observed in Figure IV.19, where FESEM images, taken at the same magnification, of the powders obtained at different pressures, in the case of the mixture DMSO/AC 25/75 (v/v), are reported.

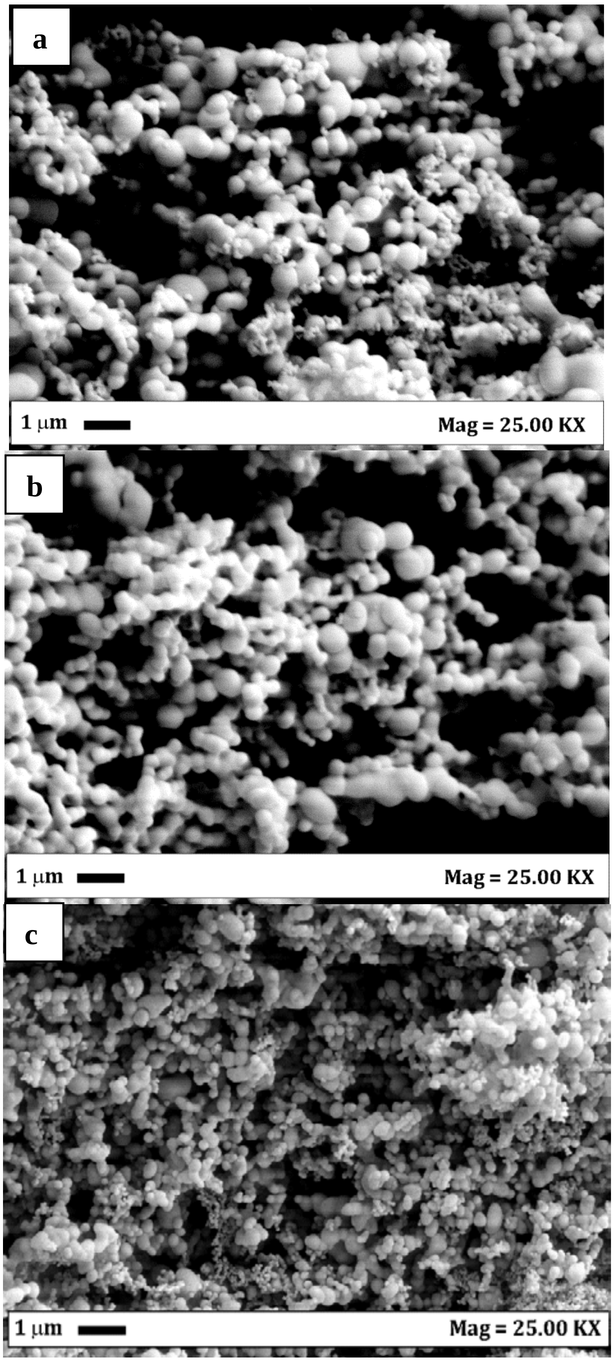

Figure IV. 19 *FESEM images of cellulose acetate precipitated at 313 K, 40 mg/mL, DMSO/Acetone 25/75 (v/v) at different pressures; (a) P = 8.5 MPa; (b) P = 9.0 MPa; (c) P = 10.0 MPa.*

For the mixture DMSO/AC 25/75 (v/v), that, in absence of the solute, showed a complete one-phase mixing starting from 9.0 MPa we observed, at 10.0 MPa, the coexistence of microparticles and nanoparticles; therefore, for this mixture, presumably the transition from two-phase to one-phase mixing, precipitating a CA solution with a concentration of 40 mg/mL, was not still complete. For the higher pressure SAS experiments, it was chosen the mixture DMSO/AC 50/50 (v/v).

Experiments at 12.0 and 15.0 MPa were also carried out. In Figure IV.20, particle size distributions of the CA particles precipitated from the mixture with 50% of DMSO are reported.

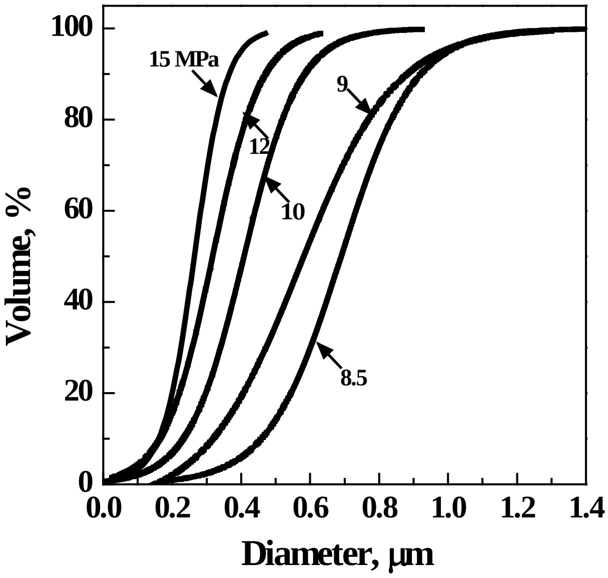

Figure IV.20 *Volumetric particle size distributions of cellulose acetate precipitated at 313 K and 40 mg/mL at different pressures.*

Increasing the pressure, the mean diameter decreased; moreover, it is possible to observe that, while, at 10.0 MPa, nanoparticles precipitated together with microparticles from the mixture DMSO/AC 25/75 (v/v), at 12.0 MPa, nanoparticles and microparticles precipitated together in the case of the mixture DMSO/AC 50/50 (v/v). This experimental evidence underlines the fact that probably a transition from a two-phase mixing flow to a single-phase mixing is occurring at pressures higher than in absence of solute.

Analyses

Differential scanning calorimetry (DCS) thermograms of untreated and SAS processed CA samples are shown in Figure IV.21a. A broad endothermic event between room temperature and 373 K is present in all DSC traces. It can be attributed to water desorption from polysaccharide structure. Untreated CA and all the samples obtained from AC, DMSO and their mixtures show an endothermic melting peak at 503 K. This analysis indicated that the SAS process did not alter the product structure.

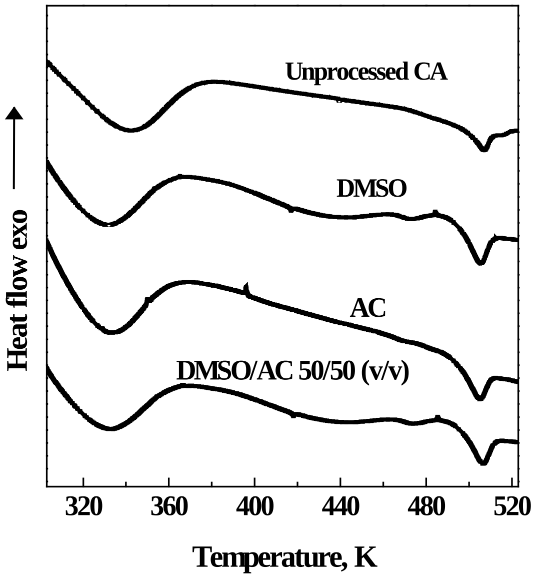

Figure IV.21 *Differential scanning calorimetry thermograms for unprocessed and SAS processed CA, Exo indicates exothermic flow.*

X-ray diffraction patterns (XRD) analyses for untreated and SAS processed CA samples are shown in Figure IV.22. This analysis confirm that no changes occurred in the amorphous structure of the materials as a consequence of the SAS processing.

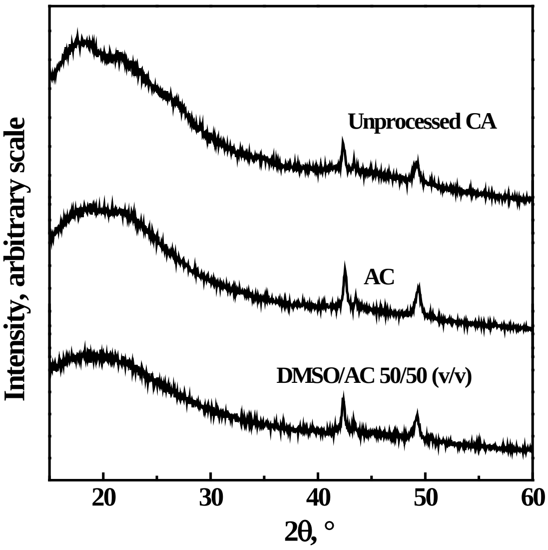

Figure IV.22 *XRD analysis of unprocessed and SAS processed CA.*

IV.2.3 Conclusions

The results obtained in this part of the thesis confirmed that solvent mixtures, formed by a sharp two-phase/one-phase mixing transition solvent (like acetone) plus a broad two-phase/one-phase mixing transition solvent (like DMSO), not only show intermediate behaviors between the two solvents during SAS processing, but allow the production of the corresponding morphology, when a solute is present.

Chapter V
Coprecipitation in SAS process

V.1 Background

Coprecipitated microparticles play an important role in various industrial fields, such as agriculture, biomedicals, pharmaceuticals, foods and cosmetics. Indeed, they can be used to protect the encapsulated material against oxidation and deactivation, to achieve a controlled delivery of the active ingredients and to mask organoleptic properties like color, taste, and odor of the active compounds (Vladisavljević, 2012).

Traditional techniques used to produce coprecipitates include: spray-drying (Vehring, 2008), emulsification/solvent evaporation (O'Donnell and McGinity, 1997), centrifugal extrusion (Oxley, 2012), freeze drying (Heidebach et al., 2010), and coacervation (Nihant et al., 1995). These techniques suffer some limitations, such as relatively large particle size, wide particle size distribution, possible degradation of the product and difficulties in the complete elimination of organic solvents used in the process (Wang et al., 2013).

Supercritical fluids (SCFs) based techniques have been proposed as an alternative to conventional processes, thanks to their specific characteristics, mainly solvent power and liquid-like densities with gas-like transport properties that can be tuned varying pressure and temperature. Among supercritical assisted micronization techniques, Supercritical Antisolvent (SAS) precipitation has been successfully used to obtain microparticles and nanoparticles of several kinds of compounds, such as pharmaceuticals, superconductors, coloring matters, polymers and biopolymers (Chávez et al., 2003b, De Marco et al., 2013, Caputo et al., 2012, Marra et al., 2012, Prosapio et al., 2014, E. Reverchon, 2011, Rossmann et al., 2012, Sarkari et al., 2000, Wang et al., 2006). However, until now, only few SAS works have been focused on the production of coprecipitates due to the difficulty in producing composite microparticles using this technique. Indeed, some authors attempted polymer/drug coprecipitation using SAS; but, the obtained particles were generally irregular and coalescing (Montes et al., 2011), with broad particle size distributions (Patomchaiviwat et al., 2008, Uzun et al., 2011), low drug entrapment efficiency (Chen et al., 2006, Wang et al., 2013) and, in most of the cases, the demonstration of the effective coprecipitation was at least questionable (Elvassore et al., 2001, Kalogiannis et al., 2006, Li et al., 2012, Nerome et al., 2013). Indeed, the authors had difficulties in demonstrating that a coprecipitate was formed and that drug properties were improved. A convincing explanation of the coprecipitation mechanism is also missing.

In order to overcome these limitations, the aims of this work are to test the applicability of SAS process to produce microcomposite coprecipitates and to understand the possible mechanisms of SAS coprecipitation, its applicability and limits.

V.2 Precipitation experiments

Materials

Polyvinylpyrrolidone (PVP, average molecular weights of 10 kg/mol), folic acid (FA, purity ≥ 97%), β-carotene (BC, purity ≥ 93 %), dexamethasone (DMS, purity ≥ 98 %), prednisolone (PDN, purity ≥ 99 %), budesonide (BDS, purity ≥ 99 %), ethanol (EtOH, purity 99.5%) and dimethylsulfoxide (DMSO, purity 99.5%) were supplied by Sigma–Aldrich (Italy). CO_2 (purity 99 %) was purchased from SON (Italy). All materials were used as received.

V.2.1 PVP/Folic acid

Folic acid (Thiering et al.) or folates, belonging to vitamin B family, are essential for the proper working of a variety of human physiological processes, such as biosynthesis of nucleotides, cell division, gene expression; moreover, FA is important in the prevention of neural tube defects in infants, vascular diseases and megaloblastic anemia (Prasertmanakit et al., 2009). However, Folic acid is not produced by human body; therefore, it must be necessarily taken with the diet; but, natural folates in foods undergo degradation reactions when they are exposed to light, moisture, acid or alkaline medium, oxygen and high temperatures (Lopera et al., 2009). A possible solution, to improve folates stability and their bioactivity, is represented by their coprecipitation with a biodegradable polymeric carrier, that can protect the vitamin from degradation (Pérez-Masiá et al., 2015). Moreover, since FA shows a low water solubility (0.0016 mg/mL), it is necessary to use a hydrophilic polymer to improve its bioavailability.

Polyvinylpyrrolidone (PVP) is a water soluble synthetic polymer, widely used as carrier in controlled release systems (Ledet et al., 2015a) or to enhance the dissolution rate of poorly water soluble drugs (Oth and Moës, 1985). Particularly, its ability to retard crystal growth makes it suitable for the coprecipitation with crystalline substances (Ledet et al., 2015a). Since it possesses the GRAS (Generally Regarded As Safe) status and it is included in the FDA (Food and Drug Administration) list, it can be used in pharmaceutical, biomedical and food applications.

Specifically speaking of FA processing, Prasertmanakit et al (Prasertmanakit et al., 2009) proposed the production of microcapsules of folic acid and ethyl cellulose using the emulsion solvent evaporation technique; they obtained very large particles with low encapsulation efficiency and the release profiles did not show a substantial improvement of FA dissolution rate. Lopera et al (Lopera et al., 2009) used spray drying process for the obtaining of microparticles of FA+arabic gum+maltodextrin; the results showed the production of irregular particles with broad particle size distribution. Pérez-Masiá et al (Pérez-Masiá et al., 2015) proposed the encapsulation of FA through electrospraying and nanospray drying techniques; the authors used both whey protein and starch as carrier but they did not report the dissolution tests to demonstrate the increase of FA bioavailability.

In order to overcome the limitations of traditional techniques and SAS coprecipitation works until now, the aim of this part of the Ph.D. is to test the applicability of SAS process to produce microcomposite coprecipitates applying it to a compound of nutraceutical/pharmaceutical interest like FA and using PVP as a hydrophilic polymer trying to take advantage of its specific crystallization blockage characteristics.

The general scope of this work is to understand SAS coprecipitation applicability, limitations and the possible precipitation mechanisms.

Experimental results

All SAS experiments were carried out using a CO_2 flow rate of 10000 mL/min, a solution flow rate of 1 mL/min, an injector of 100 µm internal diameter and DMSO as the liquid solvent. The effect of PVP/AF w/w ratio, operating pressure, temperature and total concentration was investigated. In Table V.1, a list of the most relevant experiments is reported, with the indication of the obtained morphology, mean diameter (m.d.) and standard deviation (s.d.).

Table V.1 *SAS experiments performed on PVP/FA mixtures (MP: microparticles, SMP: sub-microparticles; NP: nanoparticles).*

#	**P MPa**	**PVP/FA w/w**	**T K**	**C_{tot} mg/mL**	**Morph.**	**D µm**	**s.d. µm**
1	15	0:1	313	20	-	-	-
2		1:0			MP	3.80	2.41
3		1:1		40	-	-	-
4		2:1			NP	0.05	0.01
5		5:1			NP	0.18	0.05
6		10:1			NP	0.27	0.07
7		20:1			SMP	0.65	0.15
8		5:1			SMP	0.65	0.18
9	9	10:1			MP	2.63	0.76
10		20:1			MP	3.81	1.11
11	10	10:1			MP	2.35	0.95
12	11				MP	1.18	0.27
13	12				MP	0.81	0.25
14	13				SMP	0.31	0.05
15			308		SMP	0.29	0.06
16	9		313	20	MP	1.15	0.31
17				10	-	-	-

The first experiment was performed processing FA alone at 15 MPa, 313 K and at a concentration of 20 mg/mL (#1 in Table V.1). Using these operating conditions, FA precipitated in form of large and irregular material, as it is possible to observe from the FESEM image reported in Figure V.1.

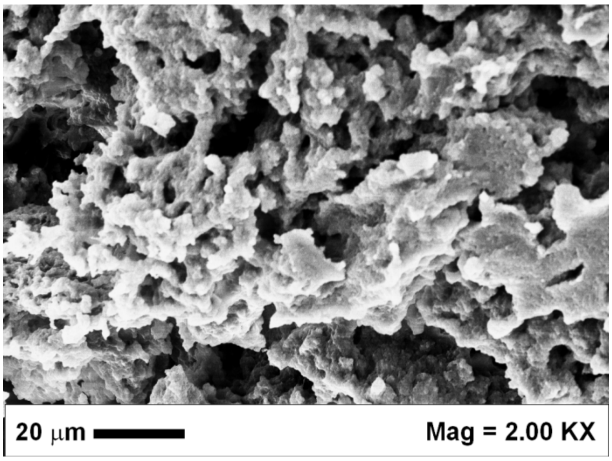

Figure V. 1 *FESEM image of FA precipitated from DMSO at 15 MPa, 313 K, 20 mg/mL.*

Then, PVP alone was SAS processed, using the same solvent and the same operating conditions of the test performed on FA, to confirm results already observed in the literature (De Marco et al., 2015, Rossmann et al., 2014). As it is possible to observe from the FESEM image reported in Figure V.2, PVP precipitated in form of spherical separated microparticles with a mean diameter of 3.8 µm (in Table VI.1).

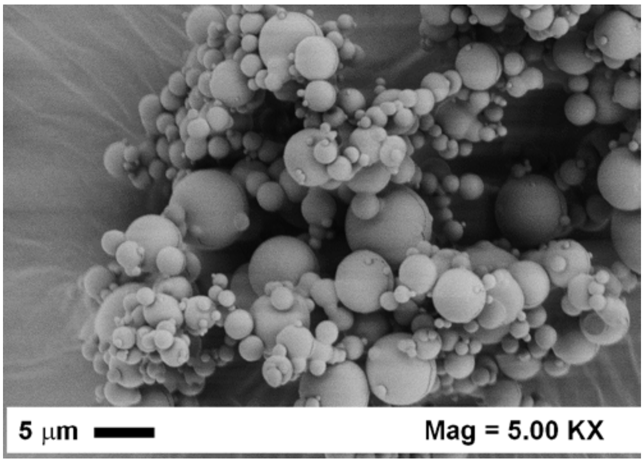

Figure V. 2 *FESEM image of PVP precipitated from DMSO at 15 MPa, 313 K, 20 mg/mL.*

This result confirms the ones obtained by Rossmann et al. (Rossmann et al., 2014) and by De Marco et al. (De Marco et al., 2015); they observed that SAS processed PVP precipitated from ethanol (Rossmann et al., 2014) and from different solvents, including DMSO, in form of microparticles at operating pressures up to 30 MPa. The result is unusual since, as a rule, SAS produces microparticles only near the mixture critical point (MCP) pressure of the adopted system CO_2-solvent. This phenomenon is probably due to the fact that, in this case, the presence of PVP strongly enlarges the range of pressures in which the transition from two-phase to one-phase mixing takes place (E. Reverchon, 2011).

The observation of Figures V.1 and V.2 shows that FA and PVP exhibit completely different morphologies at the same operating conditions and, from a SAS point of view, FA can be considered a very bad candidate for micronization; whereas, PVP is a good candidate for coprecipitates formation. At this point, the challenge of this study is: what will happen when we try to coprecipitate the two compounds? Can PVP particles maintain spherical morphology that is the result of jet break-up and droplets formation and drying (He et al., 2008)? Can PVP force FA to coprecipitate in a regularly distributed system forming a nanocomposite material? To answer to these questions, the other experiments reported in this study were performed varying: (a) the ratio PVP/FA that should describe the interaction of the two compounds in different proportions and at different pressures; (b) the operating temperature and (c) the total concentration of the two solutes in DMSO.

The binary system CO_2/DMSO at 313 K (Andreatta et al., 2007) shows the MCP at approximately 8.5 MPa. Therefore, we decided to investigate the effect of polymer/drug ratio in correspondence of two very different operating conditions: at completely developed supercritical conditions (one phase mixing), i.e., far above the MCP (15.0 MPa) and near the transition from two-phases to one-phase mixing (De Marco et al., 2012) that occurs at 9.0 MPa.

Effect of PVP/FA ratio operating at pressures far above the MCP

The first SAS tests on the system PVP-FA were performed at the same operating conditions chosen for the precipitation of the single compounds (15 MPa and 313 K), fixing the total concentration of the liquid solution at 40 mg/mL and varying the ratio PVP/FA (#7 in Table V.1). Examples of FESEM images of the precipitated powders are shown in Figure V.3.

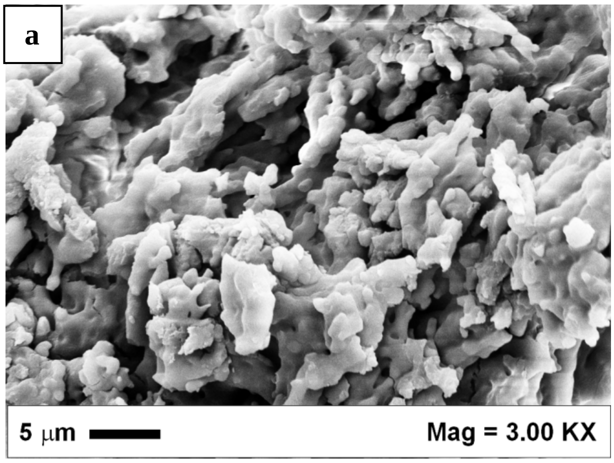

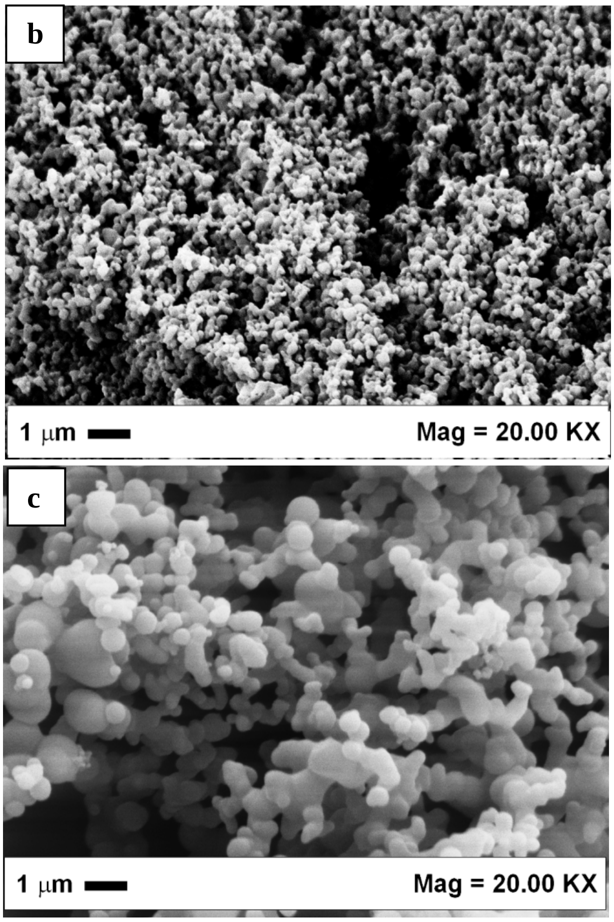

Figure V.3 *FESEM images of PVP–FA particles precipitated from DMSO at 15.0 MPa and 313 K at different polymer/drug ratios: (a) 1/1 w/w, (b) 5/1 w/w, (c) 20/1 w/w.*

When PVP/FA 1/1 w/w was processed, the precipitated material was irregular and coalescing (Figure V.3a). Increasing PVP/FA ratios at 2/1, 5/1 and 10/1 w/w, nanoparticles of increasing mean diameter were produced. In Figure V.3b, an example of these nanoparticles is reported; their mean diameter is 0.05 µm for PVP/FA 2/1 w/w, 0.18 µm for 5/1 w/w and 0.27 µm for 10/1 w/w. At ratio PVP/FA 20/1 w/w, sub-microparticles with a mean diameter of 0.65 µm were obtained (Figure V.3c).

The volumetric cumulative particle size distributions of the powder precipitated at different PVP/FA ratios are reported in Figure V.4; it is possible to observe that, increasing the content of PVP in the processed solution, the mean size of the precipitated particles increased and the particle size distribution (PSD) enlarged.

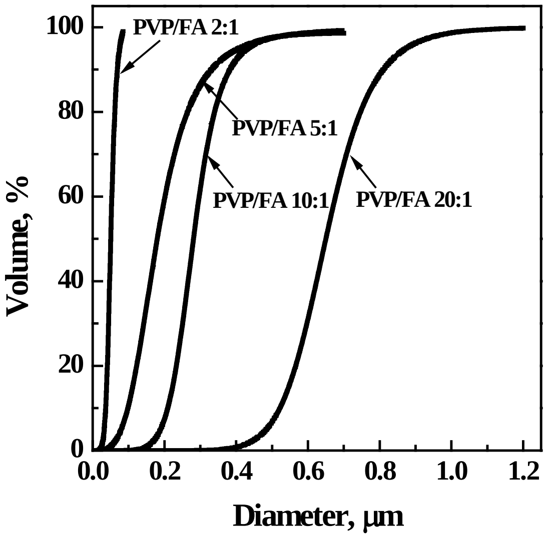

Figure V.4 *Volumetric cumulative PSDs of PVP–FA nano and sub-microparticles precipitated from DMSO at 15.0 MPa and 313 K at different polymer/drug ratios.*

Summarizing this part of results, at a PVP/FA ratio 1/1 w/w, large amorphous particles were obtained, in which evidently the FA contribution prevails in determining the final size and morphology. But, starting from 2/1 w/w ratio, nanoparticles precipitation was observed. This result is interesting, since at these operating conditions neither PVP nor folic acid showed this morphology in the reference tests (#1-2). A possible explanation of these results is that probably FA in the mixture operates as a surface tension reducer and, thus, favors the mechanism of gas-mixing with respect to jet break-up, reducing the time of surface tension vanishing (Lee et al., 1985). It is also interesting to note that using DMSO at 15 MPa, 313 K, nanoparticles have been frequently observed in the literature for several solutes (Torino et al., 2010, Campardelli et al., 2015) , with the exception of PVP (Rossmann et al., 2014).

Effect of PVP/FA ratio operating at pressures near above the MCP

The effect of PVP/FA ratio was also studied at 9 MPa and 313 K; i.e., at operating pressures near above the DMSO/CO_2 MCP (-10 in Table VI.1). At these process conditions, well separated sub-microparticles and microparticles were obtained at all polymer/drug ratios tested (5/1, 10/1, 20/1 w/w), as shown, for example, in FESEM images reported in Figure V.5.

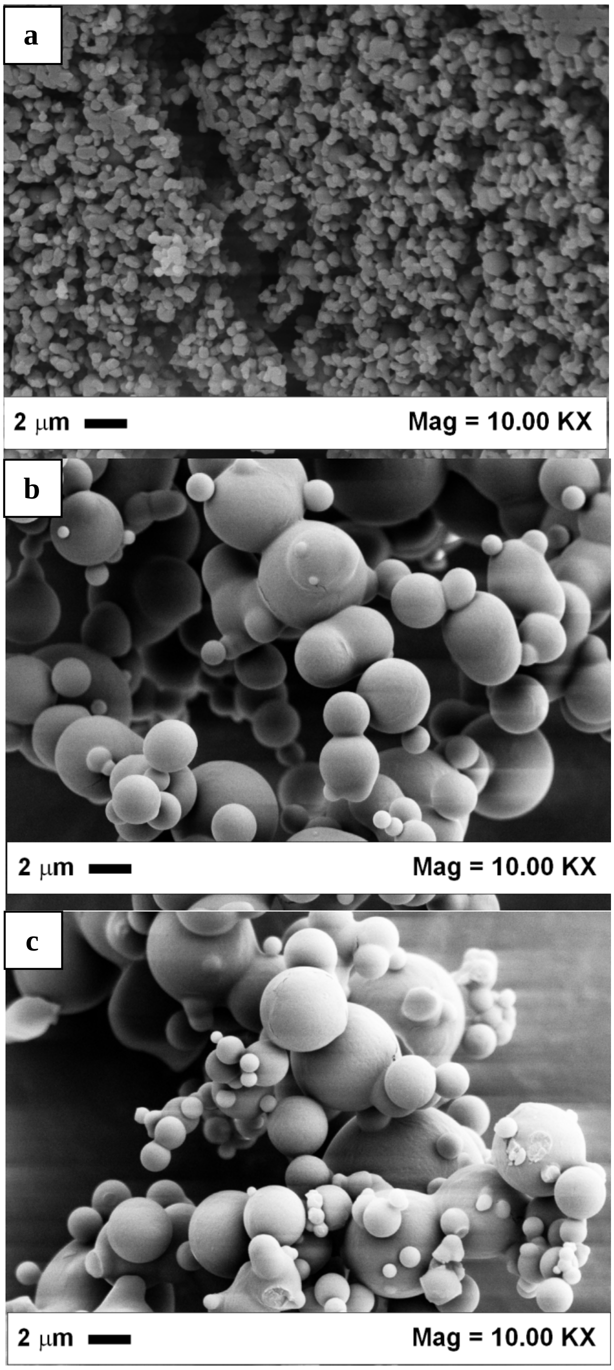

Figure V.5 *FESEM images of PVP–FA particles precipitated from DMSO at 9 MPa and 313 K with different polymer/drug ratio: (a) 5/1 w/w, (b) 10/1 w/w, (c) 20/1 w/w.*

The most interesting result is the one observed starting from the 10/1 w/w PVP/FA ratio. For the first time, in this study, we observed the formation of spherical microparticles similar in morphology to the microparticles precipitated by SAS using PVP alone.

Comparing the volumetric PSDs of the precipitated particles at different PVP/FA ratios, obtained in this set of experiments, it can be observed that, increasing the PVP/FA ratio, the mean size of the particles increased and the PSD enlarged, as shown in Figure V.6. In particular, for PVP/FA 5/1 w/w, sub-microparticles with a mean diameter equal to 0.65 µm were obtained (Figure V.5a); whereas, for PVP/AF 10/1 and 20/1 w/w (Figures V.5b-V.5c), microparticles with mean diameters equal to about 2.6 and 3.8 µm were produced, respectively.

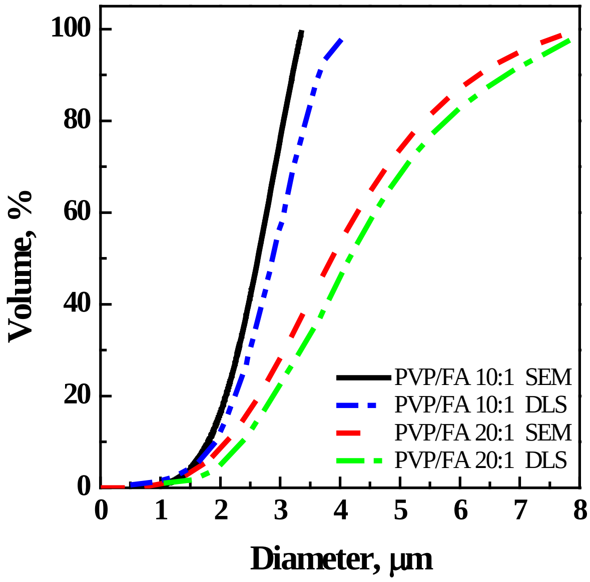

Figure V.6 *Volumetric cumulative PSDs of PVP-FA microparticles precipitated from DMSO at 9 MPa and 313 K at different polymer/drug ratios, using FESEM images analysis and DLS analysis.*

Summarizing, either at 15 or at 9 MPa, an increase of the ratio PVP/AF induced an increase of the mean particle size and an enlargement of the particle size distribution. The differences between the two sets of experiments are related to the obtained morphologies:

- at 15 MPa, the PVP/AF powders are in the nanometric or sub-micrometric range;

- at 9 MPa, the PVP/FA powders are in the sub-micrometric range only for the ratio 5/1 and in the micrometric range in the tests performed at higher PVP/FA ratios.

Effect of the operating pressure and temperature

To obtain a complete screening of the effect of the SAS operating parameters on PVP/FA coprecipitates morphology, particle size and particle size distribution, the ratio PVP/FA was fixed at 10/1 and operating pressure and temperature were varied. Considering that, in terms of pressure, two limit SAS conditions have been already explored (9 and 15 MPa), experiments at 10, 11, 12 and 13 MPa were performed. At these intermediate pressures, microparticles with a mean diameter ranging from about 0.8 to 2.4 µm were obtained between 10 and 12 MPa; whereas, sub-microparticles with a mean diameter of about 0.3 µm were obtained at 13 MPa.

In Figure V.7, a comparison among the volumetric cumulative particle size distributions of the particles obtained, at the same polymer/drug ratio (10/1) and at all tested pressures, is reported. As it is possible to observe, reducing the operating pressure, the mean particle size increased and the PSD enlarged.

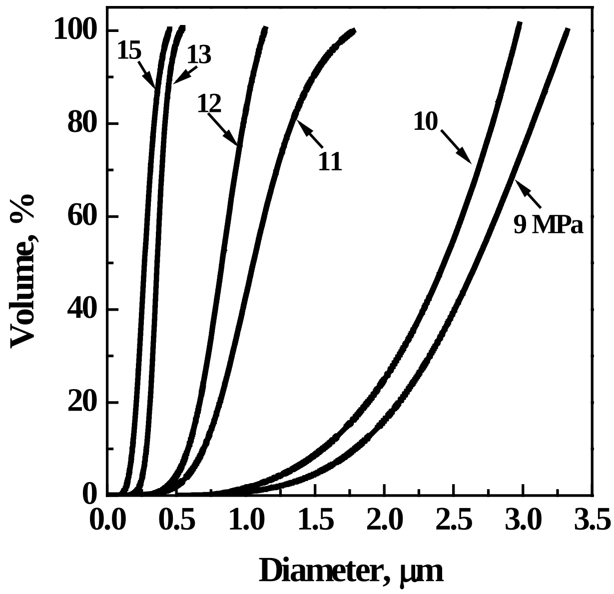

Figure V.7 *Volumetric cumulative PSDs of PVP-FA particles precipitated from DMSO: effect of the operating pressure*

Then, we fixed the operating pressure at 9.0 MPa and the effect of temperature was evaluated, carrying out an experiment at 308 K (#15 in

Table V.1); operating at these conditions, sub-microparticles, instead of microparticles, were produced. The comparison of the particle size distributions of the powders precipitated at 308 and 313 K is reported in Figure V.8. Reducing the operating temperature, the mean size of the particles reduced and particles size distribution shrank.

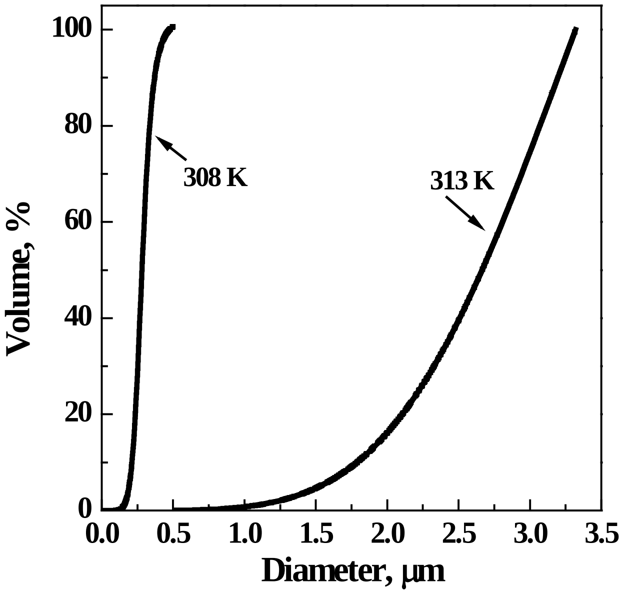

Figure V.8 *Volumetric cumulative PSDs of PVP-FA particles precipitated from DMSO: effect of the operating temperature.*

Effect of concentration

The effect of the total concentration of solutes in the liquid solution was investigated at 9.0 MPa, 313 K and PVP/FA 10/1; the data at 40 mg/mL was already available and additional experiments at 20 and 10 mg/mL were performed (#17 in Table V.1). Using an overall concentration of 20 mg/mL, microparticles were produced, with a mean diameter equal to about 1.2 μm, whereas, at 10 mg/mL, the powder precipitated in form of very coalescing particles that cannot be characterized in terms of dimensions.

Comparing the mean diameter and the PSD of the microparticles obtained at 40 and 20 mg/mL (experiments #9 and #16), it can be observed that, reducing the concentration, the mean particle size reduced and the PSD became narrower.

Characterization of precipitates

X-ray diffraction (XRD) analyses were carried out on untreated FA, SAS processed FA, untreated PVP, SAS processed PVP, physical mixtures PVP+FA and SAS processed PVP+FA at different ratios and different pressures to evaluate the crystallization behavior of the different samples. These analyses revealed that the unprocessed vitamin and the physical mixture show the typical crystalline structure of FA, whereas all FA processed samples showed an amorphous structure (examples of traces of this analysis are reported in Figure V.9).

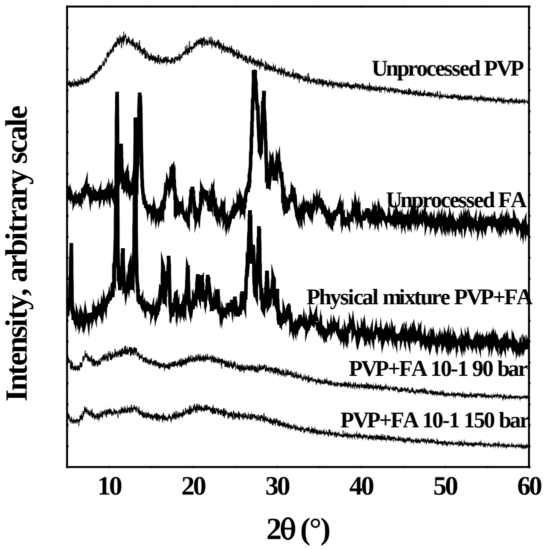

Figure V.9 *XRD analysis of unprocessed and processed powders*

HPLC analyses, reported in Figure V.10, were performed to study the degradation of FA after SAS processing. In correspondence of a wavelength of 362 nm, FA showed a peak at a retention time equal to 18 min. Comparing the processed FA area under the peak with the unprocessed FA area under the peak , we found a value that can be correlated to the integrity of the vitamin equal to 88 %. Comparing, then, the coprecipitated particles PVP+FA 10:1 w/w area under the peak with the unprocessed physical mixture PVP+FA area under the peak, we found a value that can be correlated to the integrity of the vitamin equal to 95 %. These results suggest that, not only SAS process has a not relevant influence on vitamin integrity, but also that the presence of PVP in the coprecipitates protects folic acid from degradation.

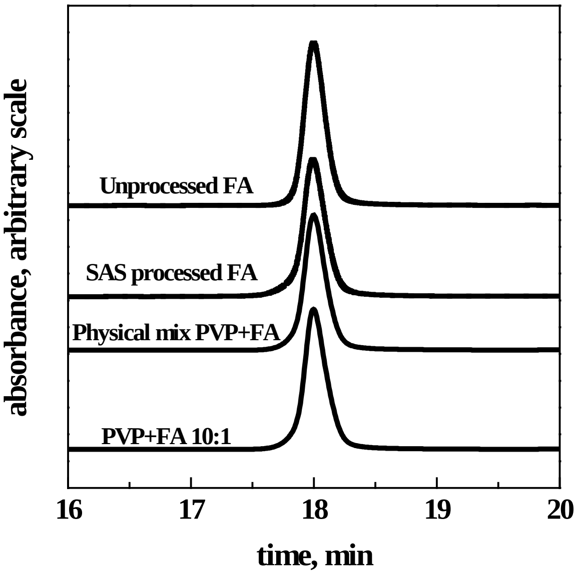

Figure V.10 *HPLC traces of unprocessed and processed powders.*

Drug entrapment efficiency analyses revealed that the powders obtained at 15.0 MPa (nanoparticles) show a drug content with respect to the initial value reduction equal to 66 %, whereas the powders obtained at 9.0 MPa (microparticles) show a drug content between 95 and 99 % with respect to the initial values. These results confirm the presence of both solutes in the samples. However, these results are not sufficient to demonstrate that PVP and FA are coprecipitated. Therefore, dissolution tests in PBS were performed to compare the dissolution rate of different samples, because, if the coprecipitation properly occurred, FA has to be present at nanometric dimensions inside PVP microparticles and its dissolution rate should significantly increase.

Therefore, the dissolution rate of each sample was monitored plotting for 80 hours the percentage of dissolved FA as a function of time. The analyses were performed for unprocessed FA, SAS processed FA, for the physical mixture PVP+FA 10/1 w/w and for the samples PVP/FA 10/1 w/w processed at 9.0 and 15.0 MPa, with an overall concentration of 40 mg/mL; these results are shown in Figure V.11.

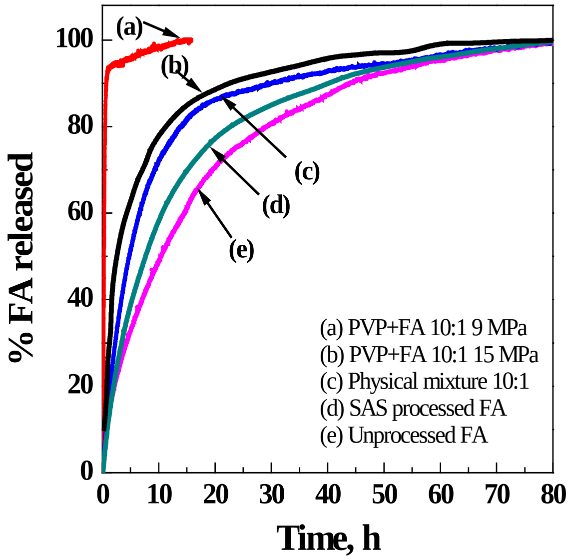

Figure V.11 *Dissolution profiles of FA in PBS at 310 K and pH 7.0.*

Considering as the reference point the dissolution profile of untreated FA, SAS processed FA (alone) shows a slight reduction of the dissolution time, probably connected to the amorphous particles generated during this process. The physical unprocessed mixture PVP/FA 10/1 w/w shows a faster dissolution with respect to reference FA and the same mixture processed at 15.0 MPa, 313 K, in which nanoparticles were produced, exhibits an even shorter dissolution time. However, only the mixture 10/1 w/w processed at 9.0 MPa, 313 K, in which microparticles were formed, shows a radically different behavior, with a dissolution profile in which about 90 % of the drug was released in one hour: the drug dissolution rate is about 45 times faster than single FA, 30 times faster than the physical mixture and 23 times faster than SAS produced nanoparticles. This last result requires a further comment: PVP+FA nanoparticles precipitate is 23 times less efficient than the corresponding microparticles precipitate.

V.2.2 PVP/β-carotene coprecipitates

Nutraceuticals are defined as functional ingredients (antioxidants, vitamins, etc.) that, if taken regularly, can prevent or treat some diseases (DeFelice, 1995).

β-carotene (BC) is a carotenoid, present in sweet potatoes, carrots, spinaches, pumpkins, broccoli, peas, peppers, pink grapefruits, papayas and peaches (Keijer et al., 2005). It is a precursor of Vitamin A and its intake is fundamental to reduce the risk of cardiovascular diseases (Stahl and Sies, 2003), osteoporosis (Chen et al., 2015a) and to prevent cancer of stomach, esophagus, lung, oral cavity, pharynx, pancreas and colon (Chen et al., 2015a, Li et al., 2015b). Carotenoids are not produced by human organism, therefore, they have to be acquired with the diet; however, BC easily undergoes chemical or physical degradation in presence of light, moisture, oxygen and high temperature, during storage (Hosseini et al., 2015). To avoid these adverse effects and to preserve the vitamin nutritional properties, encapsulation systems have been developed. These composite particles are formed by a drug or a vitamin uniformly dispersed in a polymeric matrix or by drug or vitamin particles coated with a polymeric shell. In these systems, the carrier should be a hydrophilic polymer, since BC shows low water solubility and, therefore, a reduced bioavailability. Polyvinylpyrrolidone (PVP) is a water-soluble polymer, broadly used as carrier in pharmaceutical, biomedical and food applications, since it possesses the GRAS (Generally Regarded As Safe) status and is included in the FDA (Food and Drug Administration) list. It has the ability to retard crystal growth (Yang et al., 2015) and to enhance the dissolution rate of poorly water-soluble drugs (Oth and Moës, 1985).

Various conventional processes have been reported for the production of coprecipitates: spray-drying (Vehring, 2008), emulsification/solvent evaporation (O'Donnell and McGinity, 1997), centrifugal extrusion (Oxley, 2012), freeze drying (Heidebach et al., 2010), and coacervation (Nihant et al., 1995). All of these techniques show some drawbacks, such as lack of control over particle size and particle size distribution, possible degradation of the product and high residual solvent (Wang et al., 2013). More specifically, Liang et al. (Liang et al., 2013) proposed the spray-drying of nanoemulsions for the encapsulation of BC in starch; they obtained highly irregular particles and did not report the dissolution tests to confirm an increase of BC dissolution rate. Yi at al. (Yi et al., 2015) used the homogenization-evaporation method to coprecipitate BC using sodium caseinate, whey protein and soybean protein as carriers; they obtained particles in the range 78-370 nm and compared the dissolution profiles of BC using the different carriers, but no comparison with the dissolution profile of unprocessed BC was proposed to demonstrate the improved bioavailability.

Franceschi et al. (Franceschi et al., 2008) and Priamo et al. (Priamo et al., 2010) proposed the application of the SAS-like solution enhanced dispersion with supercritical fluids (SEDS) technique for the encapsulation of BC in poly(3-hydroxybutirate-co-hydroxyvalerate (PHBV) using dichloromethane as the liquid solvent. They obtained powders formed by a large and irregular material, not characterizable in terms of size and morphology, and did not report dissolution tests and solvent residue analyses despite the toxicity of the used solvent. He at al. (He et al., 2007) used SEDS process for the coprecipitation of BC in poly-ethylene glycol (PEG) obtaining irregular flakes with a BC loading lower than 50 %; moreover, also in this case, the dissolution tests were missing. Hong et al. (Hong et al., 2007) proposed SEDS technique for the production of BC/proanthocyanidin microspheres; however, they obtained results similar to those previously described. Moreover, none of these authors proposed an explanation of the coprecipitation mechanisms.

In the hypothesis that PVP can exert a general positive effect in the formation of SAS coprecipitates, in this work, we applied SAS process to the coprecipitation of PVP/BC microparticles, to extend the applicability of this technique to other solutes and to gain more information about the involved precipitation mechanisms.

Experimental results

All SAS experiments were carried out using a CO_2 flow rate of 15 NL/min, a solution flow rate of 1 mL/min, at a temperature of 313 K. Since BC is soluble in Acetone (Jackson and Mantsch); whereas, PVP is soluble in Ethanol (EtOH), a mixture AC/EtOH 70/30 (v/v) was used as the liquid solvent. A preliminary check on the formation of a homogeneous solution of PVP/BC/EtOH/AC was made to be sure that one liquid phase without solute precipitation can be formed. Then, the effect of PVP molecular weight, PVP/BC w/w ratio, operating pressure and total concentration of solutes was investigated. A selection of the performed experiments is summarized in Table V.2, with the indication of the operating conditions employed, the obtained morphology and, in the case of particles, their mean diameter (m.d.) and standard deviation (s.d.). Each experiment was carried out in duplicate.

Table V.2 *Summary of SAS experiments performed on PVP/BC (MP: microparticles; NP: nanoparticles; C:crystals).*

#	MW_{PVP} g/mol	PVP/BC w/w	P MPa	C mg/mL	Morph	m.d. µm	s.d. µm
1	10000	*1/0*	8.5	5	MP	0.81	0.23
2	-	*0/1*			C	-	-
3	*40000*	10/1	8.5	5	NP	0.25	0.05
4	*10000*				MP	2.43	0.81
5	10000	10/1	*9.0*	5	MP	2.06	0.64
6			*10.0*		MP	1.24	0.44
7	10000	10/1	8.5	*3*	MP	1.15	0.50
8				*7*	-	-	-
9	10000	*15/1*	8.5	5	MP	1.70	0.51
10		*20/1*			MP	1.63	0.49

Two preliminary SAS experiments were performed using the solutes separately, to know their behavior under the same operating conditions. Both the tests were carried out at 8.5 MPa and 313 K; i.e., in proximity of the MCP of the system. These process conditions were selected because, in a previous work (Prosapio et al., 2015), it has been demonstrated that coprecipitation occurred when microparticles were formed. When BC alone was processed (in Table VI.1), the precipitate, from a macroscopic point of view, appeared as an orange powder that, observed at SEM, was formed by large and irregular particles. In Figure V.12, a FESEM image of the precipitated powder is reported. The micronization was clearly unsuccessful.

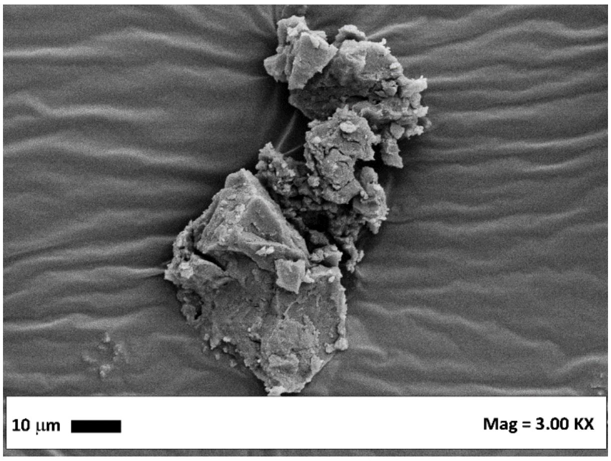

Figure V.12 *FESEM image of BC precipitated from AC/EtOH 70/30 at 8.5 MPa, 313 K and 5 mg/mL.*

PVP (Mw=10000 g/mol) alone, instead, when SAS processed using the same solvent mixture of the previous experiment, precipitated in form of a white powder characterized by microparticles with a mean diameter of 0.8 µm (#1 in Table V.2). A SEM image of this precipitate is shown in Figure V.13, as confirmation of the suitability of the polymer processing by SAS (Prosapio et al., 2015). This preliminary test on PVP alone was necessary, because, in a previous work (Prosapio et al., 2015), PVP was chosen to produce coprecipitates using dimethylsulfoxide (DMSO) as liquid solvent; therefore, the precipitation from EtOH/AC mixtures of PVP in form of microparticles had to be verified.

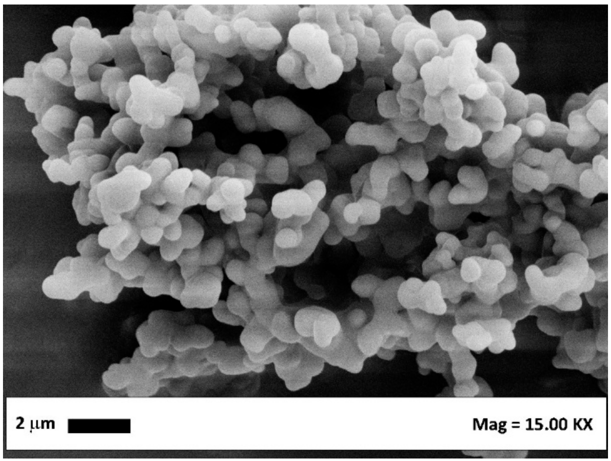

Figure V.13 *FESEM image of PVP precipitated from AC/EtOH 70/30 at 8.5 MPa, 313 K and 5 mg/mL.*

Summarizing the results of these preliminary tests, it is possible to observe that the two compounds show completely different behavior when SAS processed at the same operating conditions and that BC alone is a bad candidate for SAS micronization.

Effect of PVP molecular weight

In the first set of experiments the effect of the polymer molecular weight was investigated (#4 in Table V.2), working at the same conditions used in the previous experiments. The scope of these experiments was to select the most appropriate PVP molecular weight for the coprecipitation experiments.

First, a test was performed using a PVP with a molecular weight of 40000 g/mol (run #3 in Table V.2), fixing the polymer/vitamin ratio equal to 10/1. Then, the same experiment was carried out (run #4 in Table V.2) using a lower polymer molecular weight (10000 g/mol). It is very relevant to consider that, despite the two experiments were carried out at the same operating conditions, the obtained powders had a different color. In particular, using the polymer with the higher molecular weight the powder was orange with some white points, suggesting that probably the two solutes precipitated separately (Figure V.14a). The powder obtained using the PVP with the lower molecular weight, instead, showed a yellow color that was intermediate between that of BC and PVP alone (Figure V.14b). This result is the visual evidence that, in this case, probably the coprecipitation is successful; this hypothesis has been adequately demonstrated in the following parts of the work.

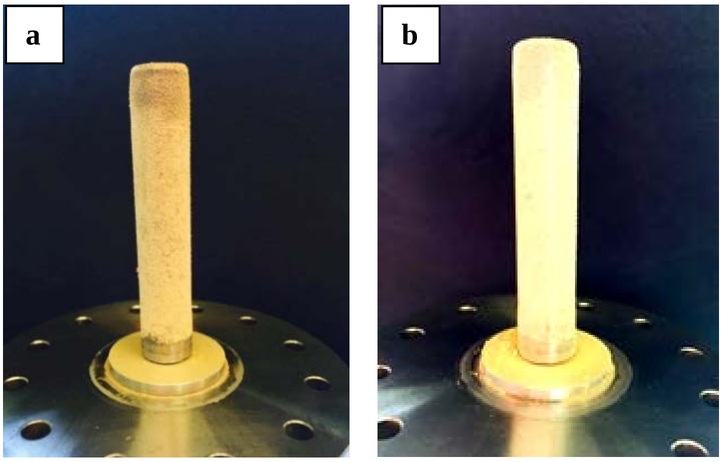

Figure V.14 *Photos of the filter of PVP/BC 10:1 processed at 8.5 MPa, 313 K, 5 mg/mL: a) PVP molecular weight of 40000 g/mol; b) PVP molecular weight of 10000 g/mol.*

The microscopic analysis of the powders of different molecular weight PVP showed that, in the case of the higher molecular weight PVP, slightly coalescing nanoparticles were obtained, as showed in the FESEM image reported in Figure V.15a; whereas, the powder obtained using the lower molecular weight PVP is formed by spherical microparticles with a mean diameter of about 2.64 μm, as shown in Figure V.15b. The comparison of the FESEM images of the powders obtained from the two experiments showed that the morphology obtained using the lower molecular weight polymer is more compatible with a coprecipitation. Indeed, on the basis of a previous work (Prosapio et al., 2015), it is expected that coprecipitates are formed by microspheres. Therefore, of the lower molecular weight PVP was used in the experiments that follow.

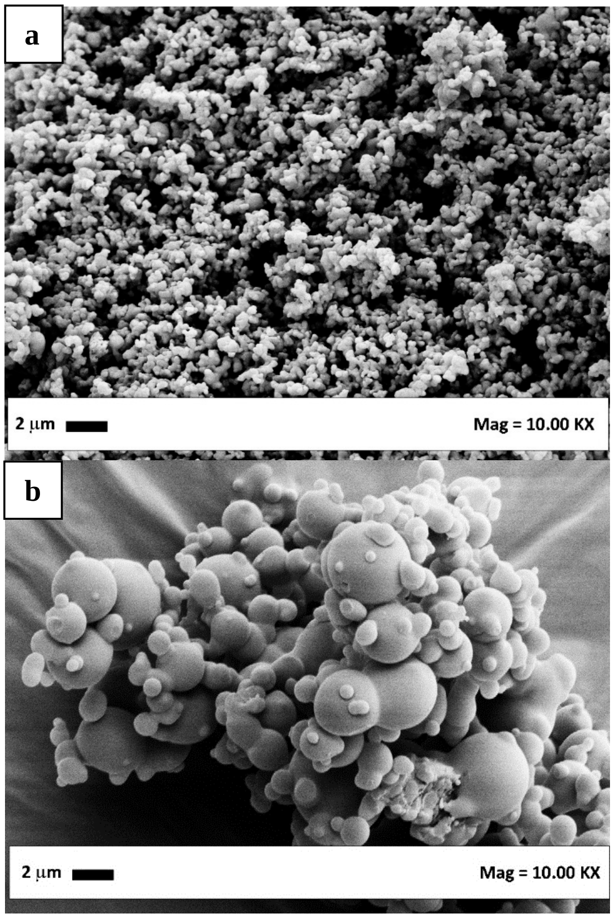

Figure V.15 *FESEM images of PVP/BC 10:1 processed at 8.5 MPa, 313 K, 5 mg/mL: a) PVP*

Effect of Polymer/Vitamin Ratio

The second parameter taken into account was the polymer/vitamin ratio, which was increased first at 15/1 and then at 20/1 (-10 in Table VI.2), keeping constant the other process parameters.

When PVP/BC 15/1 was processed, a yellow powder was again obtained, but it was characterized by a lighter yellow color: this result was expected and can be attributed to the larger amount of PVP used with respect to the vitamin. The FESEM images (an example is reported in Figure V.16a) showed the presence of slightly coalescing microparticles. Processing PVP/BC 20/1, a larger coalescence is visible, as shown in the FESEM image reported in Figure V.16b and the yellow color intensity further decreases.

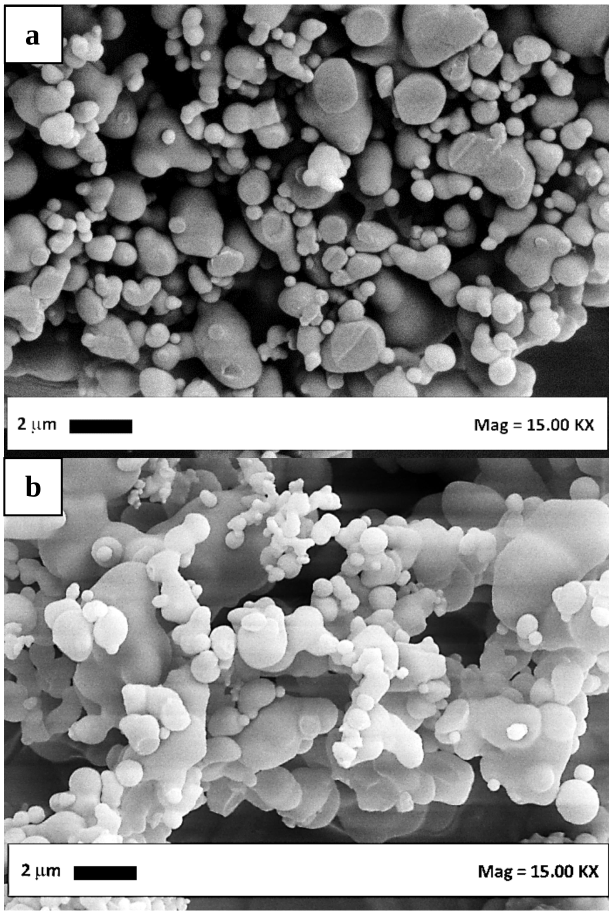

Figure V.16 *FESEM images of PVP/BC particles precipitated from AC/EtOH 70/30 at 85 MPa and 313 K at different polymer/drug ratios: (a) 15/1 w/w, (b) 20/1 w/w.*

These two last experiments showed that, increasing the PVP/BC ratio from 10/1 to 20/1 , a worsening of particle morphology occurred. Moreover, to produce powder with the largest BC content, it is possible to state that the best proportion between the two solutes is 10/1, that was fixed for the subsequent experiments.

Effect of the operating pressure

The effect of the operating pressure on PVP/BC coprecipitates morphology, particle size and particle size distribution was, then, investigated, fixing the polymer/vitamin ratio at 10/1. The pressure range explored was between 8.5 and 10.0 MPa, since in a previous work

(Prosapio et al., 2015) it was observed that good conditions for a successful coprecipitation are located near above the mixture critical point (MCP) of the binary system solvent/CO_2. An experiment was carried out at 9.0 MPa; in correspondence of these operating conditions, spherical microparticles (Figure V.17a) with a mean diameter of about 2 µm were obtained, as it is possible to observe from the SEM image and from data in Table V.2 (run #5). When the process pressure was increased to 10.0 MPa, slightly smaller microparticles were produced (see run #6 in Table V.2), as shown in Figure V.17b.

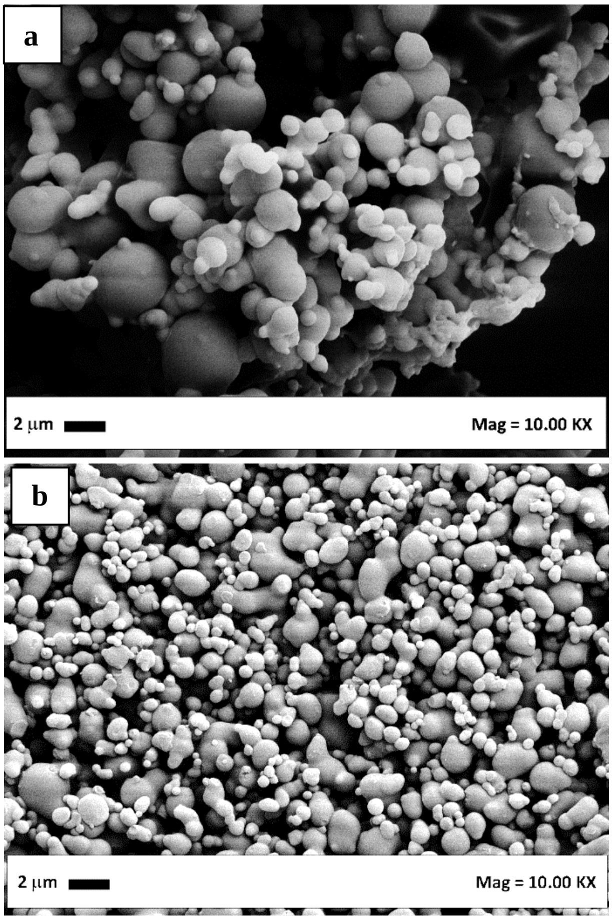

Figure V.17 *FESEM images of PVP/BC particles precipitated from AC/ETOH 70/30 at 313 K and different pressures: (a) 9.0 MPa; (b) 10.0 MPa.*

Comparing the volumetric particle size distributions of the particles, it is possible to observe that, increasing the operating pressure, the particle size reduced and the PSD became narrower, as can be seen in

Figure V.18. This result is in agreement with SAS literature (E. Reverchon, 2011), as we will see in the discussion of the results.

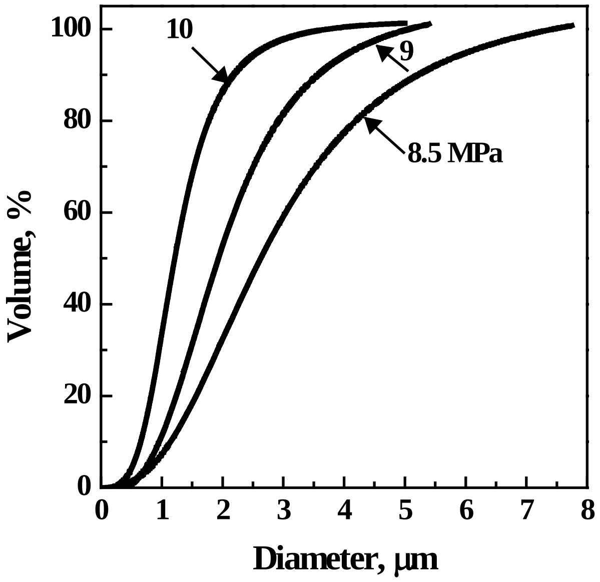

Figure V.18 *Volumetric particle size distributions of PVP/BC 10/1 coprecipitates obtained at different pressures.*

Effect of the total solute concentration

The effect of the total concentration of solutes in the liquid solution was studied at 8.5 MPa, 313 K and fixing PVP/BC at 10/1. Using as a reference the experiment #4, two experiments with a higher and a lower concentration were performed. Using an overall concentration equal to 3 mg/mL, well separated microparticles with a mean diameter of 1.15 μm were obtained. Increasing the concentration at 7 mg/mL, highly coalescing particles were produced, which cannot be characterized in terms of dimensions. Comparing the results obtained at 3 and 5 mg/mL, it is possible to observe that increasing the concentration the mean diameter increased and the particle size distribution become wider.

Analyses on precipitates

To evaluate the quantity of vitamin present in the coprecipitates and its dissolution profiles, UV-vis analyses were performed on the processed samples and on unprocessed BC. Drug entrapment efficiency analyses revealed that the powders of PVP/BC 10/1, processed at 8.5 MPa and 313 K, obtained using the polymer with the higher molecular weight show a drug content equal to 70 % with respect to the initial value; whereas, the powders obtained using the polymer with the lower molecular weight show a drug content near 100 % with respect to the initial value.

The dissolution rate of each sample was monitored for 80 hours by plotting the percentage of dissolved β-Carotene as a function of time. The analyses were performed for unprocessed β-Carotene, SAS processed PVP/BC 10/1 with a PVP molecular weight of 40000 g/mol and with a PVP molecular weight of 10000 g/mol; all results are shown in Figure V.19. The profile of the untreated vitamin shows a complete dissolution time in 80 hours. The sample formed by PVP/BC nanoparticles, obtained using the polymer with higher molecular weight, instead, shows a faster dissolution rate, reaching the 100% dissolution in 40 hours. However, only the sample formed by PVP/BC microparticles obtained with the lower polymer molecular weight shows a radically different behavior, with a dissolution profile in which the 100 % of the vitamin was released in only 8.5 hours. Therefore, for PVP/BC microparticles the dissolution rate of the vitamin was 5 times faster than PVP/BC nanoparticles and 10 times faster than the unprocessed BC.

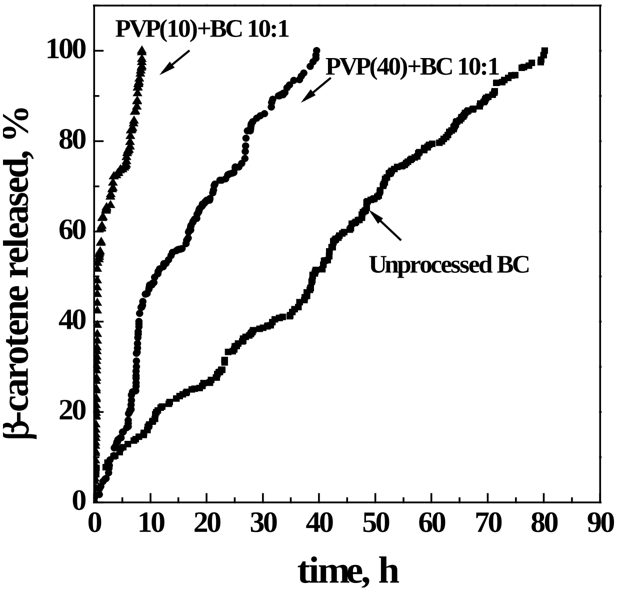

Figure V.19 *Dissolution profiles of BC in PBS at 310 K and pH 7.0.*

V.2.3 PVP/corticosteroids coprecipitates

Corticosteroids are a class of steroid hormones, largely used as anti-inflammatory drugs for the treatment of ocular (Muñoz-Fernández and Martín-Mola) and pulmonary (Diette et al., 2015) diseases, hepatitis (Yeoman et al., 2014) and ulcers (Zhou et al., 2015). Some of the most widely used drugs in this category are dexamethasone (DMS), prednisolone (PDN) and budesonide (BDS). They show a low water solubility (< 1 mg/100 mL) and consequently low bioavailability (Gómez-Gaete et al., 2007, Chen et al., 2015b); therefore, large doses are required to reach the therapeutic level, that can produce some undesired effects, like high sugar concentration in blood, hypertension, stomach and intestinal ulcers, fluids retention (Urbańska et al., 2014). To improve their dissolution rate, a possible solution is represented by their particle size reduction at micrometric diameters.

Traditional micronization techniques such as spray drying, jet milling and solvent evaporation show several drawbacks: lack of control over the particle morphology and particle size distribution, difficulty in the elimination of the solvent and use of high temperatures (Wang et al., 2013). Tajber et al. (Tajber et al., 2009) proposed the micronization of BDS using a spray drying technique; they obtained amorphous microparticles in the range 1-7 µm; but, they did not demonstrate the improvement of the dissolution rate. Rasenack et al. (Rasenack et al., 2003) used a controlled crystallization process to micronize several anti-inflammatory drugs, among which budesonide and prednisolone, obtaining large and irregular crystals; also in this case, dissolution tests were not performed. Another approach to increase drug dissolution rate is to produce composite microspheres drug-polymer, using a water soluble polymer in which the drug is entrapped. The fast solubilization of the polymer should release the drug in nanometric subparticles. Rodrìguez et al. (Rodríguez et al., 1998) prepared cellulose acetate butyrate-budesonide microspheres by emulsion-solvent evaporation using acetone and methanol as solvents; they obtained particles larger than 200 µm with an encapsulation efficiency lower than 75 %, and did not report neither the residual solvent analysis, nor the comparison of the dissolution profiles between unprocessed BDS and coprecipitated powder.

When processed using SAS, corticosteroids precipitate in form of large crystals (Velaga et al., 2002, Velaga et al., 2004, Steckel et al., 1997) , without improvement of the dissolution rate with respect to the unprocessed drugs. SAS is governed by complex high pressure equilibria, fluid dynamics interactions and mass transfer (Reverchon et al., 2010, De Marco et al., 2015 (Chávez et al., 2003a). In the case of corticosteroids, large crystals are produced as a result of the partial solubility of these drugs in the mixture solvent/antisolvent, that can modify the corresponding vapor-liquid equilibria (VLE) with consequent shift of the mixture critical point (MCP) towards higher pressures. As previously discussed, to improve the dissolution rate, a possible solution is represented by the coprecipitation with a biodegradable polymeric carrier in form of microspheres. However, examples of SAS coprecipitation are rather limited, because of the difficulty to produce composite microspheres using this process. Indeed, the two compounds tend to precipitate separately.

Therefore, in this work (Prosapio et al., 2016a), to overcome SAS limitation in producing corticosteroids microparticles and to extend the application of SAS coprecipitation, three corticosteroids, dexamethasone (DMS), prednisolone (PDN) and budesonide (BDS), are processed trying to take advantage of PVP ability to retard crystal growth (Ledet et al., 2015b, Sun et al., 2012, Van den Mooter et al., 2001). The effect of polymer/drug ratio, operating pressure and overall solute concentration will be investigated to understand their effect on the success of coprecipitation and on particle morphology, mean size and particle size distribution. Precipitation mechanisms will be discussed, drug entrapment efficiency and dissolution tests of coprecipitates will be performed to verify process efficiency.

Experimental results

SAS experiments were performed using a CO_2 flow rate of 10 NL/min, a solution flow rate of 1 mL/min and EtOH as the liquid solvent. The effects of polymer/drug w/w ratio, operating pressure and total concentration were investigated. Table V.3 reports a list of the experiments, with the indication of the obtained morphology, mean diameter (m.d.) and standard deviation (s.d.).

Table V.3: *Summary of SAS experiments (MP: microparticles, SMP: sub-microparticles; C: crystals; m.d.: mean diameter; s.d.: standard deviation).*

#	Polymer/Drug (w/w)	P [MPa]	C [mg/mL]	Morph.	m.d. [µm]	s.d. [µm]
1	1:0	9	20	MP	4.11	1.62
2	1:0	15		MP	2.41	1.52
PVP/DMS						
3	0:1	15		C	-	-
4	0:1			C	-	-
5	2:1			C+SMP	-	-
6	3:1	9	20	MP	1.82	1.22
7	5:1			MP	2.14	1.46
8	10:1			MP	2.48	1.78
9	20:1			MP	2.51	1.79

PVP/PDN						
10	0:1	15	20	C	-	-
11	0:1	9		C	-	-
12	2:1			C+SMP	-	-
13	3:1			MP	1.96	1.21
14	5:1			MP	2.40	1.73
15	10:1			MP	2.45	1.85
16		15		MP	2.21	1.39
17		9	10	MP	2.01	1.28
18			30	MP	3.10	1.39
19	20:1		20	MP	3.03	1.99
PVP/BDS						
20	0:1	15	20	C	-	-
21	0:1	9		C	-	-
22	1:1			C+SMP	-	-
23	2:1			MP	3.06	1.03
24	3:1			MP	3.12	1.25
25	5:1			MP	3.27	1.78
26	10:1			MP	3.37	1.85
27	20:1			MP	3.58	1.88

A first set of experiments was performed processing the corticosteroids alone, to confirm the results observed in the literature. These experiments were first performed operating at 9 MPa, 313 K and a solute concentration of 20 mg/mL (#4,11,21 in Table V.3). At these process conditions, all the corticosteroids (DMS, PDN and BDS) precipitated in form of large crystals. Then, to verify if these results are limited to lower SAS operating pressures, the three compounds were processed at 15 MPa and 313 K (#3,10,20 in Table V.3). The same morphology was observed, as shown, for example, in the FESEM images reported in Figure V.20. Therefore, the confirmation that using SAS, corticosteroids precipitate in form of crystals, irrespective of the process conditions selected, was obtained.

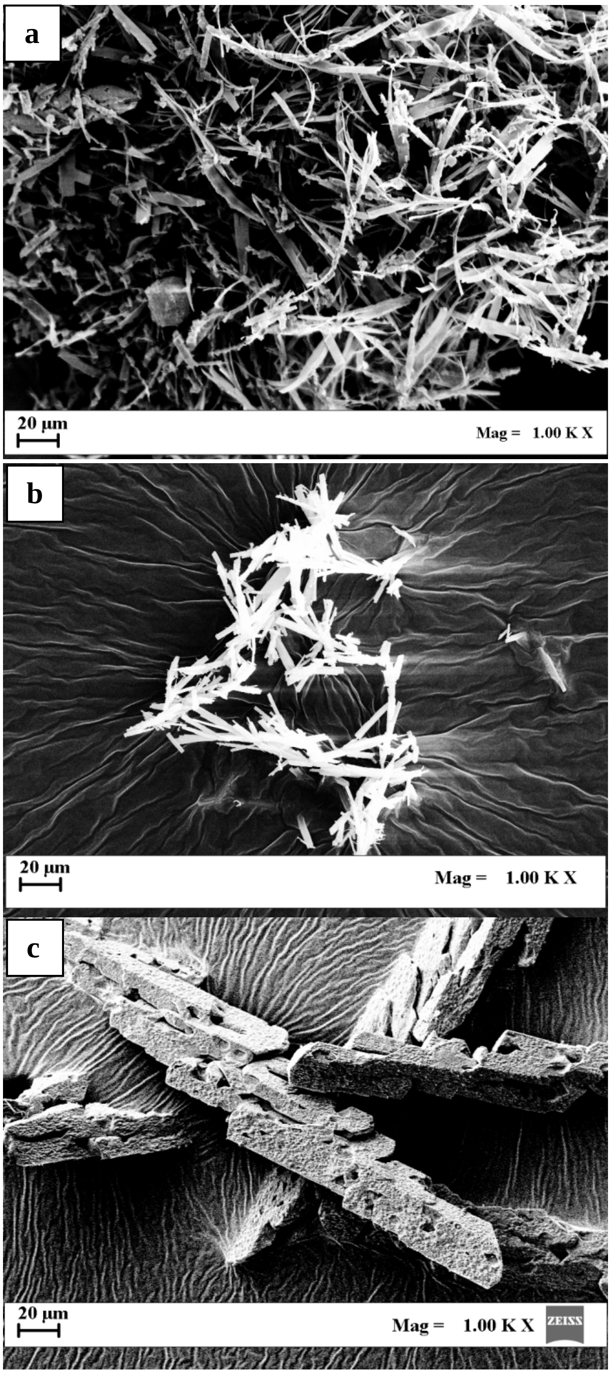

Figure V. 20 *FESEM images of corticosteroids precipitated from EtOH at 15MPa, 313 K and a concentration of 20 mg/mL: a) DMS, b) PDN; c) BDS. Large crystals were obtained in all cases.*

Then, PVP was processed at the same two operating conditions (#1,2 in Table V.3). Rossmann et al. (Rossmann et al., 2014) and De Marco et al. (De Marco et al., 2012) observed that, when PVP is SAS processed from ethanol, it precipitates in form of microparticles, independently on the operating pressure, in the range 9-30 MPa. Our results confirmed their observation: at 9 and 15 MPa, well separated spherical microparticles were produced. In Figure V.21, an example of FESEM image of PVP particles obtained at 15 MPa is reported. Comparing the mean size and the standard deviation of the particles obtained from these two experiments (Table V.3), it is possible to observe that, increasing the operating pressure, the mean diameter of the particles decreased and the particle size distribution shrank.

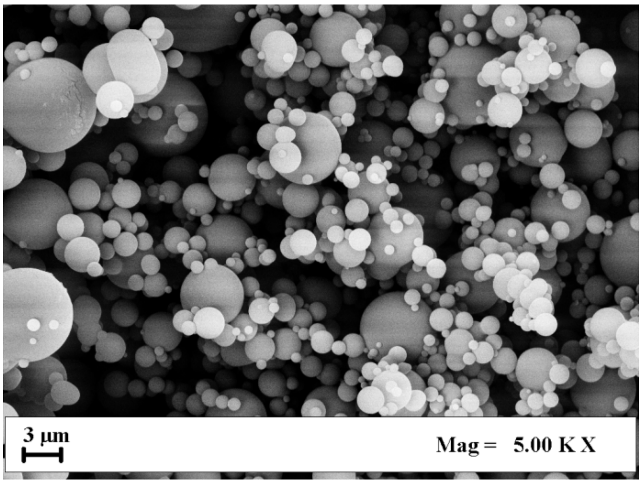

Figure V. 21 *FESEM image of PVP microparticles precipitated from EtOH at 15 MPa, 313 K and 20 mg/mL.*

The comparison of the FESEM images of corticosteroids and PVP (Figures V.20 and V.21) clearly shows that the polymer and the drugs precipitate with a complete different morphology, even when processed at the same SAS operating conditions. PVP is a good candidate for coprecipitates formation, since it can interfere with the crystallization kinetics of some compounds like folic acid and β-carotene producing composite microspheres. To verify if PVP can work in the same manner for corticosteroids, we performed SAS experiments using PVP as the carrier and DMS, PDN or BDS as the active compounds. To this purpose, the effect of: polymer/drug ratio, operating pressure and total concentration of the two solutes in EtOH was studied.

Effect of PVP/drug ratio

For each corticosteroid, the effect of polymer/drug ratio on particles morphology, mean size and particle size distribution was investigated at 9 MPa and 313 K, using different polymer/drug ratios.

When PVP/drug 2:1 ratios (#5,12,23 in Table V.3) were processed, crystals and coalescing sub-microparticles were observed in the case of DMS and PDN, as shown in the FESEM images in Figure V.22a and V.22b; therefore, the samples could not be characterized in terms of dimensions as coprecipitation is substantially unsuccessful: the two compounds precipitated as separated particles/crystals. In the case of BDS, instead, microparticles with a mean diameter equal to 3.06 µm were produced, as shown in Figure V.22c. Since this last result differs from the ones obtained for DMS and PDN, a further experiment was performed fixing PVP/BDS at 1:1, to identify a possible transition from crystals to microparticles; indeed, in this test, crystals and coalescing sub-microparticles were obtained.

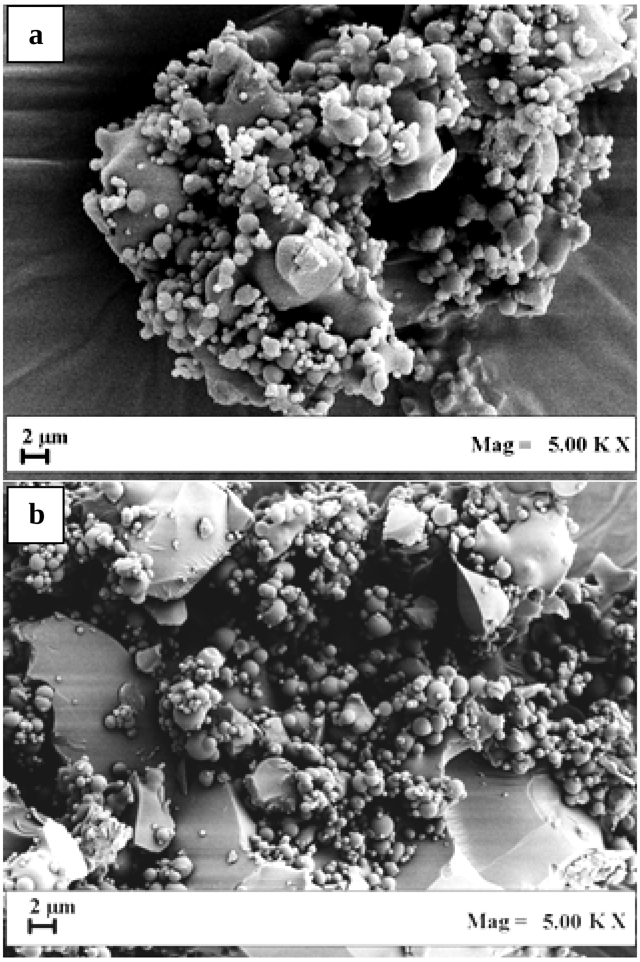

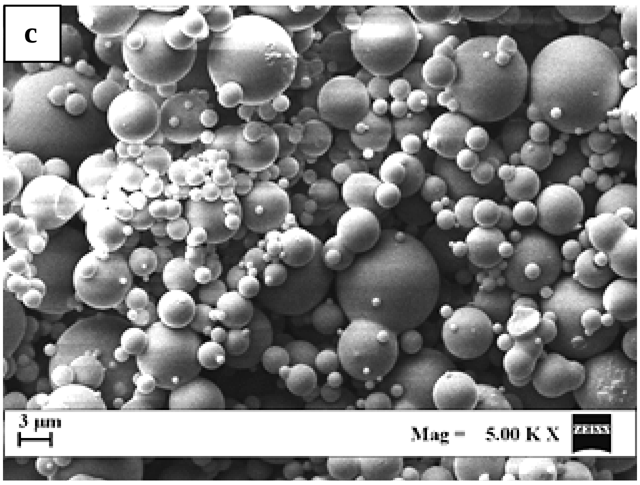

Figure V. 22 *FESEM images of PVP/corticosteroids 2:1 particles precipitated from EtOH at 9 MPa, 313 K and 20 mg/mL: a) PVP/DMS, b) PVP/PDN; c) PVP/BDS.*

In the subsequent experiments, the ratio PVP/drug was increased at 3:1 (#6,13,24 in Table V.3) for all systems. Operating at these conditions, microparticles were obtained in all cases. Also when we increased the polymer/drug ratio at 5:1 (#7,14,25), as showed in the exemplificative FESEM images reported in Figure V.23, and at 10:1 (#8,15,26) and 20:1 (#9,19,27), well separated spherical microparticles were obtained in all cases.

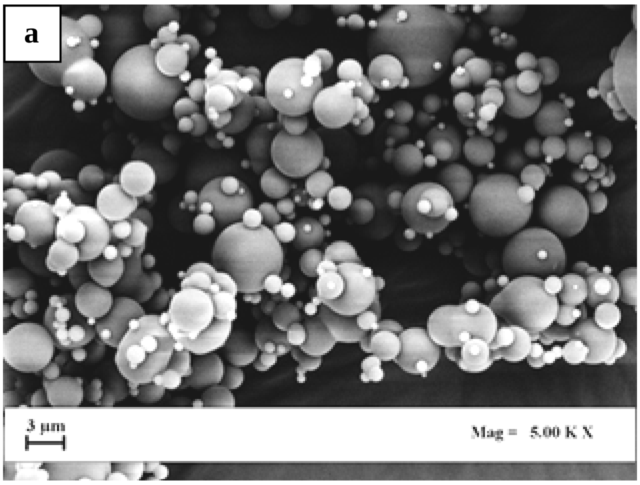

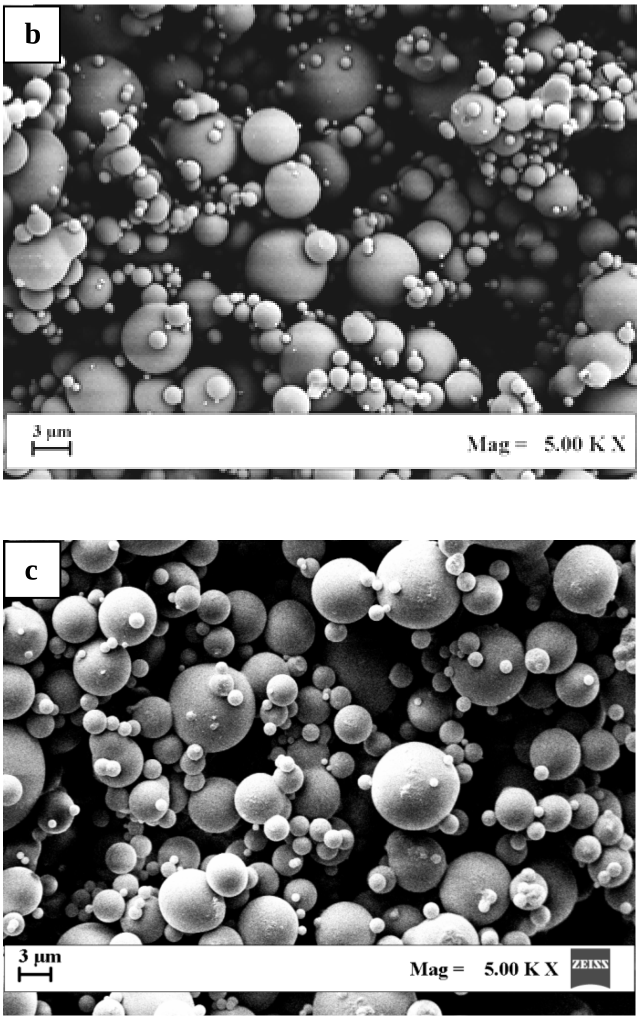

Figure V. 23 *FESEM images of PVP/corticosteroids 5:1 particles precipitated from EtOH at 9 MPa, 313 K and 20 mg/mL: a) PVP/DMS, b) PVP/PDN; c) PVP/BDS.*

Comparing the volumetric PSDs obtained at different polymer/drug ratios, it is possible to note that, increasing the percentage of polymer in the injected solution, the mean size of the particles increased and the PSD become wider in the case of PVP/DMS and PVP/PDN particles, as shown in Figure V.24, whereas not significant variations in the mean diameter were observed in the case of PVP/BDS particles (see Table V.3).

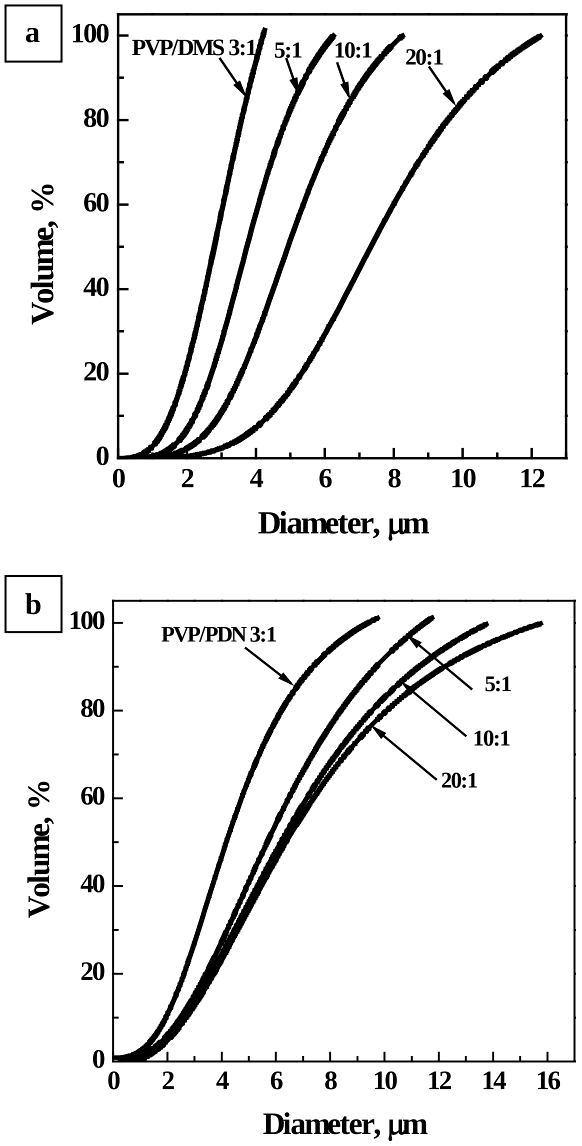

Figure V. 24 *Volumetric cumulative PSDs of microparticles precipitated from EtOH at 9MPa and 313 K at different polymer/drug ratios: a) PVP/DMS, b) PVP/PDN.*

Effect of the operating pressure

To study the effect of the operating pressure, an experiment was performed at 15 MPa for the system PVP/PDN 10:1 (#16 in Table V.3), keeping constant all the other operating parameters at the values previously proposed. The FESEM images of the powders produced, confirmed that they were formed by microparticles, as shown in Figure V.25, and a mean diameter of 2.21 µm was measured by image analysis .

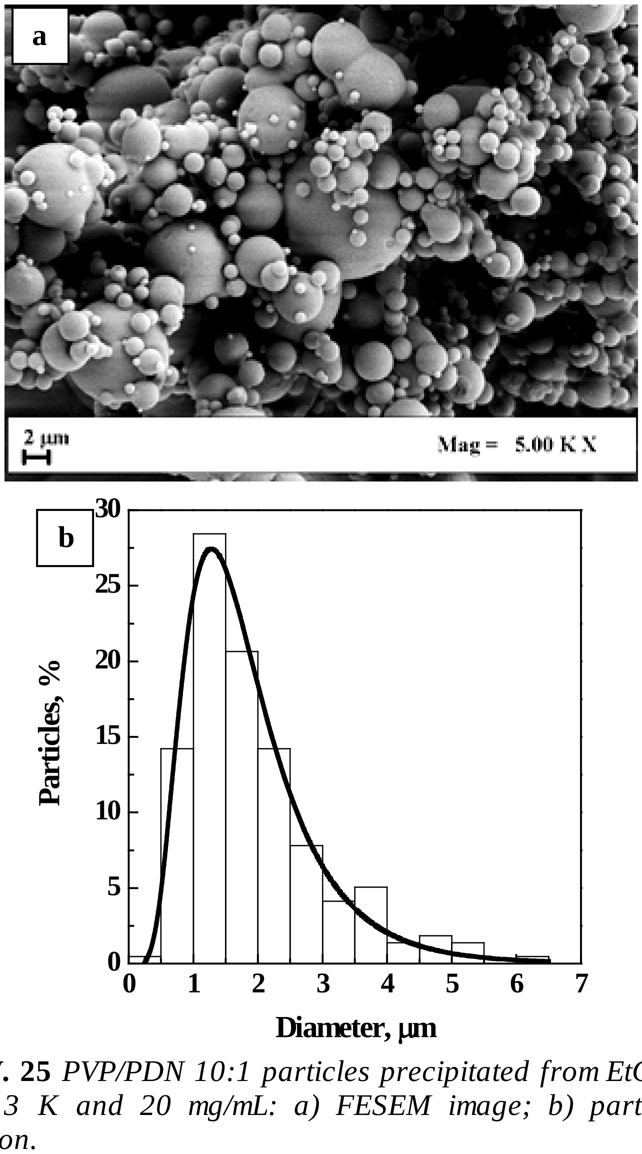

Figure V. 25 *PVP/PDN 10:1 particles precipitated from EtOH at 15 MPa, 313 K and 20 mg/mL: a) FESEM image; b) particle size distribution.*

This result is interesting, since at these process conditions the SAS operating point is located far above the MCP of the binary system CO_2/EtOH and, as a consequence, nanoparticles should be produced, as largely discussed in the literature. The system PVP/PDN follows, instead, the same behavior of PVP alone that, as mentioned above, precipitates from ethanol in form of microparticles at pressures up to 30 MPa; i.e., the quantity of polymer that is present in the system controls its overall morphology even at higher pressures tested. This experimental evidence for PVP is still under investigation.

Effect of concentration

The effect of the total concentration PVP/corticosteroid in EtOH was investigated for the system PVP/PDN 10:1 at 9 MPa and 313 K, varying the overall concentration from 10 mg/mL to 30 mg/mL (#17-18 in Table V.3); data at 20 mg/mL was already available (#15). Using an overall concentration of 10 mg/mL, microparticles were produced, as shown in Figure V.26a, with a mean diameter equal to about 2 µm; increasing the concentration at 30 mg/mL, as shown in Figure V.26c, microparticles were still obtained, but with a mean size of 3.5 µm.

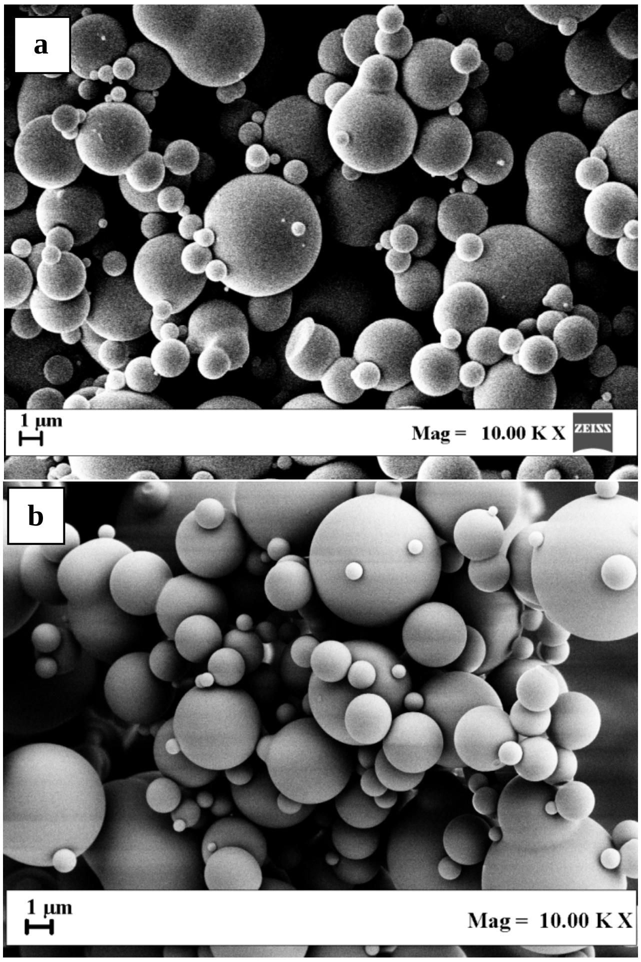

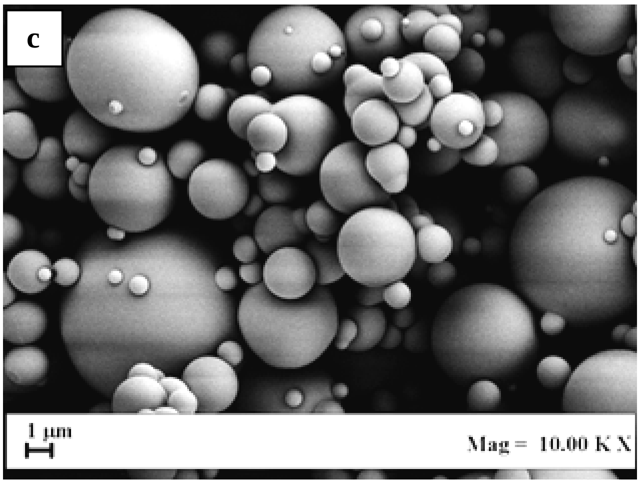

Figure V. 26 *FE-SEM images of PVP/PDN 10:1 particles precipitated from EtOH at 9 MPa, 313 K and different concentrations: a) 10 mg/mL; b) 20 mg/mL; c) 30 mg/mL.*

Comparing the volumetric PSD of the particles obtained at different concentrations, it is possible to observe that, increasing the concentration, the particle mean size increase and the PSD enlarges, as reported in Figure V.27, this result is in agreement with several other experimental observations on SAS precipitates, reported in the literature.

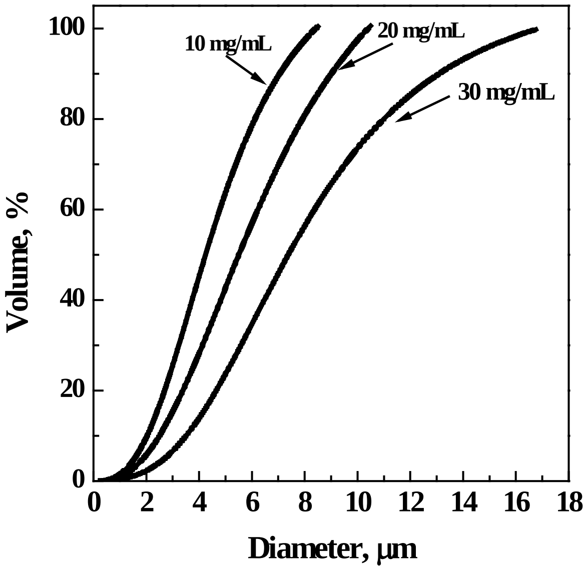

Figure V. 27 *Volumetric cumulative PSDs of PVP/PDN 10:1 particles precipitated from EtOH at 9 MPa and 313 K at different concentrations.*

Characterization of precipitates

Differential scanning calorimetry (DSC) analyses were performed on unprocessed drugs and polymer, physical mixtures PVP/corticosteroids and SAS processed PVP/corticosteroids 5:1, to determine the changes in the thermal transition of the drugs and the polymer in the coprecipitates. The analyses revealed that: the unprocessed drugs show all a narrow endothermic peak in correspondence of about 563 K; unprocessed PVP shows a broad endothermic peak ranging from 323 to 403 K; the physical mixtures show both the polymer and drug peaks; SAS processed PVP/corticosteroids show both the endothermic peaks but, in all the cases, the peak of the drug is remarkably reduced in its intensity. This last result could be due to the higher presence of the polymer with respect to the drug and indicates the presence of both the compounds in the powder.

Fourier transform infrared (FT-IR) analyses were performed to identify possible interactions between the drug and the carrier in the coprecipitates. FT-IR spectra of unprocessed drugs and PVP, physical mixtures PVP/corticosteroids 5:1 and SAS processed PVP/corticosteroids 5:1 are reported in Figure V.28. The spectra of unprocessed corticosteroids show characteristic absorption bands in the range 1600-1700 cm^{-1} related to the stretching vibration of C=O carbonyl groups, a characteristic absorption band in the range 2750-3100 cm^{-1} related to the stretching vibration of the C–H group and a characteristic absorption band in the range 3100-3700 cm^{-1} related to the stretching vibration of the –OH groups. The spectrum of PVP shows a characteristic absorption band at 1653 cm^{-1} which belongs to the stretching vibration of C=O groups, a C–H stretching vibration at 2873 cm^{-1} and a –OH stretching vibration at 3469 cm^{-1}. The spectra of the physical mixtures PVP/corticosteroids and of processed PVP/corticosteroids spectra show the same characteristic bands related to the carbonyl stretching, –OH stretching and C–H stretching; this result suggests the presence of both the compounds in the samples but does not indicate the existence of a well-defined interaction between them

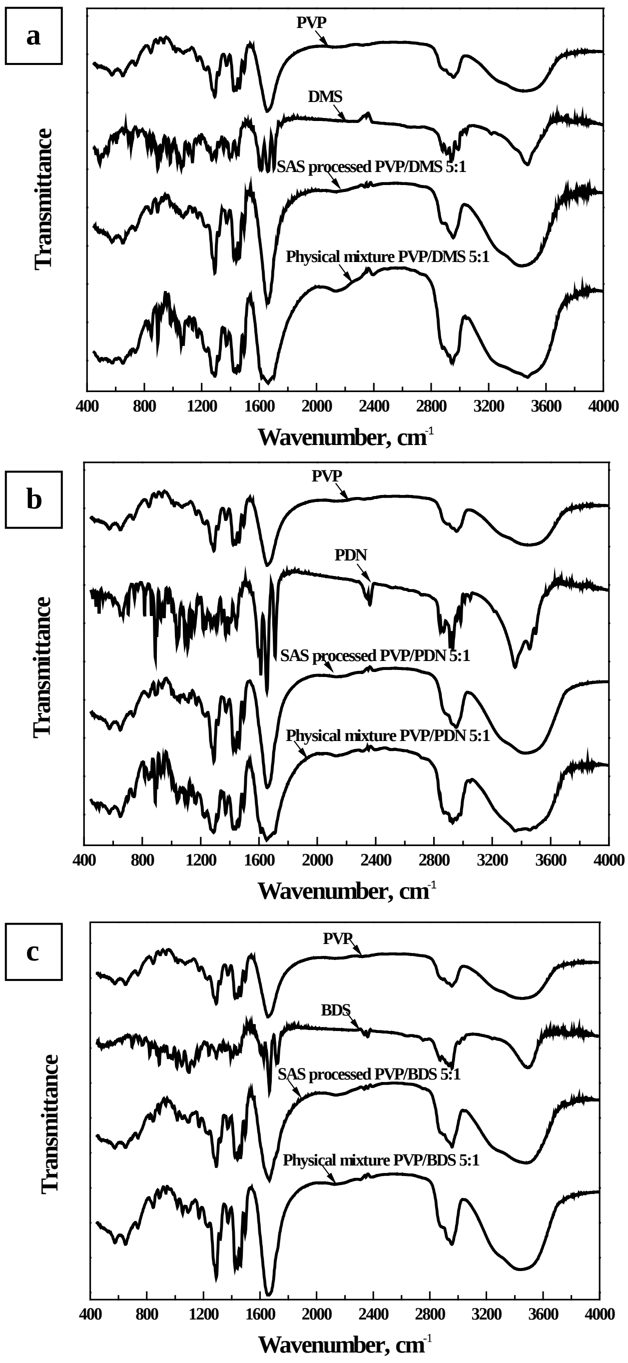

Figure V. 28 *FT-IR spectra of unprocessed, physical mixtures and SAS processed PVP/corticosteroids: a) dexamethasone; b) prednisolone; c) budesonide.*

In order to demonstrate the successful coprecipitation of the drug and the polymer and the improvement of corticosteroids dissolution rate, drug entrapment efficiency and drug release tests were performed using UV-vis spectroscopy analyses. Drug entrapment efficiency analyses revealed that the samples PVP/DMS, PVP/PRN and PVP/BDS show a drug content ranging between 90 and 95 % with respect to the initial value. For dissolution tests, the samples taken into account were: unprocessed drugs, SAS processed drugs (#4,11,21) and SAS processed coprecipitates PVP/drug 5:1 (#7,14,25). During the analyses, the dissolution rate of each sample in PBS was monitored plotting the percentage of dissolved drug as a function of time. In Figure V.29a, the dissolution profiles of dexamethasone are reported; it is possible to observe that both unprocessed and SAS processed DMS achieve the complete dissolution in 25 hours; whereas, the sample PVP/DMS 5:1 has a faster dissolution rate and arrives at 100 % in about 6 hours. In Figure V.29b, the dissolution profiles of prednisolone are shown: unprocessed PDN achieves the complete dissolution in about 70 hours; SAS processed PDN achieves the 100 % release also in 70 hours, but, the curve shows a higher slope in the first part; the coprecipitate PVP/PDN 5:1, instead, concludes its dissolution in only 14 hours. In Figure V.29c, the dissolution profiles of budesonide are reported; unprocessed BDS reaches the complete dissolution in 90 hours; SAS processed BDS dissolves slightly faster, but, achieves the 100 % release also in 90 hours; the coprecipitate PVP/BDS 5:1, instead, accomplishes its dissolution in 20 hours. Summarizing, in all cases, the unprocessed and SAS processed corticosteroids show very similar dissolution behavior; whereas PVP/drug coprecipitates show a very fast dissolution, from about 4.2 to 5 times faster!

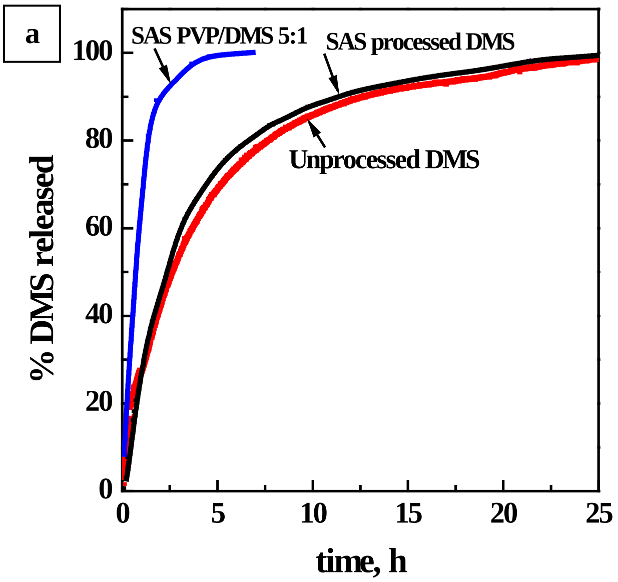
a
SAS PVP/DMS 5:1
SAS processed DMS
Unprocessed DMS
% DMS released
0
20
40
60
80
100
0
5
10
15
20
25
time, h

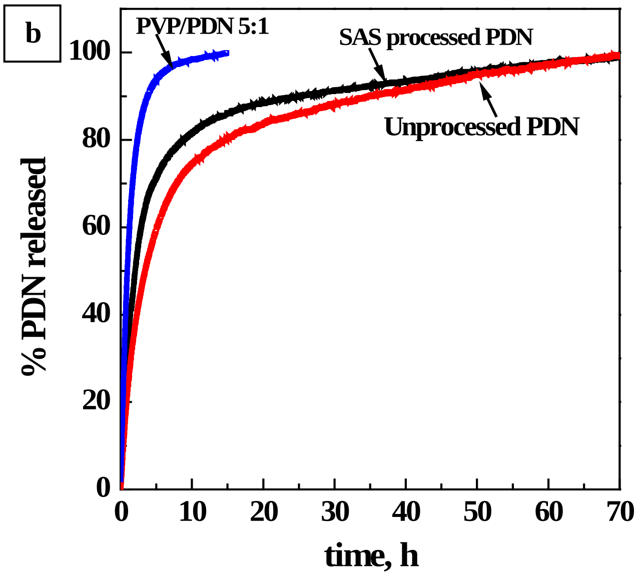
b
PVP/PDN 5:1
SAS processed PDN
Unprocessed PDN
% PDN released
0
20
40
60
80
100
0
10
20
30
40
50
60
70
time, h

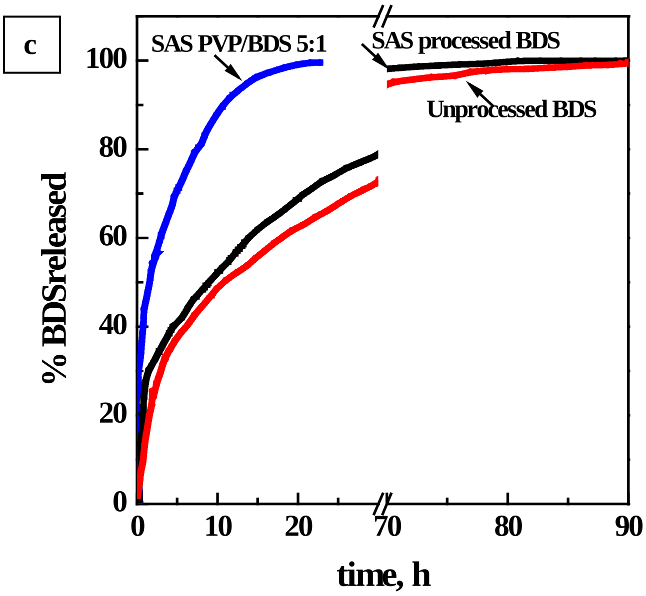

Figure V. 29 *Dissolution profiles in PBS at 310 K and pH 7.4: a) DMS; b) PDN; c) BDS.*

According to Food and Drug Administration (FDA) guidelines, ethanol belongs to class 3 residual solvent; therefore, its maximum acceptable concentration in the final product is 5000 ppm. A headspace sampler, coupled to a gas chromatograph, was used to verify the solvent residue content in SAS produced microspheres. The analysis revealed that the solvent residue was around 100 ppm!

V.2.4 Interpretation of results

As stated in the Introduction, SAS coprecipitation is difficult to be obtained. An explanation of this problem is given by the analysis of the precipitation processes that are activated during this operation. Nanoparticles are obtained by a gas-to-particle nucleation process, followed by a growth mechanism; this process is generally activated when the operating point is located far above the MCP of the studied system organic solvent-antisolvent (Reverchon et al., 2010). Microparticles are produced by jet break-up, droplet formation and drying, as a result of the atomization process and of the very fast solvent extraction operated by $scCO_2$; this precipitation mechanism is favored at process conditions near the MCP.

If we try to extend this interpretation to precipitates observed in this work, droplets formation and their consequent drying can be applied to microspheres formation. Each droplet behaves as a confined reactor and all its content concurs to the formation of the final microparticle. To obtain this result, the time of jet break-up (t_{jb}) has to be smaller than the time of surface tension vanishing (t_{st}) (E. Reverchon, 2011).

In this work, it is evident that folic acid, β-carotene and corticosteroids alone tend to produce crystals; PVP, instead, depending on its molecular weight tends to produce spherical particles of different mean size. The key question was: due to its capacity to block and control the morphology of the compound precipitating in its presence, can PVP force the coprecipitation of FA, BC and corticosteroids, producing microdroplets according to the second discussed SAS mechanism and obtain a successful coprecipitation?

In the experiments performed near above the MCP of the binary system CO_2/solvent, spherical microparticles are produced and, due to their hypothesized formation mechanism, it is obvious that they are formed by both PVP and the vitamin. This nanostructured composite system showed a very fast release rate. Summarizing, at selected SAS processing conditions, the presence of PVP is able to modify FA, BC and corticosteroids precipitation, blocking nanoparticles growth inside the PVP structure.

For the experiments carried out, instead, far above the MCP, the drug release analyses revealed that coprecipitation did not occur. The explanation is relatively simple. The usual mechanism to form nanoparticles by nucleation and growth is homogeneous nucleation. Indeed, in literature (York et al., 2002), it is reported that, when the supersaturation is high, as in the case of gas mixing, heterogeneous nucleation does not take place and the mechanism governing the precipitation is the primary homogeneous nucleation. In this case, therefore, the two species (polymer and active compound) tend to precipitate separately (Prosapio et al., 2015) forming a sort of intimate physical mixture: coprecipitation is substantially unsuccessful. This nanometric physical mixture is more rapidly dissolved with respect to the unprocessed and SAS processed drug, but does not drastically change the dissolution rate of drug as in PVP+drug microparticles in which the drug precipitated in PVP probably forms even smaller nanostructures.

We discovered that PVP molecular weight also plays an important role in successful coprecipitation; indeed, the nanoparticles obtained using PVP 40000 g/mol, show a nucleation and growth process that induces separate precipitation of the two solutes, confirmed by the color of coprecipitates, but also by the β-carotene release tests. When PVP 10000 g/mol is used, microparticles are obtained, whose color is intermediate between the ones of BC and PVP; also their morphology (spherical microparticles) indicates that the coprecipitation mechanism could be successful in this case. This result is confirmed by BC release tests: the dissolution process is concluded in only 8.5 hours that is about 10 times faster than β-carotene alone and about 5 times faster than the intimate physical mixture formed when nanoparticles were obtained. Moreover, all (100 %) BC was recovered in the precipitates, whereas, only 70 % was present in the case of nanoparticles formation. The missing BC was probably lost by dissolution in the supercritical mixture solvents+CO_2 in the precipitator.

The final consideration is about the dispersion of the active compound inside the PVP based microparticles. It can expect that a nanodispersion has been obtained. There are some good reasons to hypothesize this morphology:

- first, it has been demonstrated (Shah et al., 2014) that this is the usual mode of coprecipitation in droplets containing large PVP quantities;
- second, PVP is a powerful crystal growth inhibitor and no traces of crystalline drug have been formed;
- third, the very fast dissolution of coprecipitates is reasonably due to the very fast dissolution of PVP (that is readily soluble in water based solution), the release of small drug nanoparticles and their subsequent fast solubilization.

1) Considering all the experimental evidences collected in this work, it is possible to state that: looking at the experiments performed at different operating pressures, it was observed that, increasing the pressure, the mean diameter of the particles reduced and the PSD became narrower. Indeed, increasing the pressure, the formation of the supercritical mixture solvent/antisolvent is faster and, therefore, the velocity of the dynamic surface tension vanishing increases, leading the precipitation of smaller particles (De Marco and Reverchon, 2011a);
2) looking at the experiments performed at different solute concentrations, it was observed that, increasing the liquid solution concentration, the mean diameter increased and the particle size distribution enlarged. This trend has been frequently observed in SAS experiments and can be explained using the classical theory of crystallization steps (nucleation and growth) or considering an increase of the viscosity of the solution with a consequent increase of jet break-up time, that led to a disequilibrium between the jet break-up time and the dynamic surface tension vanishing time;
3) the drug entrapment efficiency analysis results confirmed the presence of both solutes in the samples; in particular, they show that using the PVP with the lower molecular weight, the drug content with respect to the initial value remained unchanged. However, these data are not sufficient to demonstrate that PVP and drug were

coprecipitated: it is the reason for which dissolution tests were needed;

4) dissolution test results allow to conclude that only in the case of microparticles production the co-precipitation was successful.

V.2.5 Conclusions

SAS process of PVP based solutions demonstrated to be efficient in producing polymer/drug coprecipitation when accurate process conditions are chosen. Indeed, for the first time, well separated microparticles PVP/FA, PVP/BC and PVP/corticosteroid were produced, overcoming the limitations observed in SAS literature. The induced precipitation by microdroplets formation and drying is the key step of the successful coprecipitation of the two solutes and of the increase of drug dissolution rate. Analyses performed on coprecipitates also showed that the formation of composite microparticles protects the active compound from degradation phenomena.

Chapter V

Chapter VI
Processing of water soluble compounds by ELAS process

VI.1 Background

To properly perform the SAS process, two requisites have to be respected: first the solute has to be soluble in the solvent and not soluble in $scCO_2$, second the organic solvent and $scCO_2$ have to be completely miscible at the process conditions; i.e., a supercritical solution has to be formed. Water shows a very limited solubility in CO_2 at ordinary SAS conditions (313–333 K, 10.0–25.0 MPa); in fact, as can be seen in Fig. VI.1, water and carbon dioxide have a very wide miscibility hole, which reduces increasing the temperatures (Takenouchi and Kennedy, 1964). Therefore, the applicability of the SAS technique is restricted to hydrophobic substances.

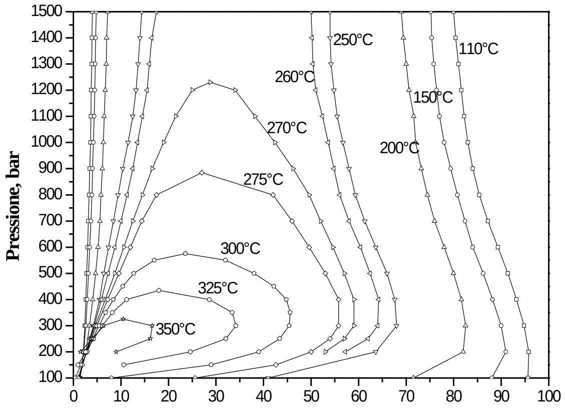

Figure VI.1 *VLE of the binary system CO_2-H_2O (Takenouchi and Kennedy, 1964).*

However, many materials of pharmaceutical interest, like proteins, are water soluble; their use as micronized powders should be of interest in several applications, for example as micro or nanocarriers for the transport of bioactive molecules.

In order to micronize water-soluble compounds, a solution could be the use of another supercritical fluid instead of CO_2 as antisolvent, like ethanol or acetone. However, liquid organic solvents have critical conditions (489 K and 6.14 MPa for ethanol, 508 K and 4.7 MPa for acetone) not compatible with the stability of the large part of the compounds.

A better solution could be the use of an antisolvent formed by a mixture of CO_2 and an organic solvent, like ethanol (EtOH), acetone (Jackson and Mantsch) or isopropyl alcohol (iPrOH), in order to enhance water solubility. However, only some limited studies have been performed in this field till date.

Foster and co-workers (Bustami et al., 2000, Bustami et al., 2003) used mixtures of CO_2 + EtOH (with a mole fraction of EtOH in the antisolvent equal to 0.2) to try to process some proteins, such as lysozyme, albumin, insulin, recombinant human deoxyribonuclease (rhDNase), lysozyme–lactose and rhDNase–lactose. Depending on the protein used, they obtained micrometric (irregular) particles with mean diameters ranging between about 3 and 18 µm. Operating at 15.5 MPa, they analyzed the effect of temperature between 293 and 318 K and the effect of solute in water at concentrations from 5 to 65 mg/mL. However, the obtained powders showed, in many cases, severe problems of aggregation. The less agglomerated particles with a mean diameter equal to 2.9 µm were obtained processing lysozyme at a temperature of 318 K with a concentration of 50 mg/mL.

Jovanović et al. (Jovanović et al., 2004) and Bouchard et al. (Bouchard et al., 2007, Bouchard et al., 2008) also tried to process water soluble compounds using a SAS process based on the use of CO_2 plus EtOH. They worked at extremely low water concentrations (the higher water mole fraction in the ternary mixture was equal to 0.06), that, in turn, implied the possibility to process very low quantities of solubilized compounds. They obtained, operating at 10.0 MPa and in the range 35–313 K, spherical microparticles of lysozyme, glycine and phenylalanine monohydrate with mean diameters falling the in range 1–50 µm.

Supercritical conditions are obtained for all the mixture compositions located on the right side of the MCP; whereas, the part of the phase diagram on the left of the MCP, in which single phase conditions are still obtained, is called expanded liquid region. An expanded liquid, especially in the proximity of the MCP, has characteristics very similar to the ones of the corresponding supercritical fluid mixture and could give precipitation results comparable with those obtained operating at supercritical fluid conditions. Expanded liquid conditions correspond to the possibility to process homogeneous mixtures containing larger mole fractions of water and co- antisolvent, increasing the possible concentration of solute that can be processed, thus overcoming one of the limitations of the works previously discussed. Moreover, this region has never been tested for the precipitation from water solutions by compressed antisolvents.

Recently, De Marco and Reverchon (De Marco and Reverchon, 2012) proposed a new modification of SAS process using CO_2+ ethanol mixtures as antisolvent; but, the operating range of antisolvent composition was extended to expanded liquid conditions and, accordingly, they named this process Expanded Liquid Antisolvent (ELAS) precipitation, since it works in the region in which an expanded liquid mixture is formed.

Ethanol was chosen as co-antisolvent because it is largely soluble in $scCO_2$ and the mixture critical point (MCP) of their binary system is located at 7.9 MPa for a temperature of 313 K (Day et al., 1996); i.e., at SAS process conditions that are very simple to be obtained. Moreover, EtOH is a widely accepted solvent for many applications. The triangular diagram CO_2- H_2O- EtOH is reported in Fig. VI.2 and adapted from Durling et al. (Durling et al., 2007).

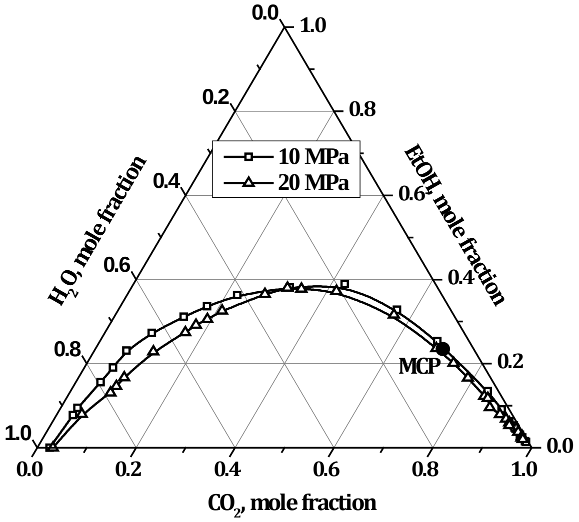

Figure VI.2 *High pressure phase equilibria diagram for the system* CO_2*–EtOH–*H_2O *at 313 K and different pressures (Durling et al., 2007).*

Looking at this diagram, it is possible to see that: (a) the miscibility hole in the ternary system only slightly varies between 100 and 20.0 MPa; therefore, it should be considered as approximately valid also for intermediate pressures; (Liapis and Bruttini) (b) large quantities of water can be used remaining in the single phase (outside the miscibility hole) and it is possible to work in the expanded liquid homogeneous region located on the left of the MCP.

The feasibility of ELAS process was demonstrated processing the bovine serum albumin (BSA) as model compound. Microparticles with narrow particle size distributions and mean diameter in the range 0.5-2 µm and nanoparticles with a mean diameter down to 0.19 µm were obtained.

On the basis of this preliminary study, the aim of this work were:

- to extend the applicability of ELAS to other co-antisolvent (acetone and isopropyl alcohol) to understand if the kind of co-antisolvent can influence morphology and particle size of precipitates;
- to extend the applicability of ELAS to other water soluble compounds of high-added value, such as proteins, enzymes and polymers;
- to understand the precipitation mechanisms involved in ELAS process.

VI.2 Precipitation experiments

Materials

BSA (fraction V, 66 kDa, γ globulin free, purity 99 %), Lysozyme from chicken egg white (lyophilized powder, single-chain mol wt 14.3 kDa), Micrococcus lysodeikticus (lyophilized cells), Sodium alginate (1% viscosity 35 mPa·s; mannuronic acid content 60%), Polyvinyl alcohol (PVA, MW ≈ 30.000–55.000 g/mol), distilled water (H_2O), ethanol (EtOH, purity 99.8 %), acetone (AC, purity 99.5 %) and isopropyl alcohol (iPrOH, purity 99.8 %) were supplied by Sigma–Aldrich (Italy). Carbon dioxide (CO_2 ,purity 99 %) was purchased from SON (Italy). All materials were used as received.

ELAS apparatus

A schematic representation of the apparatus used in this study is reported in Fig.VI.3. The ELAS laboratory apparatus consists of a diaphragm high-pressure pump (Milton Roy, model Milroyal B) used to deliver carbon dioxide, an HPLC pump (Gilson, model 805) used to deliver the co-antisolvent, and a diaphragm high-pressure pump (Milton Roy, mod. Milroyal D), used to deliver the aqueous solution. The pump that delivers CO_2 possesses a cooling head to avoid cavitation. The pre-mixer is a high-pressure vessel with an internal volume of 35 cm^3, loaded with stainless steel perforated saddles, which ensures a large contact surface between co-antisolvent and CO_2. A cylindrical vessel with an internal volume of 500 cm^3 was used as the precipitation chamber. The precipitation chamber was electrically heated using thin band heaters. The pressure in the chamber was measured by a test gauge manometer (Salmoiraghi, model SC-3200) and regulated by a micrometering valve (Hoke, model 1315G4Y) located at the exit (bottom) of the chamber. The aqueous solution was delivered to the precipitator through a thin wall stainless steel nozzle. A second collection chamber located downstream the precipitator, operating at a lower pressure (1.8–2.0 MPa) was used to recover the mixture of water and co-antisolvent. The pressure in this chamber was regulated by a backpressure valve (Tescom, model 26-1723-44). At the exit of the second vessel a rotameter and a dry test meter were used to measure the CO_2 flow rate and the total quantity of CO_2 delivered, respectively. The co-antisolvent was, then, recovered using a rotary evaporator.

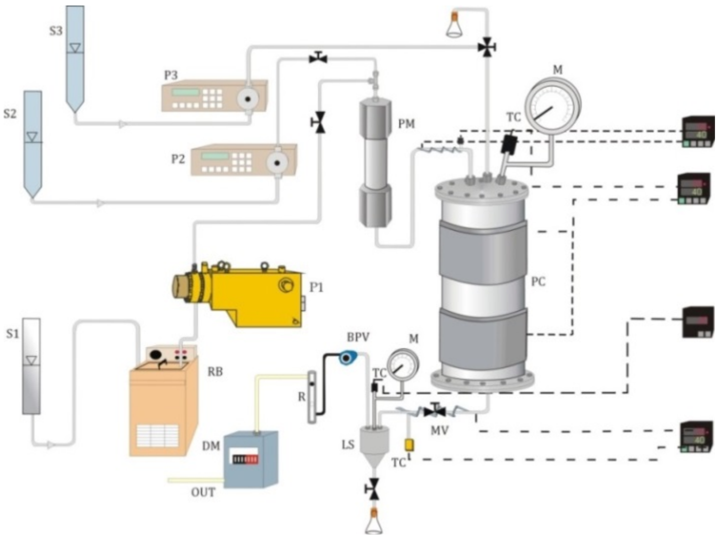

Figure VI.3 *Schematic representation of ELAS apparatus. S1: CO_2 supply; S2: co-antisolvent supply; S3: aqueous solution supply; RB: refrigerating bath; P1, P2, P3: pumps; TC: thermocouple; M: manometer; PM: pre-mixer; PC:*

ELAS procedure

An experiment usually begins delivering supercritical CO_2 at a constant flow rate to the pre-mixer and to the precipitation chamber, until the desired pressure is reached. Then, the co-antisolvent is pumped to the pre-mixer, where it is put in contact with CO_2 forming an expanded liquid solution. Once reached stable flow rates, temperature and pressure conditions in the precipitation chamber, water is sent through the nozzle in the precipitator to obtain steady state composition conditions of the fluid phase during the solute precipitation. Then, the flow of water is stopped and the aqueous solution is delivered through the nozzle at the given flow rate, producing the precipitation of the solute. At the end of the aqueous solution delivery, two washing steps were performed: in the first one, the mixture co-antisolvent + CO_2 continues to flow to wash the chamber to eliminate water residues for a time t_1 and, in the second one, CO_2 alone continues to flow to eliminate co-antisolvent residues for a time t_2. At the end of this second washing step, CO_2 flow is stopped and the precipitator is depressurized down to atmospheric pressure.

VI.2.1 Bovine serum albumin (BSA)

As a first step, BSA was still used as model compound, but the experiments were performed using also acetone and isopropyl alcohol as co-antisolvents.

ELAS operating conditions were chosen on the basis of the previous experiments performed on this protein (Caputo et al., 2012). The effects of the kind and of the mole fraction of co-antisolvent were investigated (Caputo et al., 2012). In Table VI.1, a list of the experiments performed that reports co-antisolvent flow rate ($Q_{co\text{-}ant}$), liquid solution flow rate (Q_{sol}), carbon dioxide, water and co-antisolvent mole fractions (the presence of the solute was neglected in these calculations), morphologies obtained (Morph.), the mean diameter (m.d.) and the standard deviation (s.d.) is reported.

Table VI. 1 *ELAS experiments performed on BSA at 15.0 MPa and 313 K (NP:nanoparticles; SMP: sub-microparticles; MP: microparticles).*

Co-antis.	$Q_{co\text{-}ant}$, mL/min	Q_{sol}, mL/min	x_{CO2}	x_{H2O}	$x_{co\text{-}ant}$	Morph.	m.d., µm	s.d., µm
EtOH	10	1	0.64	0.09	0.27	SMP	0.61	0.22
	15	1	0.57	0.08	0.35	SMP	0.47	0.13
	25	1	0.46	0.06	0.48	NP	0.06	0.01
	25	2	0.43	0.12	0.45	SMP	1.13	0.51
	25	0.5	0.50	0.03	0.47	u.*	-	-
AC	10	1	0.68	0.09	0.23	u.*	-	-
	15	1	0.61	0.06	0.33	MP+EMP	10.65	5.71
	25	1	0.51	0.07	0.42	MP+EMP	9.22	5.17
	25	2	0.47	0.13	0.40	MP+EMP	2.57	1.66

iPrOH	10	1	0.69	0.09	0.22	MP	4.75	2.78
	15	1	0.62	0.08	0.30	MP	4.05	2.92
	25	1	0.51	0.07	0.42	MP	0.93	0.37
	25	2	0.480	0.132	0.388	SMP	0.50	0.34

Ethanol as co-antisolvent

Effect of co-antisolvent mole fraction

The first set of experiments was performed varying the co-antisolvent mole fraction, obtained changing the flow rates of the fluid components in the precipitator. When ethanol flow rates were fixed at 10 and 15 mL/min (corresponding mole fractions of the fluid components were: x_{CO2}= 0.64, x_{EtOH}= 0.27, x_{H2O}=0.09 and x_{CO2}= 0.57, x_{EtOH}= 0.35, x_{H2O}= 0.08), BSA precipitated as well separated sub-microparticles, as it is possible to observe, for example, from the FESEM images reported in Fig. VI.4a and b. When ethanol flow rate was fixed at 25 mL/min, obtaining the following mole fractions: x_{CO2}= 0.46, x_{EtOH}= 0.48, x_{H2O}= 0.06, nanoparticles were produced, as shown in the FESEM image reported in Fig. VI.4c. Their mean diameter was about 60 nm, as indicated in Table VI.1.

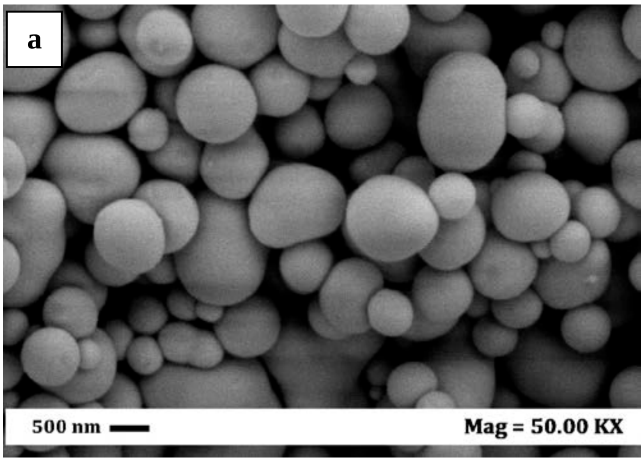

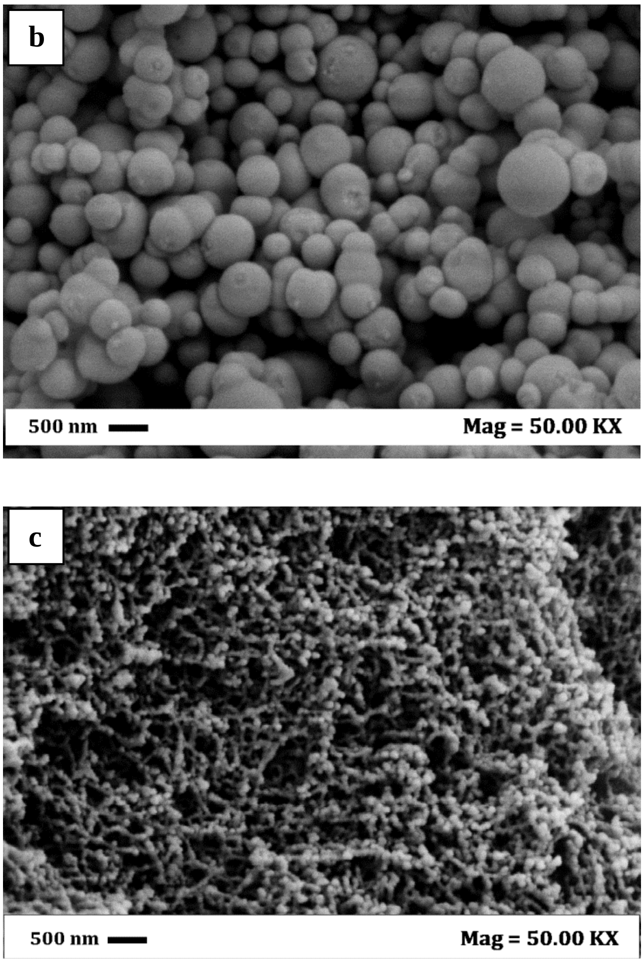

Figure VI. 4 *FESEM images of BSA particles obtained at 15.0 MPa and 313 K using an ethanol flow rate of: (a) 10 mL/min; (b) 15 mL/min; (c) 25 mL/min*.

A comparison among the volumetric cumulative particle size distributions (PSDs) of the BSA particles obtained at the different co-antisolvent flow rates is reported in Fig. VI.5. Increasing the ethanol flow rate that corresponds to an increase of the ethanol mole fraction and to a decrease of the carbon dioxide mole fraction, the mean size of the particles decreases and the PSD becomes narrower; this last information is reported in Table VI.1 in terms of standard deviation (s.d.).

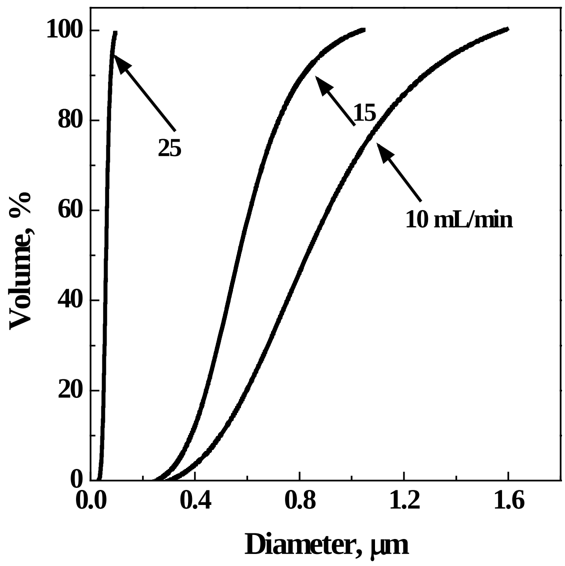

Figure VI.5 *Volumetric cumulative BSA particle size distributions obtained at 15.0 MPa and 313 K at different ethanol flow rates.*

Effect of water mole fraction

To investigate different operating conditions, the co-antisolvent flow rate was fixed at 25 mL/min and water flow rate was varied. Increasing the water flow rate from 1 to 2 mL/min (x_{CO2}= 0.43, x_{EtOH}= 0.45, x_{H2O}= 0.12), BSA precipitated in form of slightly agglomerated sub-microparticles. In this case, the mean particle size was larger than the one obtained at 1 mL/min.

Then, water flow rate was reduced at 0.5 mL/min. In this case, the experiment was not successful, since the water solution flow rate, in combination with the injector diameter and the other process conditions, was not sufficient to allow the liquid jet break-up and the experiment substantially failed.

Acetone as co-antisolvent

Effect of co-antisolvent mole fraction

Using acetone as co-antisolvent, with a flow rate of 10 mL/min, the mole fractions of the fluid components in the precipitator, at the steady state, were: x_{CO2}= 0.68, x_{AC}= 0.23, x_{H2O}= 0.09. At these conditions, BSA was completely extracted by the mixture CO_2+ acetone, and we hypothesized that the operating point lies inside the two-phase region of the high pressure vapor-liquid equilibria (VLE) diagram for the ternary system carbon dioxide–water–acetone.

Using an acetone flow rate of 15 mL/min (x_{CO2}= 0.61, x_{AC}= 0.33, x_{H2O}= 0.06), microparticles and expanded micro-particles were instead obtained, as it is possible to observe from the FESEM image reported in Fig. VI.6a. Increasing the acetone flow rate at 25 mL/min (x_{CO2}= 0.51, x_{AC}= 0.42, x_{H2O}= 0.07), BSA precipitated again in form of microparticles and expanded microparticles, as reported in Fig. VI.6b, where some broken expanded microparticles are clearly visible.

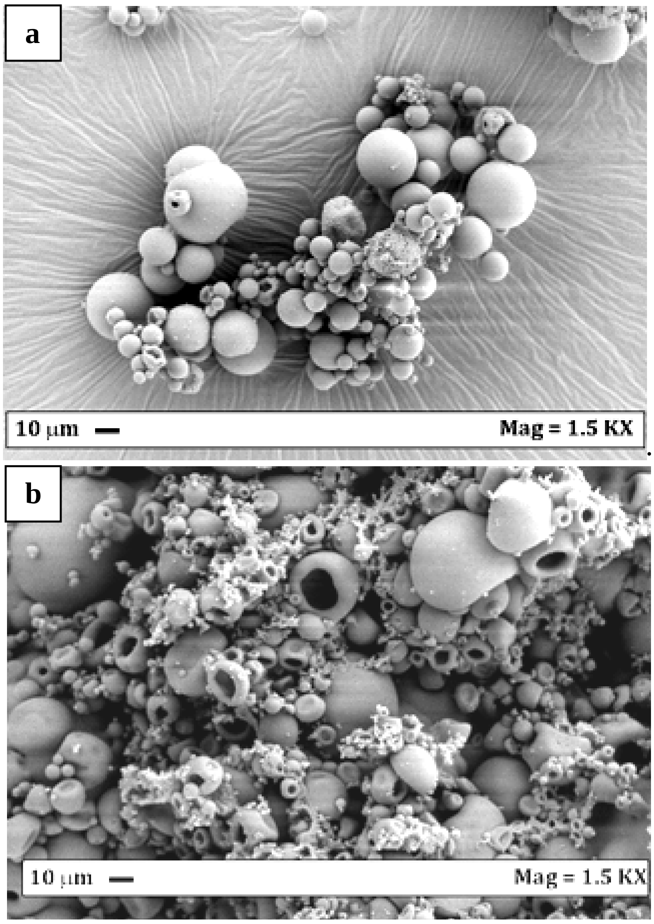

Figure VI.6 *FESEM images of BSA particles obtained at 15.0 MPa and 313 K using an acetone flow rate of: (a) 15 mL/min; (b) 25 mL/min.*

Comparison of the data reported in Table V.3 between the volumetric particle size distribution of the particles obtained at 15 and 25 mL/min shows that the increase of the acetone mole fraction did not generate modifications in the mean particle size and particle size distribution, obtaining similar mean diameters of 10.65 and 9.22 µm, respectively.

Effect of water mole fraction

Once fixed the acetone flow rate at 25 mL/min and increasing the water flow rate from 1 to 2 mL/min (x_{CO2}= 0.47, x_{AC}= 0.40, x_{H2O}= 0.13) microparticles and expanded microparticles, were obtained. Therefore, differently from the case of the BSA powders precipitated using ethanol, in the case of acetone, increasing the water flow rate, the mean particle size decreases to 2.57 µm and the particle size distribution was sharper, as it is possible to observe from the comparison of the volumetric particle size distributions reported in Fig. VI.7.

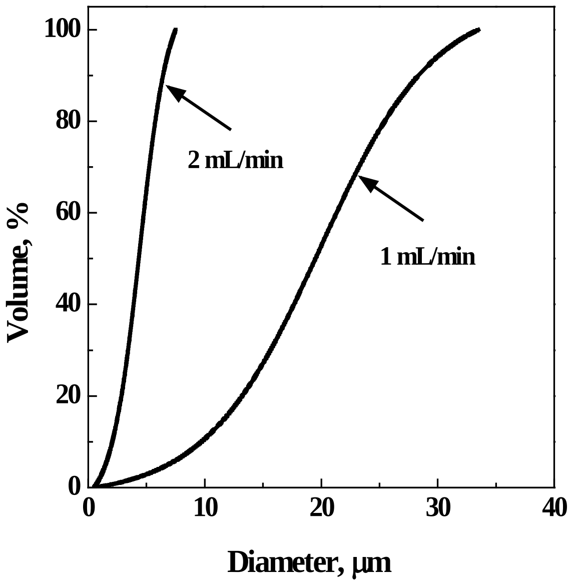

Figure VI.7 *Volumetric cumulative BSA particle size distributions, obtained at 15.0 MPar and 313 K using acetone as co-antisolvent, at different water flow rates.*

Isopropyl alcohol as co-antisolvent

Effect of co-antisolvent mole fraction

In correspondence of an isopropyl alcohol flow rate of 10 mL/min, the mole fractions of the fluid components, at steady state in the precipitator, are: x_{CO2} = 0.69, x_{iPro} = 0.22, x_{H2O} = 0.09. At these conditions, BSA precipitated as microparticles, as it is possible to observe from the FESEM image in Figure VI.8a (with a mean diameter of about 4.75 µm). Increasing the isopropyl alcohol flow rate at 15 mL/min, the mole fractions of the fluid components were: x_{CO2} = 0.62, x_{iPrOH} = 0.30, x_{H2O} = 0.08 and microparticles were obtained, as shown in Figure VI.8b (mean diameter of about 4.05 µm). When it was used an isopropyl alcohol flow rate of 25 mL/min (x_{CO2} = 0.51, x_{iPro} = 0.42, x_{H2O} = 0.07), smaller microparticles, as illustrated in Figure VI.8c (the mean diameter equal to 0.93 µm) were produced.

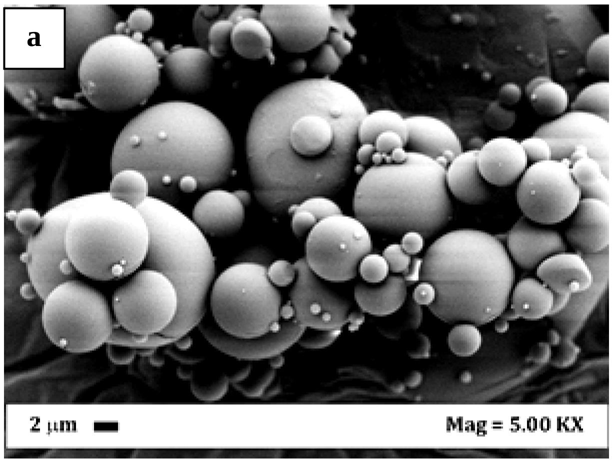

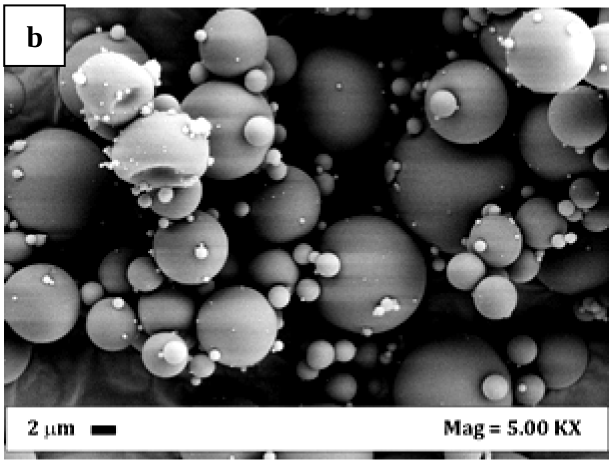

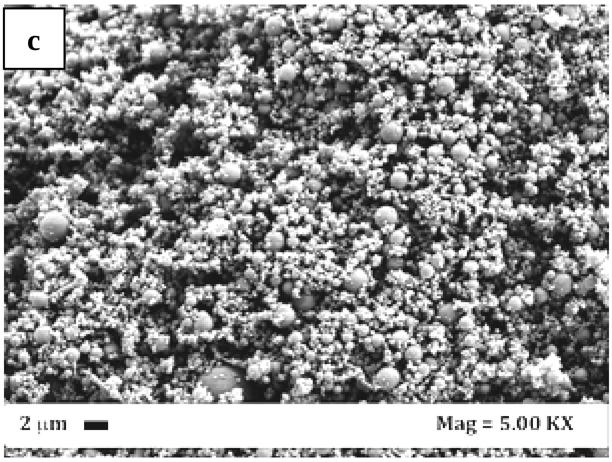

Figure VI. 8 *FESEM images of BSA particles obtained at 15.0 MPa and 313 K using an isopropyl alcohol flow rate of: (a) 10 mL/min; (b) 15 mL/min; (c) 25 mL/min*

The volumetric cumulative particle size distributions at different isopropyl alcohol mole fractions, reported in Figure VI.9, show that the particles produced using this co-antisolvent follow the same trend of ethanol: increasing the co-antisolvent flow rate at 25 mL/min, that means increasing the isopropyl alcohol mole fraction and decreasing the carbon dioxide mole fraction, the mean size decreased and the PSD became narrower. It is possible to note that, in the case of this co-antisolvent, no appreciable variations can be detected for the particles obtained at co-antisolvent flow rates equal to 10 and at 15 mL/min.

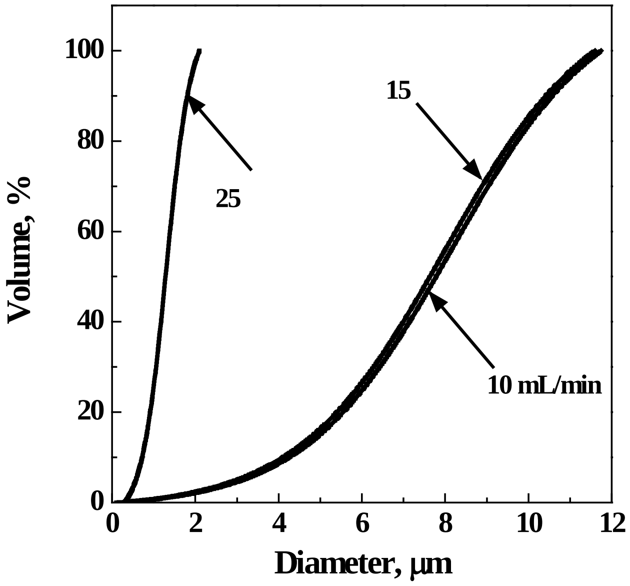

Figure VI.9 *Volumetric cumulative PSDs of the BSA particles obtained at 15.0 MPa and 313 K at different isopropyl alcohol flow rates*

Effect of water mole fraction

Also in the case of isopropyl alcohol, the effect of the water mole fraction, increasing the water flow rate from 1 to 2 mL/min and operating at a 25 mL/min of isopropyl alcohol flow rate was investigated. In this case, the mole fractions were: x_{CO2} = 0.48, x_{iPro} = 0.39, x_{H2O} = 0.13 and microparticles together with short filaments were obtained.

A comparison between the volumetric PSDs obtained varying water flow rate showed that the results are analogous to the ones obtained using acetone: increasing the water flow rate, the mean particle size decreases and the particle size distribution is sharper.

Analyses

XRD analyses of native BSA and of BSA particles obtained using the different co-antisolvents were performed to evaluate if the ELAS process modified the crystallization behavior of the compound. As shown in Figure VI.10, similar broad and scattered pattern for native BSA and all the ELAS processed BSA were observed: all the samples were amorphous.

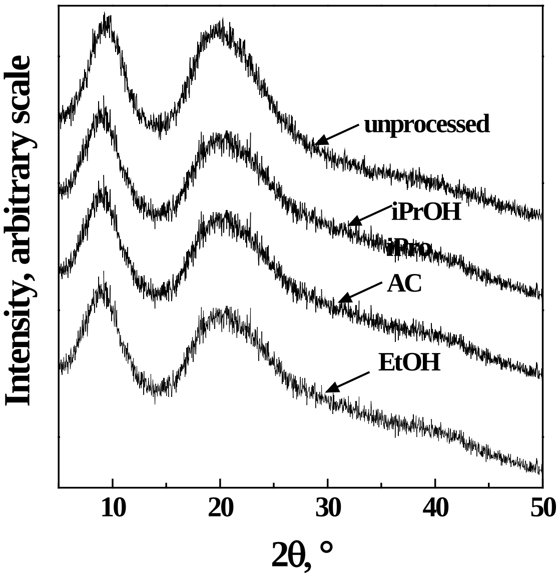

Figure VI.10 *XRD analysis of unprocessed and ELAS processed BSA particles obtained using the different co-antisolvents.*

To study the degradation of the protein, FT-IR spectra of the various BSA powders were analyzed. The spectra in the mid-infrared range of polypeptides are divided in three regions: Amide I (1700–1600 cm^{-1}), Amide II (1600–1500 cm^{-1}) and Amide III (1320–1230 cm^{-1}) (Bummer, 1996). The most sensitive spectral region to the protein secondary structural components is the amide I band (1700–1600 cm^{-1}), which is due almost entirely to the C=O stretching vibrations of different peptide linkages (Chun and Wilkinson, 1999), whereas the Amide II band, that derives mainly from in-plane NH bending and from the CN stretching vibration, is believed to be not very sensitive to the conformation of the protein (Parker, 1983) and the Amide III is approximately an order of magnitude less intense than Amide I. Component bands, in the region of 1650–1658 cm^{-1}, are assigned to α-helix (Bummer, 1996); the infrared spectra related to β-sheet exhibit a low intensity region (1620–1640 cm^{-1}) and a high intensity region (1670–1695 cm^{-1}) (Bummer, 1996). Other possible structures are unordered and β-turns.

The overall FT-IR traces of the native and ELAS processed BSA using the different co-antisolvents are very similar, as reported in Figure VI.11. No differences could be evaluated from these diagrams.

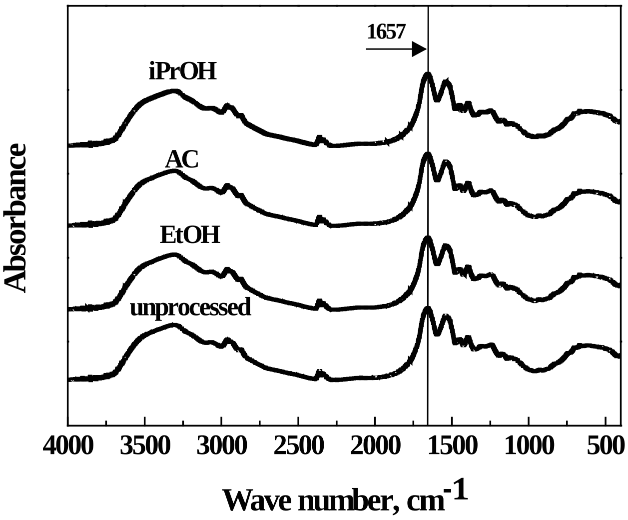

Figure VI.11 *FT-IR traces for unprocessed and ELAS processed BSA particles obtained using the different co-antisolvents.*

Therefore, the second order derivative amide I spectra to enhance the resolution of overlapping IR bands and to identify the secondary structures of the protein (Susi and Michael Byler, 1983) were compared. Considering that α-helix and unordered structures can each be assigned to one band, whereas multiple bands are associated with β-sheets and β-turns (Dong et al., 1990),the relative intensity of the α-helix peaks using also the data from the literature (Peters, 1985) were compared. The analysis revealed an α-helix content, referred to the percentage area of the peak at 1657 cm^{-1}, of about 55% for the BSA particles obtained using acetone as the co-antisolvent, of about 45 % for the particles obtained using isopropanol and of about 40 % for the particles obtained using ethanol. Native BSA showed an α-helix content equal to 55%; this value that is in agreement with the literature data (Peters, 1985). Therefore, the ELAS process has induced minor modifications in the case we used ethanol and isopropyl alcohol. Using acetone as co-antisolvent, no modifications of the BSA secondary structure were found.

HPLC analysis was performed on BSA powders processed using isopropyl alcohol and ethanol as co-antisolvents, to study the extent of the protein degradation. HPLC traces of native BSA, BSA microparticles obtained using isopropyl alcohol and BSA nanoparticles obtained using ethanol showed similar peaks, as shown in Figure VI.12, (the peak was detected at 214 nm in correspondence of 24 min of retention time), but the intensity of the processed BSA peaks with respect to the one detected for the untreated BSA was equal to 90 % in the case of BSA microparticles obtained from isopropyl alcohol and 82 % in the case of BSA nanoparticles obtained from ethanol, indicating a degradation of the protein, that, in every case, is smaller than the degradation obtained in the case of the traditional processing with organic solvents at low temperature (Yoshikawa et al., 2012).

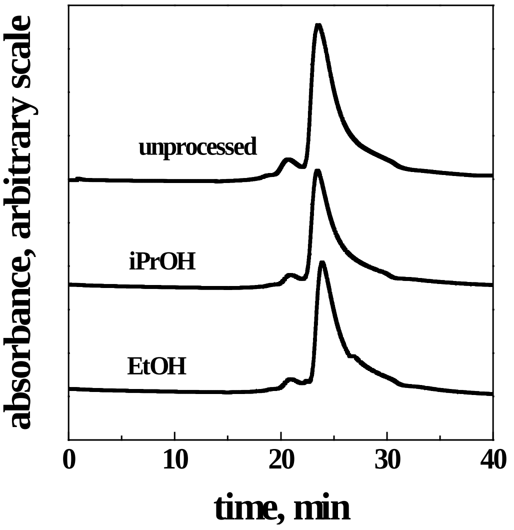

Figure VI.12 *HPLC traces for unprocessed and ELAS processed BSA, using*

The three co-antisolvents belong to class 3 products and, therefore, their FDA limit is 5000 ppm in the final product. A headspace sampler coupled to a gas chromatograph was used to verify the co-antisolvent residue content, in BSA produced particles. The analysis revealed that the solvent residue was around 1000 ppm in the case of acetone, 3000 ppm in the case of ethanol and 1000 in the case of isopropyl alcohol; i.e., in all cases, lower that the FDA limits.

VI.2.2 Lysozyme from chicken egg white

Functional foods are food products enriched with natural additives that can promote consumer’s health and reduce the risk of some diseases (i.e., diabetes, anemia, heart attack) (Menrad, 2003). Their application affects different segments of food market: beverages, cereals, cheese, bakery products and meat (Siró et al., 2008). However, the additive could alter some product characteristics, such as taste, color and texture. To avoid these adverse effects, a possible solution can be to micronize the additive (Weidner, 2009). Moreover, the use of nutrients and supplements at micro and nanoscales can improve their uptake, absorption and bioavailability in the body, compared to bulk equivalents (Chaudhry and Castle, 2011).

Lysozyme is an enzyme widely used as food additive (as E1105) thanks to its numerous properties. In food industry, lysozyme is used as antimicrobial agent to prolong the shelf-life of cheese products, beer and malt beverages, wines and other alcoholic drinks (A. Martín, 2008).However, to avoid that lysozyme could change the taste of foods, it has to be micronized; indeed, it has been observed (Tyle, 1993) that particles smaller than 25 µm are not felt by the palate.

Micronization of lysozyme requires particular care, since proteins undergo to degradation (Manning et al., 1989). Traditional techniques may induce relevant modifications in lysozyme structure with consequent loss of its characteristics (Van der Plancken et al., 2006). Jet milling and ball milling expose the protein to high shear forces and electrostatic charge; moreover, the obtained particles are characterized by a large particle size distribution (Thiering et al., 2000a). In spray drying, the final product yield is generally low and the high temperatures required to evaporate the solvent may cause the denaturation of the protein (Shewan and Stokes, 2013, Yeo et al., 1993). Lyophilisation and liquid antisolvent precipitation show difficulties in solvent recovery and control of particle size distribution (Yeo et al., 1993). Freeze-drying requires long time processing, high consumption of energy and induces partial degradation of the protein due to the stress related to freezing and drying operations (Jovanović et al., 2004). Some authors proposed the micronization of lysozyme by SAS using Dimethylsulfoxide (DMSO) as solvent (Chattopadhyay and Gupta, 2002, Muhrer and Mazzotti, 2003, Thiering et al., 2000a, Thiering et al., 2000b). However, studies about the effect of solvents on proteins structure (Jackson and Mantsch, 1991) showed that DMSO can induce the unfolding of proteins polypeptide chain; in particular, it has been observed (Jackson and Mantsch, 1991) that, in presence of this solvent, lysozyme goes through irreversible denaturation. Some authors (Chattopadhyay and Gupta, 2002, Muhrer and Mazzotti, 2003, Thiering et al., 2000b)measured the residual biological activity of the processed enzyme stating that it ranged between 60 and 100 % of the initial value; but, none verified the presence of structural modifications related to the reduction of α-helix content, which is considered to be responsible for the loss of its properties (Phillips et al., 1994). In order to overcome the limitations of SAS process, some authors tried to micronize proteins using other supercritical fluid based techniques (Adami et al., 2009). The obtained powders were characterized by a good biological activity but they did not produce nanoparticles. Other authors used a modification of SAS in which the antisolvent is formed by a mixture of $scCO_2$ and an organic solvent. Foster and co-workers (Bustami et al., 2000, Bustami et al., 2003) added ethanol or ethanol + triethylamine to $scCO_2$ to micronize different proteins, including lysozyme, obtaining irregular and aggregated particles. Bouchard et al. (Bouchard et al., 2007, Bouchard et al., 2008) added methanol, ethanol, acetone or 2-propanol to $scCO_2$ to process lysozyme; but, they obtained regular particles only using very small quantities of water solutions (the water mole fraction was around 0.006), that imply the possibility to process only very small quantities of solute; moreover, the measure of the solvent residue was not reported.

In order to overtake the limitations of the previously discussed processes, in this work, the micronization of lysozyme using ELAS to obtain precipitates with regular morphology, good biological activity, unaltered conformational structure and negligible solvent residue was proposed. The effects of the kind of co-antisolvent and of the operating parameters on morphology, particle size and particle size distribution are investigated. Various analytical methods are used on the processed powders to verify how ELAS process influences lysozyme integrity.

Experimental results

ELAS experiments were carried out at a pressure of 15.0 MPa, a temperature of 313 K, a CO_2 flow rate of 20 g/min and a liquid solution flow rate of 1 mL/min. The effects of the kind of co-antisolvent, co-antisolvent mole fraction and solute concentration were investigated. In Table VI.2, a selection of the experiments performed, reporting mole fractions, morphologies obtained, mean diameter (m.d.) and standard deviations of lysozyme particles is reported.

Table VI. 2 *Summary of ELAS experiments performed on lysozyme (MP: microparticles; u.*: unsuccessful).*

Co-antis.	**$Q_{co\text{-}ant}$, mL/min**	**C, mg/mL**	x_{CO2}	x_{H2O}	$x_{co\text{-}ant}$	**Morph.**	**m.d., µm**	**s.d., µm**
AC	15	20	0.61	0.06	0.33	u.*	-	-
	25	10	0.51	0.07	0.42	MP	8.67	2.86
		20				MP	11.40	3.31
		50				MP	13.82	6.16
iPrOH	10	20	0.69	0.09	0.22	MP	9.60	2.70
		50				MP	12.36	1.55
	15	20	0.62	0.08	0.30	MP	5.85	1.51
	25	20	0.51	0.07	0.42	MP	2.81	0.83
		50				MP	5.25	1.23

Acetone as co-antisolvent

The first set of experiments was performed using AC as co-antisolvent and fixing the solute concentration at 20 mg/mL. Using AC flow rate of 15 mL/min (x_{CO2} = 0.61, x_{AC} = 0.33, x_{H2O} = 0.06), lysozyme did not precipitated on the porous filter, because probably it is soluble in the mixture $CO_2/H_2O/AC$. When an AC flow rate of 25 mL/min (x_{CO2} = 0.51, x_{AC} = 0.42, x_{H2O} = 0.07) was used, microparticles were obtained. In correspondence of this last process condition, the effect of lysozyme concentration in water (at 10, 20 and 50 mg/mL) was studied.

In Figure VI.13, FESEM images taken at the same enlargement, are reported, showing examples of the morphologies observed at the different concentrations tested; well defined and regular spherical microparticles were produced at all lysozyme concentrations tested. In Figure VI.14, the corresponding particle size distributions are reported, that show that particle size increased with enzyme concentration in the water solution.

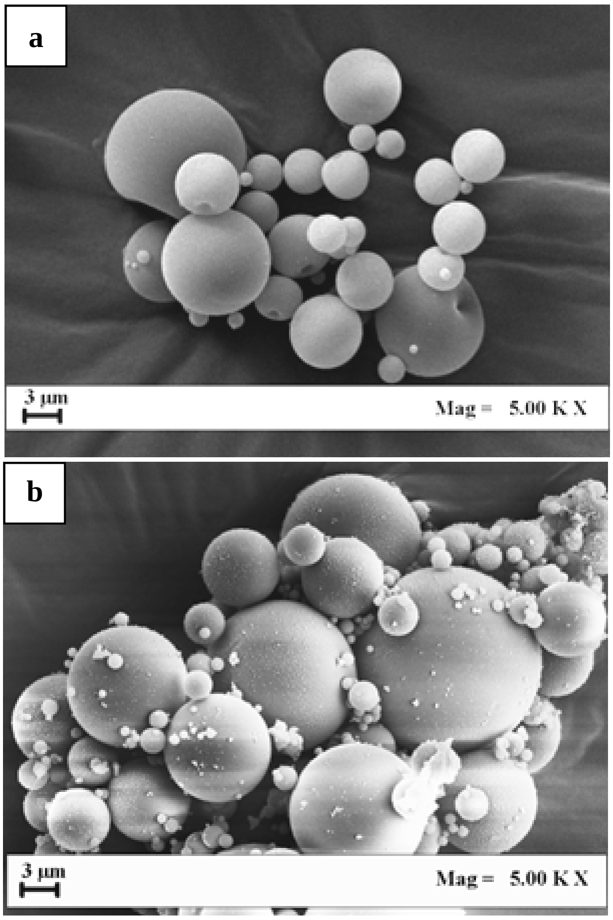

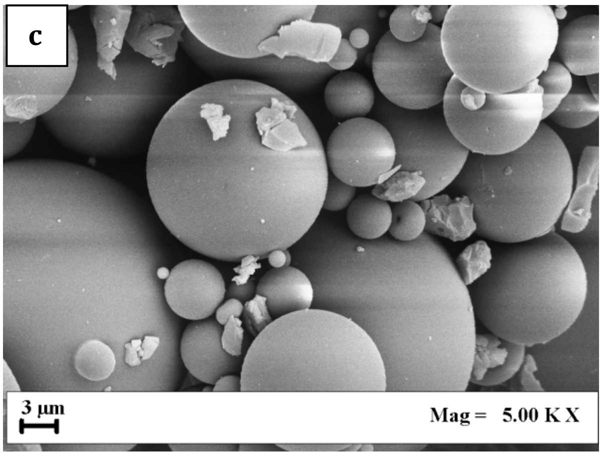

Figure VI.13 *FESEM images of lysozyme particles obtained adding an Acetone flow rate of 25 mL/min to CO_2 and operating at different enzyme concentrations: (a) 10 mg/mL; (b) 20 mg/mL; (c) 50 mg/mL.*

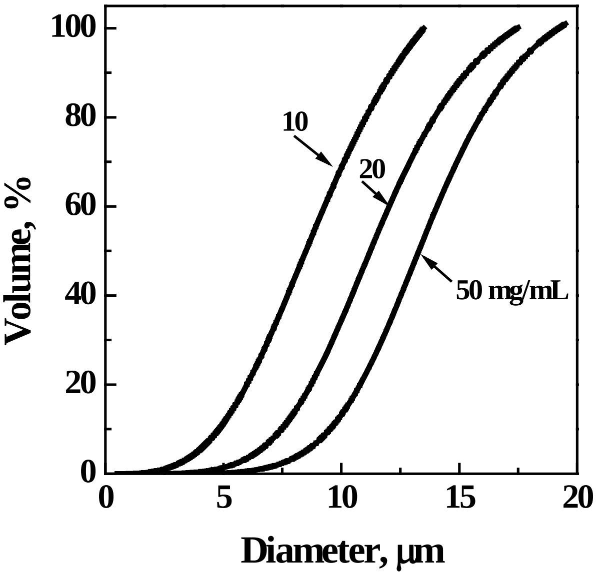

Figure VI.14 *Volumetric cumulative PSDs of lysozyme particles obtained at different lysozyme concentrations in water (10-50 mg/mL) using an Acetone flow rate of 25 mL/min.*

Isopropyl alcohol as co-antisolvent

Using an iPrOH flow rate of 10 mL/min, the mole fractions of the fluid components, at steady state in the precipitator, were: x_{CO2} = 0.69,

x_{iPrOH} = 0.22, x_{H2O} = 0.09. In correspondence of this operating point, lysozyme precipitated in form of microparticles, as it is possible to observe from the FESEM image in Figure VI.15a. Increasing the iPrOH flow rate at 15 mL/min (mole fractions of the fluid components were: x_{CO2} = 0.62, x_{iPrOH} = 0.30, x_{H2O} = 0.08) and at 25 mL/min (x_{CO2} = 0.51, x_{iPrOH} = 0.42, x_{H2O} = 0.07), microparticles were still obtained; but, they were smaller than in the previous experiments, as shown in Figure VI.15b and VI.15c.

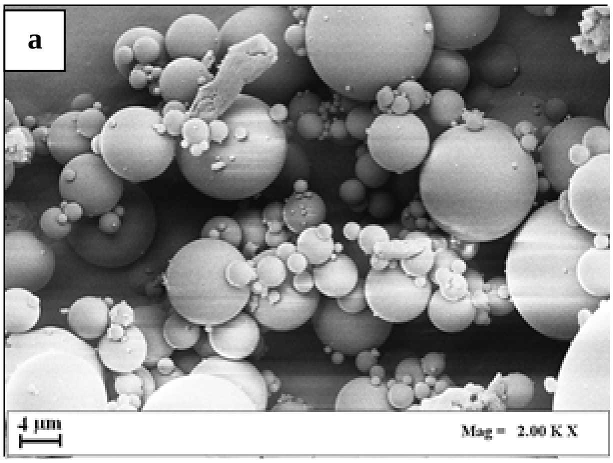

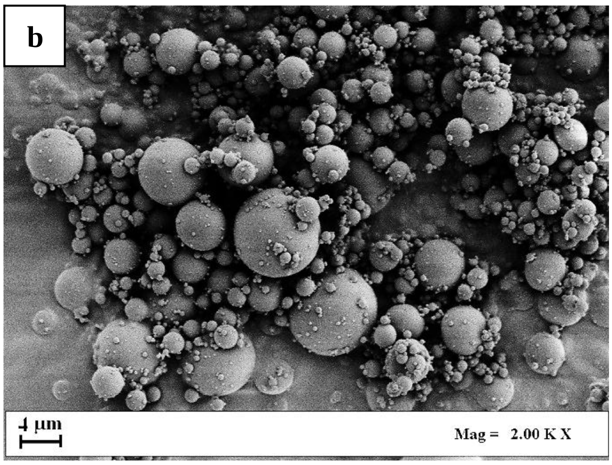

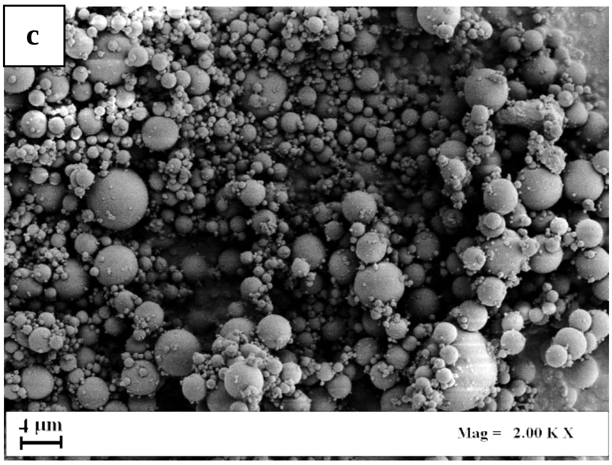

Figure VI.15 *FESEM images of lysozyme microparticles obtained using an Isopropyl alcohol flow rate of: (a) 10 mL/min; (b) 15 mL/min; (c) 25 mL/min.*

The volumetric cumulative lysozyme particle size distributions at different iPrOH flow rates are reported in Figure VI.16, and show that, increasing the co-antisolvent flow rate (that means increasing the iPrOH mole fraction), the mean size of the particles decreases and the PSD become narrower.

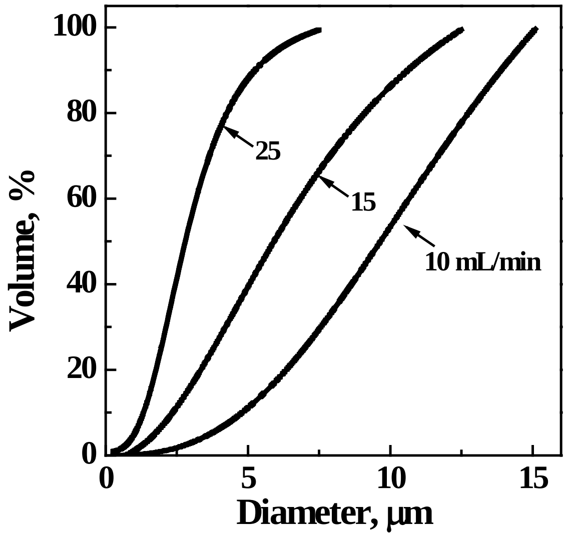

Figure VI. 16 *Volumetric cumulative PSDs of Lysozyme precipitated from water at 20 mg/mL at different Isopropyl alcohol flow rates.*

The effect of lysozyme concentration in water, working in correspondence of the highest and the lowest iPrOH concentrations, corresponding to 10 and 25 mL/min was also studied. In both cases, the experiments performed with a concentration of the liquid solution at 10 mg/mL were unsuccessful, since the material precipitated in form of a compact powder with an irregular shape. Increasing the concentration to 50 mg/mL, well separated microparticles were produced. Comparing the results of the experiments performed at 20 and 50 mg/mL, it is possible to observe that, increasing lysozyme concentration in water, the mean size of the particles increases and PSD enlarges, as it is possible to observe from Figure VI.17, confirming the trend observed when Acetone was used.

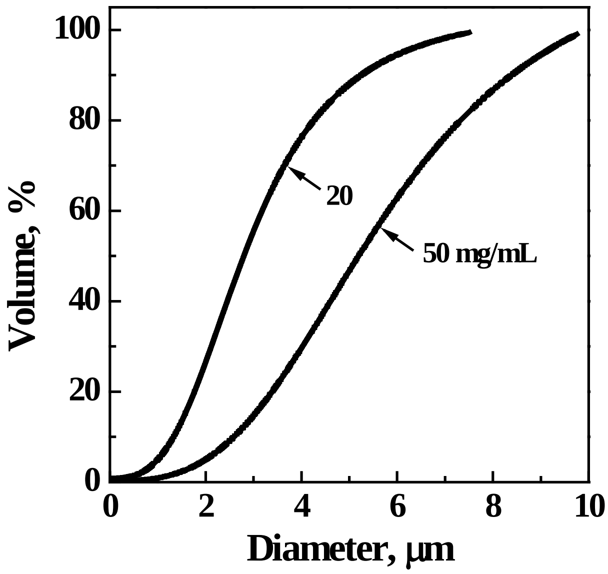

Figure VI.17 *Volumetric cumulative PSDs of Lysozyme particles obtained from water at different concentrations (20-50 mg/mL) using an Isopropyl alcohol flow rate of 25 mL/min.*

Analyses

Native lysozyme and ELAS precipitated lysozyme particles obtained using the different co-antisolvents were analyzed carrying out XRD measurements, to evaluate if the process modified the crystallization of the compound. As shown in Figure VI.18, the samples showed similar broad and scattered pattern, suggesting that no changes occurred in the structure of the protein.

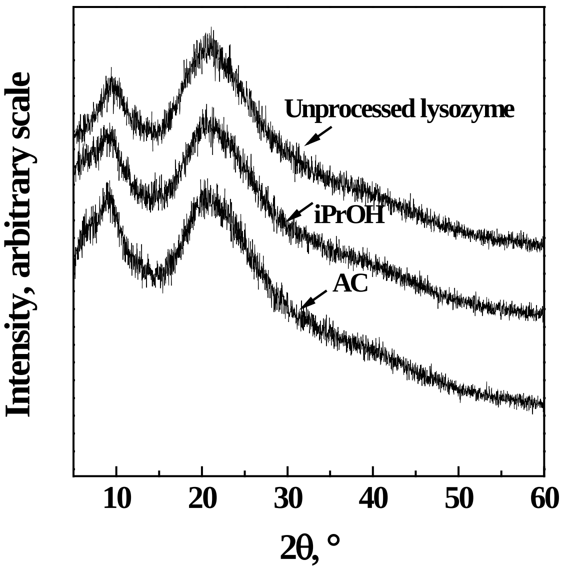

Figure VI.18 *XRD analysis of unprocessed and ELAS processed Lysozyme particles obtained using the different co-antisolvents.*

Lysozyme lytic activity is based on the hydrolysis of the β-(1-4) linkage between N-acetylmuramic acid and N-acetylglucoseamine, which constitutes the peptidoglycan layer of the bacterial cell walls. This chitinolytic activity changes the cell's permeability, causing degradation of the bacterial cell walls, thus accelerating cell lysis (Cunningham et al., 1991). For the determination of lysozyme bioactivity, the degree of lysis induced by the enzyme on *Micrococcus lysodeikticus* by means of turbidimetry was measured (Shugar, 1952). This technique, uses a UV-vis spectrophotometer, and provides a measure of the decrease in turbidity of the suspension that can be correlated to the concentration of biological active enzyme. Then, comparing the difference in absorbance at 450 nm of the substrate suspension after 3 min of the processed and unprocessed lysozyme, it is possible to calculate the residual biological activity (Jiang and Huang, 2007). It resulted that the biological activity of the processed samples with respect to the one of the unprocessed lysozyme was 95 % in the case of AC and 80 % in the case of iPrOH. These results showed that ELAS process, when acetone is used, has a lower impact on the enzymatic activity of lysozyme.

FT-IR analyses were carried out to obtain information about unfolding of the enzyme. As previously discussed, the Amide I region is the most intense absorption band in proteins and it is primarily governed by the stretching vibrations of the C=O of different peptide linkages

(Kong and Yu, 2007). Thus, only this Amide I region was considered. Within this region, the different protein structures are assigned to specific ranges of the infrared spectra: 1650–1658 cm^{-1} for α-helix ; 1620–1640 cm^{-1} and 1670–1695 cm^{-1} for β-sheet; 1640-1648 cm^{-1} for unordered conformation; around 1670, 1683, 1688 and 1694 for β-turns. Since the overall FT-IR traces of native and ELAS processed lysozyme using the different co-antisolvents are very similar, as shown in Figure VI.19, a comparison between the second order derivative amide I spectra to enhance the resolution of overlapping IR bands and to identify the secondary structures of the protein was made (Susi and Michael Byler, 1983).

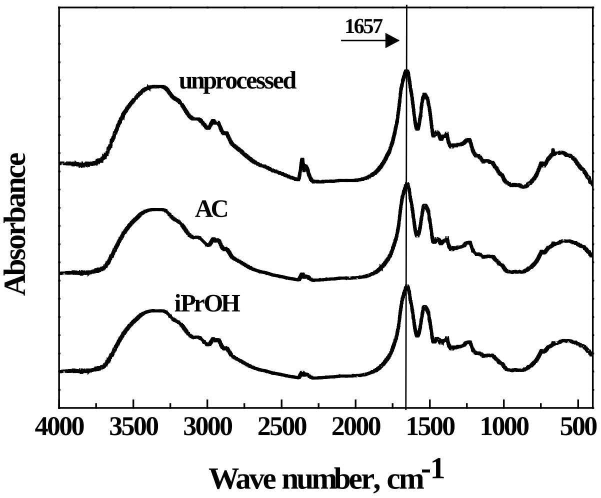

Figure VI.19 *FT-IR traces for unprocessed and ELAS processed Lysozyme particles obtained using the different co-antisolvents.*

It was observed by some authors (Winters et al., 1996) that the loss in activity of lysozyme can be attributed to the structural modification related to the decrease of α-helix content. For this reason, a comparison between the relative intensity of the α-helix peaks for the unprocessed and processed lysozyme was made. FT-IR analysis performed on the native enzyme revealed a α-helix content, referred to the percentage area of the peak at 1657 cm^{-1}, equal to 19%; whereas, the processed powders showed a α-helix content of about 18% for the particles obtained using AC as co-antisolvent and about 16% for the particles produced using Isopropyl alcohol. Therefore, the ELAS process has induced only some minor modifications on lysozyme secondary structure, that are less relevant for the microparticles obtained using AC.

The co-antisolvent residue content was measured using a headspace sampler coupled to a gas chromatograph, to verify if, in lysozyme produced particles, it was lower than the allowable limit, that, in the case of food additives, is equal to 50 ppm, for the two solvents. Before the analysis, the samples were taken under vacuum at 298 K for two hours to eliminate the solvent not entrapped in the powder. The analysis revealed that the solvent residue was around 20 ppm in the case of AC and 30 in the case of iPrOH, therefore, in both the cases, lower that the allowable limits.

VI.2.3 Sodium alginate and polyvinyl alcohol (PVA)

A controlled release system is designed to deliver the drug at a predetermined rate. The drug can be surrounded by a polymeric shell or can be uniformly dispersed in it (Dash and Cudworth Ii, 1998). Morphology, mean size, particle size distribution and polymer molecular weight can influence the ways in which the drug release occurs (Freiberg and Zhu, 2004). The polymer used as carrier has to satisfy some requirements, such as biocompatibility and biodegradability (Rani et al., 2015). Among the natural and synthetic polymers, sodium alginate and polyvinyl alcohol (PVA), have been widely proposed for drug delivery systems (Builders et al., 2008, Kayal and Ramanujan, 2010, More et al., 2010, Tuğcu-Demiröz et al., 2007).

Sodium alginate is a random, linear and anionic polysaccharide, formed by linear copolymers of α-L guluronate (G) and β-D-mannuronate (M) residues. The composition and sequence of G and M can influence polymer properties and depend from the source from which alginate is obtained. Sodium alginate is generally regarded as safe (GRAS) by the FDA (Food and Drug Administration) and is considered as one of the most versatile polysaccharides for a large number of industrial applications. Indeed, it is stable, biodegradable, biocompatible, non-toxic, mucoadhesive, non-immunogenic and low in cost (Motwani et al., 2008). Microparticles of sodium alginate are largely used in biomedical field for drug delivery systems (Goh et al., 2012, Singh et al., 2010, Wong, 2011). Drug release from alginate matrix occurs through two mechanisms: drug diffusion and degradation of the polymer (Goh et al., 2012).

PVA is a water-soluble synthetic polymer, used in pharmaceutical and biomedical applications for its remarkable properties such as mechanical resistance, biocompatibility, biodegradability and non-toxicity (Shagholani et al., 2015). These properties are influenced by polymer molecular weight, cross-linking density and crystallinity (Ting et al., 1992). Furthermore, because of PVA rapid hydrolysis, a long time retention of the carrier in the human body is avoided (Dong et al., 2014).

Traditional techniques used for polymer micronization include solvent/emulsion evaporation (Li et al., 2015a), jet milling (Nykamp et al., 2002) and spray drying (Blanco et al., 2006). However, they show several limitations such as the use of large quantities of organic solvent difficult to recover, high operating temperatures, lack of control over particle size and particle size distribution (Wang et al., 2013).

Generally, sodium alginate microparticles are obtained by gelation methods (Chan et al., 2006, Ribeiro et al., 2005, Silva et al., 2006); however, these techniques led the production of irregular particles and suffer from some operational limits, such as needle blockage and cleaning if the solution is extruded through a needle to form alginate droplets (Paques et al., 2014). Nan et al. (Nan et al., 2014) produced microparticles of alginate using an emulsification + extrusion process, but using this technique long time processing was required; moreover, harmful solvents, such as petroleum ether, were used and no residual solvent analyses were performed on the final product.

Ting et al. (Ting et al., 1992) proposed the micronization of PVA using spray-drying and spray-desolvation techniques; but, they obtained collapsed large particles with a mean diameter in the range 17-55 µm and with yield lower than 50 %; moreover, the characterization of the powder, to verify the structure of the material after processing, was missing.

Microparticles and nanoparticles of different polymers have been frequently obtained using the supercritical antisolvent (SAS) process (E. Reverchon, 2011, De Marco et al., 2013, Adami et al., 2007, Costa et al., 2007, De Marco et al., 2012). For example, PVA, that is soluble in some organic solvents, was precipitated from dimethylsulfoxide (DMSO) using SAS technique (Adami et al., 2007). Well-defined microparticles were obtained, but the residual solvent amount was not measured.

In order to overtake the limitations of the above mentioned processes, in this work the micronization of sodium alginate $(C_6H_7NaO_6)n$ and PVA $(C_2H_4O)n$ is proposed, in order to extend ELAS application to the micronization of these polymers (Prosapio et al., 2016b).

Experimental results

The operating conditions used in the ELAS experiments performed in this work were selected on the basis of our previous experience in this process (Prosapio et al., 2016c, Prosapio et al., 2014). Operating pressure was fixed at 15.0 MPa, temperature at 313 K, aqueous solution flow rate at 1 mL/min and CO_2 flow rate at 20 g/min. The first set of experiments on alginate and PVA were carried out varying the kind of co-antisolvent and its mole fraction. Then, some experiments were performed varying the concentration of the liquid solution. A list of the experiments performed, the obtained morphologies, mean diameter (m.d.) and standard deviation (s.d.) of the powders is reported in Table VI.3.

Table VI. 3 *ELAS experiments performed on sodium alginate and PVA (NP: nanoparticles; MP: microparticles; NMP: Nanostructured microparticles; u.*: unsuccessful; m.d.: mean diameter; s.d.: standard deviation).*

#	Co-antis.	$Q_{co\text{-}ant}$, mL/min	C, mg/mL	Morph.	m.d., µm	s.d., µm
Sodium alginate						
1	EtOH	10	10	NMP	12.98	13.96
2		15		NMP	11.00	5.78
3		25		NMP	10.37	3.22
4	AC	10	10	u.*	-	-
5		15		u.*	-	-
6		25	5	MP	0.91	0.59
7			10	MP	3.35	1.61
8			15	MP	5.40	3.04
9	iPrOH	10	5	MP	2.05	0.49
10			10	MP	6.19	1.75
11			15	MP	12.50	2.81
12		15	10	MP	6.19	1.81
13		25		MP	3.31	1.92
Polyvinyl alcohol (PVA)						
14	EtOH	10	20	MP	2.10	0.64
15		15		NP	0.26	0.08
16		25		NP	0.18	0.05
17	AC	10	20	u.*	-	-
18		15		MP	9.27	2.75
19		25	10	MP	3.58	1.03
20			15	MP	6.54	1.58
21			20	MP	7.76	3.06
22	iPrOH	10	20	MP	3.75	1.08
23		15		MP	2.80	0.95
24		25	10	MP	2.30	0.79
25			20	MP	2.36	0.88

Effect of different co-antisolvents and their mole fraction

Ethanol

Fixing EtOH flow rate at 10 mL/min (the corresponding mole fractions of the fluid components were: x_{CO2} = 0.64, x_{EtOH} = 0.27, x_{H2O} = 0.09), sodium alginate precipitated in form of expanded microparticles with a mean diameter of about 13 µm, characterized by a discontinuous nanostructured surface (also called nanostructured balloons or nanostructured microparticles). A qualitative indication is given in the FESEM image reported in Figure VI.20; quantitative data is reported in Table VI.3. Nanostructure is evident, observing the discontinuous surface of the microparticles reported in Figure VI.20.

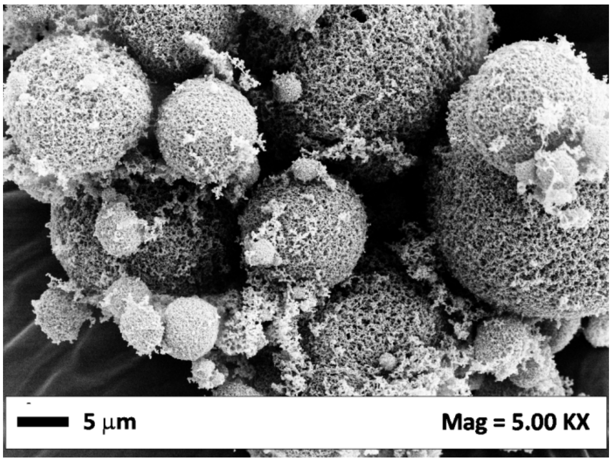

Figure VI.20 *FESEM image of nanostructured SA EMP obtained using an ethanol flow rate of 10 mL/min.*

Other experiments were performed, using EtOH flow rates of 15 mL/min (x_{CO2} = 0.57, x_{EtOH} = 0.35, x_{H2O} = 0.08) and 25 mL/min (x_{CO2} = 0.46, x_{EtOH} = 0.48, x_{H2O} = 0.06), that confirmed the morphology previously observed: nanostructured microparticles were produced also in these cases.

Comparing the particles obtained at different ethanol flow rates, it is possible to observe that, increasing EtOH flow rate, the mean diameter slightly decreased and the standard deviation (that is an indication of the sharpness of the particle size distribution) clearly decreased.

The same experiments were carried out using PVA as solute. When an EtOH flow rate equal to 10 mL/min was used (run #14), PVA precipitated in form of microparticles with a mean diameter of 2.10 µm. Figure VI.21a allows to qualitatively assess the observed morphology and size of microparticles. Increasing the co-antisolvent flow rate at 15 and 25 mL/min, nanoparticles were obtained, as reported in Figure VI.21b, which shows an example of this morphology.

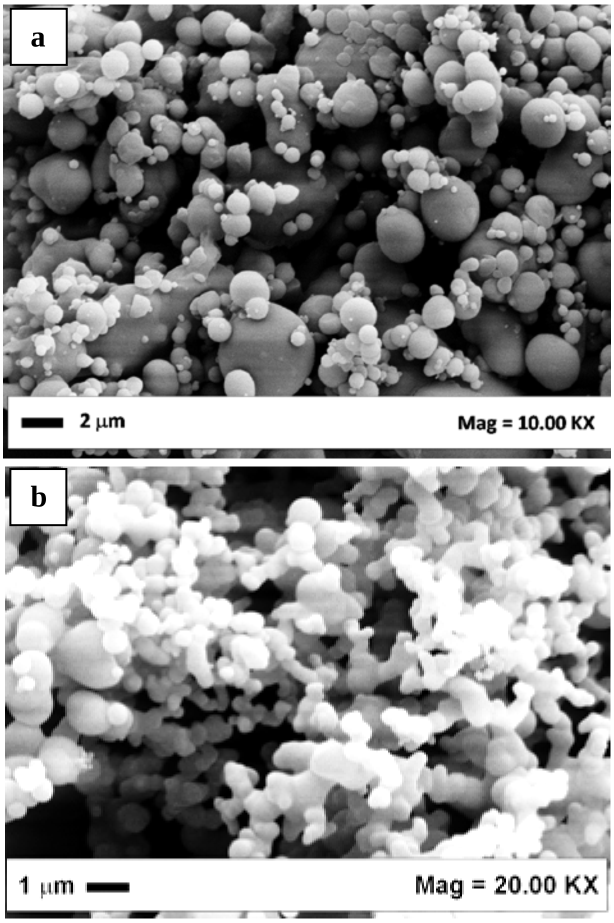

Figure VI.21 *FESEM images of PVA particles precipitated using an ethanol flow rate of: (a) 10 mL/min, (b) 15 mL/min.*

Therefore, SEM images show that, increasing the EtOH flow rate from 10 to 15 mL/min, a change of morphology occurred (microparticles to nanoparticles): the mean size of the particles decreased and the PSD became narrower, as shown in Figure VI.22, where volumetric cumulative particle size distributions are reported. No relevant size variations were observed, changing co-antisolvent flow rate from 15 to 25 mL/min, as it is also possible to verify from data of mean diameter and standard deviation reported in Table VI.3 (experiments # 15 and #16).

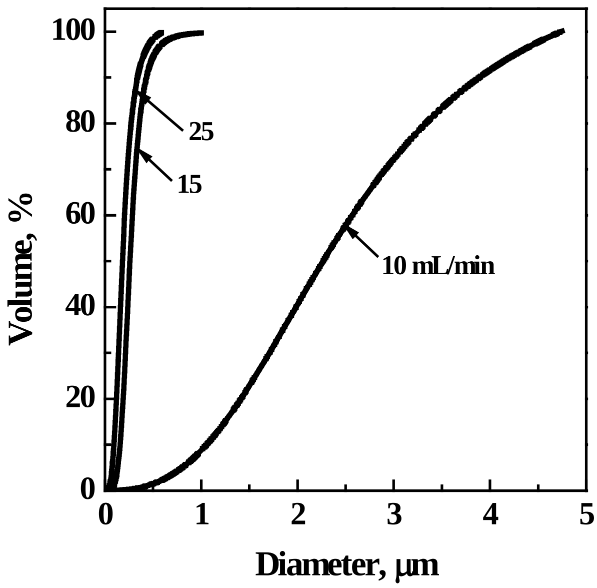

Figure VI.22 *Volumetric cumulative PSDs of PVA particles obtained at different ethanol flow rate.*

Acetone

Acetone was the second solvent used as co-antisolvent in our experiments; when its flow rate was fixed at 10 and 15 mL/min (the corresponding mole fractions of the fluid components were: x_{CO2} = 0.68, x_{AC} = 0.238, x_{H2O} = 0.09 and x_{CO2} = 0.61, x_{AC} = 0.33, x_{H2O} = 0.06 respectively), sodium alginate was completely extracted by the mixture CO_2 + AC; increasing the co-antisolvent flow rate at 25 mL/min (x_{CO2} = 0.51, x_{AC} = 0.42, x_{H2O} = 0.07), microparticles with a rough surface and a broad PSD were obtained, as it is possible to observe in the FESEM image reported in Figure VI.23a.

In the case of PVA, using an AC flow rate of 10 mL/min, as in the case of sodium alginate, the solute was completely extracted by the mixture CO_2 + AC; whereas, in correspondence of AC flow rates of 15 and 25 mL/min, well separated microparticles with a smooth surface were produced, as shown in the FESEM image reported in Figure VI.23b. Comparing the PVA particle size distribution data of the particles obtained at different AC flow rates (Table VI.3), it is possible to observe that, increasing AC mole fraction, the mean diameter of the particles slightly reduced (experiments #18 and #21).

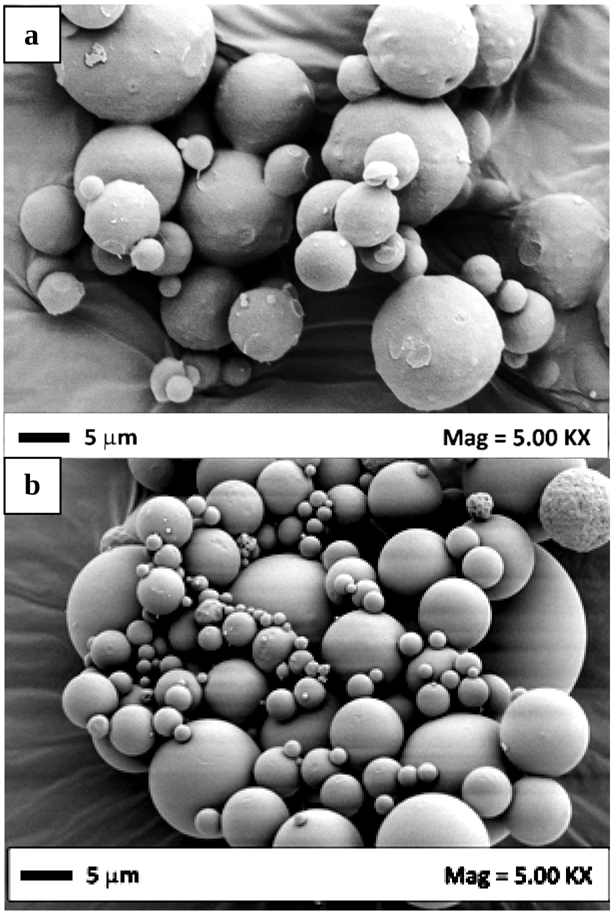

Figure VI.23 *FESEM images of microparticles obtained using an acetone flow rate of 25 mL/min: (a) SA; (b) PVA.*

Isopropyl alcohol

Using iPrOH as co-antisolvent and fixing its flow rate at 10 mL/min (mole fractions of the fluid components are: $x_{CO2} = 0.69$, $x_{iPrOH} = 0.22$, $x_{H2O} = 0.09$), SA precipitated in form of microparticles with a rough surface, as it is possible to observe from the FESEM image in Figure VI.24a. Increasing the iPrOH flow rate at 15 mL/min ($x_{CO2} = 0.62$, $x_{iPrOH} = 0.30$, $x_{H2O} = 0.08$) and 25 mL/min ($x_{CO2} = 0.51$, $x_{iPrOH} = 0.42$, $x_{H2O} = 0.07$), microparticles were still obtained, as shown in Figure VI.24b, where a FESEM image of the particles processed using a iPrOH flow rate equal to 15 mL/min is reported. However, their surface is rough also at these conditions.

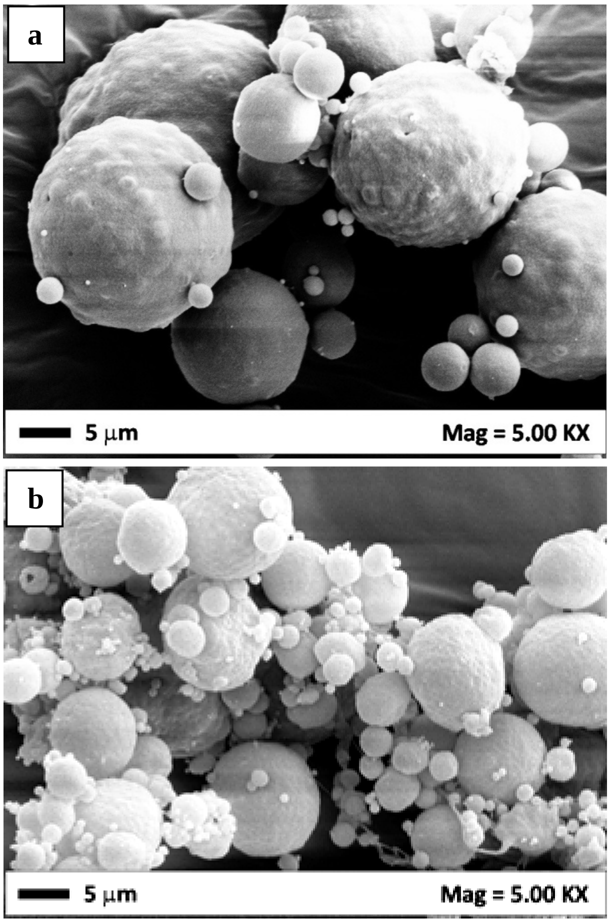

Figure VI.24 *FESEM images of SA particles obtained using an isopropyl alcohol flow rate of: (a) 10 mL/min; (b) 15 mL/min.*

The comparison of the volumetric cumulative particle size distributions, at different iPrOH flow rates, is reported in Figure VI.24 and shows that, increasing the co-antisolvent flow rate, the mean diameter of sodium alginate particles largely reduced and the corresponding PSD became narrower.

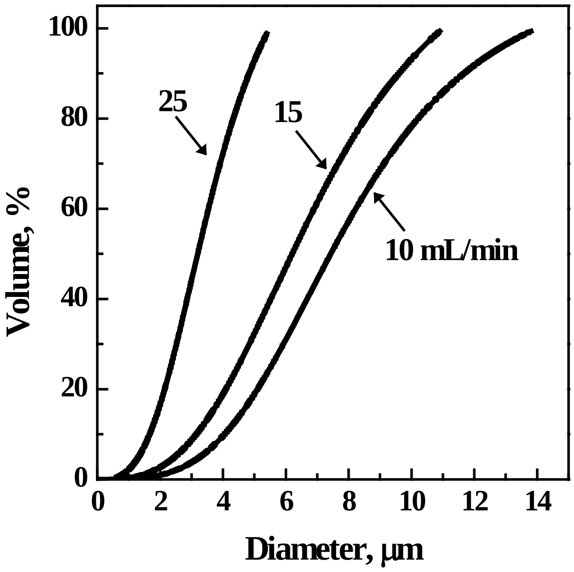

Figure VI.25 *Volumetric cumulative PSDs of sodium alginate particles obtained at different iPrOH flow rates.*

The same experiments were repeated using PVA. In correspondence of all iPrOH flow rates, PVA precipitated in form of well separated spherical microparticles. An example of FESEM image is reported in Figure VI.26.

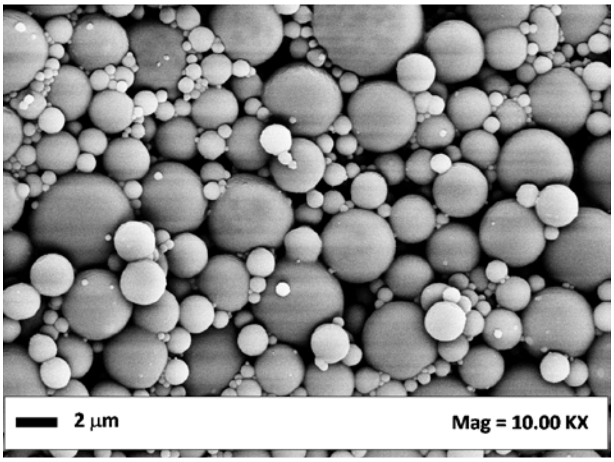

Figure VI.26 *FESEM image of PVA particles obtained using an iPrOH flow rate of 10 mL/min.*

The comparison of the diameters of the obtained PVA particles, reported in Table VI.3 (experiments #22, #23 and #25) shows that the mean size only slightly reduced increasing iPrOH flow rate.

Effect of polymer concentration in the liquid solution

The effect of the concentration of solute in the aqueous solution on particles morphology, mean size and PSD was investigated in correspondence of some selected operating conditions.

Using AC as co-antisolvent at a flow rate equal to 25 mL/min, the concentration of the polymer in water was varied from 5 to 15 mg/mL in the case of sodium alginate and from 10 to 20 mg/mL in the case of PVA. For both the polymers, the comparison of the volumetric particle size distributions obtained at different concentrations (data reported in Table VI.5), shows shat increasing polymer concentration, the mean diameter of the particles increased and the PSD enlarged.

The effect of sodium alginate concentration in water was investigated also using iPrOH as co-antisolvent, using the same set of concentrations of the previous experiments. Comparing the volumetric particle size distributions, shown in Figure VI.27, it is possible to observe that increasing alginate concentration in the liquid solution, the mean diameter largely increased and the particle size distribution enlarged.

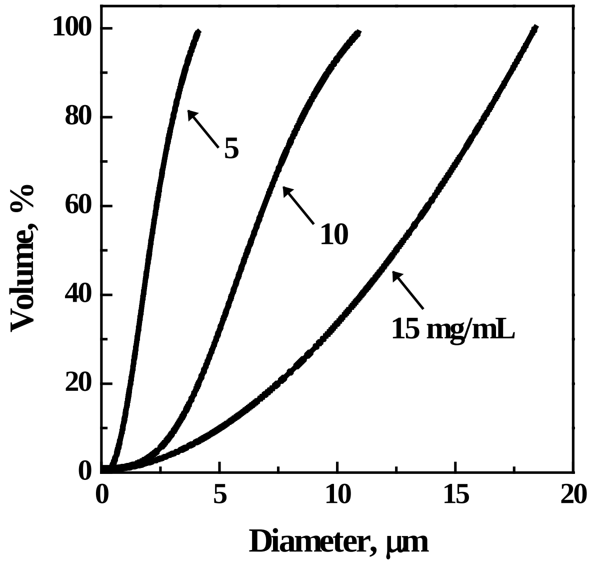

Figure VI.27 *Volumetric cumulative PSDs sodium alginate particles obtained at different concentrations using iPrOH as co-antisolvent.*

Using iPrOH as co-antisolvent with a flow rate equal to 25 mL/min, the effect of solute concentration in water was studied also for PVA. The experiments were performed fixing the concentration of the liquid solution at 10 mg/mL and well separated microparticles were produced. Comparing the mean diameter of these particles with the one of the particles produced at 20 mg/mL, at the same operating conditions, it was found that reducing the concentration, the mean size of the particles and the PSD did not change, as it is possible to observe in Table VI.3 (experiments #24 and #25).

Analyses

XRD analyses for untreated and ELAS processed sodium alginate and PVA were performed to study if the structure of the material was changed by processing. The X-ray diffractograms, in the case of both the polymers and using all the co-antisolvents, show no characteristics peaks; indeed, the traces are very similar to the ones of the unprocessed materials. It means that no chemical changes occurred in the two polymers because of the ELAS processing.

According to Food and Drug Administration (FDA) guidelines, ethanol, acetone and isopropyl alcohol belong to class 3 residual solvent; therefore, their maximum acceptable concentration in the final product is 5000 ppm. A headspace sampler, coupled to a gas chromatograph, was used to verify the co-antisolvent residue content in the ELAS produced particles. The analysis revealed that the solvent residue was for both the polymers around 50 ppm in the case of AC, 300 ppm in the case of EtOH and 200 in the case of iPrOH; i.e., in all cases, lower than the FDA limits.

VI.2.4 Interpretation of results of ELAS experiments

An attempt at the explanation of the observed morphologies during ELAS experiments could start from the consolidated knowledge of the SAS precipitation. Indeed, analogous to SAS, the interpretation of the results obtained in this work could be correlated both to thermodynamic and kinetic aspects of the process.

For the thermodynamic interpretation, the high pressure phase equilibria (VLE) of the ternary systems CO_2/H_2O/co-antisolvent, reported in Figure VI.28, should be taken into account. VLE diagrams, adapted from the scientific literature (Durling et al., 2007, Traub and Stephan, 1990, Chun and Wilkinson, 1999, Bünz et al., 1994), are referred to the same temperature used in ELAS experiments, 313 K, but at different pressures. For the systems CO_2/H_2O/EtOH and CO_2/H_2O/iPrOH, data are available at 10.0 and 20.0 MPa and the experimental points of the miscibility hole (separating the regions in which one or two coexisting phases are present) at different pressures are very close to each other or even overlap. Therefore, in the range 10-20 MPa, the miscibility hole remains substantially unchanged. Consequently, we can assume that the VLE curve at 15 MPa superimposes the literature data too. For the system $CO_2/H_2O/AC$, experimental data are available only at 10 MPa (Figure VI.28b). However, literature reports that for the systems CO_2/H_2O/organic solvents (such as, for example, ethanol (Durling et al., 2007), isopropanol (Chun and Wilkinson, 1999, Bünz et al., 1994) and methanol (Yoon et al., 1993)), in the range 7-30 MPa, increasing the pressure, the biphasic region is not sensibly changed or, at least, it is slightly reduced. Therefore, we can hypothesize that, also for the system $CO_2/H_2O/AC$, an increase of pressure to 15 MPa does not cause a substantial modification of the VLE.

In the diagrams reported in Figure VI.28, it is possible to identify two regions:

(a) an upper region, indicated with I, in which the system is homogeneous; one phase is formed and it is possible to suppose that the solute precipitates from a supercritical or an expanded liquid mixture, depending on the position of the operating point with respect to the mixture critical point;

(Liapis and Bruttini) a lower region, indicated with II, in which two phases in equilibrium coexist and solute can precipitate from the liquid-rich side of the corresponding tie-line. The amplitude of the biphasic region is different for each co-antisolvent and, in particular, it is wider for the system $CO_2/H_2O/AC$.

The operating points, investigated in this work, are indicated with the letters A, B, C; the corresponding mole fractions are shown in Table VI.5.

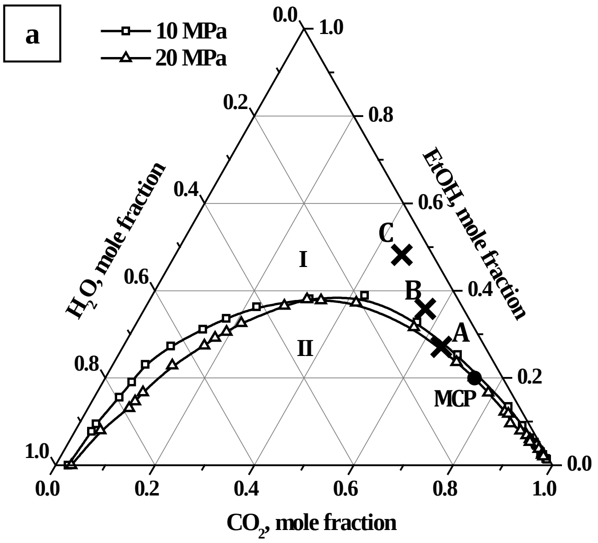
a
10 MPa
20 MPa
0.0
0.2
0.4
0.6
0.8
1.0
1.0
0.8
0.6
0.4
0.2
0.0
H2O, mole fraction
EtOH, mole fraction
CO2, mole fraction
I
II
C
B
A
MCP

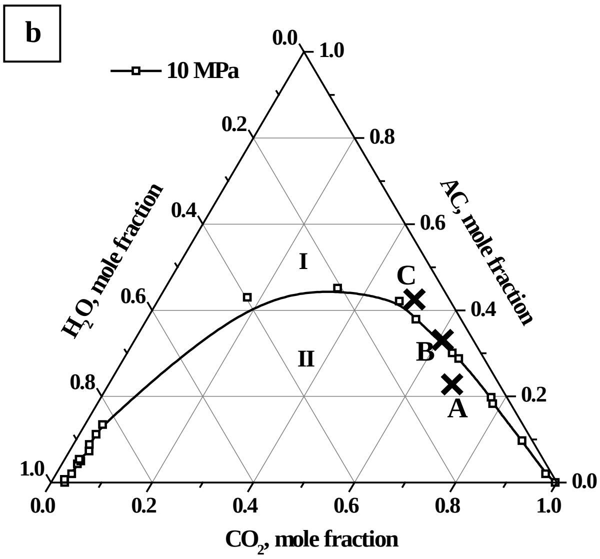
b
10 MPa
0.0
0.2
0.4
0.6
0.8
1.0
1.0
0.8
0.6
0.4
0.2
0.0
H2O, mole fraction
AC, mole fraction
CO2, mole fraction
I
II
C
B
A

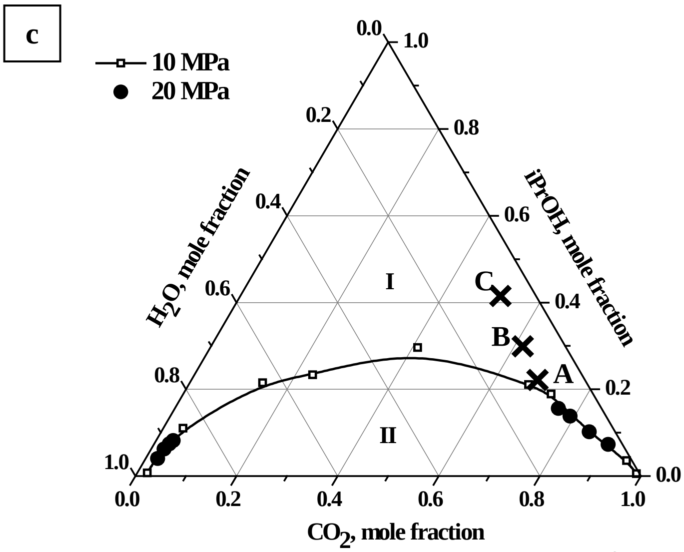

Figure VI.28 *High pressure phase equilibria for the systems* CO_2/H_2O*/co-antisolvent, at 313 K and different pressures, adapted from literature (Durling et al., 2007, Traub and Stephan, 1990, Bünz et al., 1994, Chun and Wilkinson, 1999): a) ethanol; b) acetone; c) isopropyl alcohol. I indicates the homogeneous region, II the two-phase region.*

Depending on the chosen co-antisolvent, different morphologies and mean diameters were obtained that can be related with the position of the operating point with respect to the VLE curve.

- *System* $CO_2/H_2O/EtOH$

In the case of BSA and PVA, looking at the sequence of points A, B, C, in Figure VI.28a, a trend from microparticles to nanoparticles formation can be observed, that seems correlated to the proximity of the operating point with respect to the VLE curve for the system CO_2 - EtOH - H_2O: point A produces microparticles; point B produces sub-microparticles and point C produces nanoparticles. The fact that also nanoparticles were obtained cannot be explained considering only a thermodynamic interpretation. Nanoparticles formation, in the SAS process, is explained considering gas mixing and particles nucleation and growth. Also ELAS process has characteristic times, which competition can explain the attainment of a morphology rather than another one: the time of jet break-up (τ_1) and the time of the surface tension (τ_2) between the solution and the antisolvent gaseous mixture vanishing (in the case of supercritical conditions) or diminishing (in the case of expanded liquid conditions): if $\tau_2 < \tau_1$, gas mixing phenomenon prevails and nanoparticles are obtained from gas-to-particles generation and growth.

In the case of sodium alginate, all the operating points lie in the upper region and led to the formation of nanostructured microparticles, whose formation can be explained in analogy with the SAS proposed mechanisms (Chávez et al., 2003b, Reverchon et al., 2008b). A small nucleation to diffusion time ratio (fast nucleation, slow diffusion) leads to a diffusion limited precipitation front; in this case, as in the SAS process, microparticles formed by nano-elements can be obtained.

- *System $CO_2/H_2O/AC$*

In this case, the miscibility hole is wider with respect to the one of the system $CO_2/H_2O/EtOH$ and the operating point A falls in the biphasic region. Regarding the point B, it lies in the miscibility hole too in the case of lysozyme and sodium alginate and the precipitation was unsuccessful; this experimental evidence can be explained hypothesizing that the presence of these solute induced an enlargement of the miscibility gap. In the case of BSA and PVA, microparticles were obtained, indicating a successful precipitation; this result can be explained, considering that these solutes only slightly modified the VLE and, therefore, the operating point lies in the one-phase region.

Operating at point C, the precipitation of well separated microparticles occurred for PVA, lysozyme and sodium alginate, whereas microparticles and expanded microparticles were obtained in the case of BSA.

- *System $CO_2/H_2O/iPrOH$*

In this case, the miscibility hole is narrower, therefore, the operating points are more distant from the curve.

At all operating points and for all the solutes, microparticles were obtained. Moreover, it was observed that varying iPrOH flow rate, i.e. increasing co-antisolvent mole fraction, the mean size of the particles decreases and the particle size distribution becomes narrower. These experimental evidences can be explained considering that increasing the co-antisolvent mole fraction, the distance of the operating point from the VLE curve increased; correspondingly, the surface tension reduction is faster and the generated droplets are smaller. Consequently, microparticles with smaller diameters were produced.

As concern the effect of solute concentration in water, it was observed that increasing it, the mean size of the obtained particles increased and the PSD enlarged. This result can be explained considering that, increasing the concentration, the cohesive forces increased and also the viscosity of the aqueous solution raised, with the consequent formation of larger droplets during the atomization process; as a consequence, larger particles were produced.

VI.2.5 Conclusions

ELAS process demonstrated to be very efficient in producing typical amorphous particles morphologies. Nanoparticles, microparticles and expanded microparticles of different solutes were obtained, varying the kind of co-antisolvent, the co-antisolvent mole fraction and the solute concentration in water.

Particularly:

- the use of ethanol/carbon dioxide antisolvent mixtures led to the production of micro and nanoparticles with narrow particle size distributions;
- the use of acetone/carbon dioxide and isopropyl alcohol/carbon dioxide as antisolvent mixtures, instead, led mainly to the production of microparticles and expanded microparticles.

The morphology and the dimension of the precipitates can be strictly correlated with the distance of the operating point with respect to the high pressure vapor liquid equilibria curve and to the competition between atomization and gas-mixing.

The analyses confirmed that the obtained particles are characterized by unaltered conformational structure and negligible solvent residue, especially when AC is used as co-antisolvent.

Chapter VII
Conclusions

The study of jet behavior of solvent mixtures, using elastic light scattering and Raman scattering techniques, demonstrated that solvent mixtures, formed by a sharp multi-phase/one-phase mixing transition solvent (like AC) plus a broad multi-phase/one-phase mixing transition solvent (like DMSO), show intermediate behaviors between the two solvents during SAS processing. This evidence was confirmed by precipitation experiments. Indeed, for the first time PVP nanoparticles with a mean diameter down to 0.11 μm and cellulose acetate microparticles with a mean diameter ranging between 0.18 and 0.67 μm were produced using SAS process. Therefore, it is possible to modulate the morphology of SAS precipitates using the appropriate solvent mixture. These results gave a significant contribution on the understanding of the precipitation mechanisms involved in SAS process. This part of the thesis was carried out on in collaboration with the Applied Raman Scattering (ARS) Laboratory of the Erlangen Graduate School of Advanced and Optical Technology (SAOT) of the Friedrich-Alexander-Universität (FAU) Erlangen-Nürnberg.

The coprecipitation experiments performed in this thesis work showed the successful peoduction of well separated microspheres for the systems PVP/folic acid, PVP/β-carotene and PVP/corticosteroids. Moreover, the coprecipitation mechanism was postulated: using PVP as carrier to retard crystal growth and working near above the MCP of the binary system solvent/antisolvent, i.e. when microparticles are produced, coprecipitation is successful because all the content of the droplet concurs to form the final particle. Dissolution tests showed a significant increase of the active compound dissolution rate, that is about 4-5 times faster than the unprocessed drug. This result is very relevant from a pharmaceutical and nutraceutical point of view, since it can open the way to more efficient and focused administration routes for drugs and vitamins.

ELAS experiments performed on BSA, lysozyme, sodium alginate and PVA demonstrated that this technique is very efficient in producing amorphous particles. Nanoparticles, microparticles and expanded microparticles were successfully produced varying the kind of co-antisolvent and the process parameters. In particular, it was found that the use of ethanol/carbon dioxide antisolvent mixtures led to the production of micro and nanoparticles with narrow particle size distributions; the use of acetone/carbon dioxide and isopropyl alcohol/carbon dioxide as antisolvent mixtures, instead, led mainly to the production of microparticles and expanded micro-particles. Moreover, it was hypothesized that the distance of the operating point with respect to the ternary high pressure VLE can condition the morphology of the precipitates: increasing the co-antisolvent mole fraction, this distance increases and the mean size of the particles decreases and the particle size distribution become narrower. The analyses confirmed that the particles are characterized by good biological activity, unaltered conformational structure and negligible solvent residue, especially when AC is used as co-antisolvent. These features make the particles particularly useful for food applications.

References

A. Martín, M. J. C. 2008. Micronization processes with supercritical fluids: Fundamentals and mechanisms. *Advanced Drug Delivery Reviews* 60**,** 339–350.

Adami, R., Osséo, L. S., Huopalahti, R. & Reverchon, E. 2007. Supercritical AntiSolvent micronization of PVA by semi-continuous and batch processing. *The Journal of Supercritical Fluids*, 42**,** 288-298.

Adami, R., Osséo, L. S. & Reverchon, E. 2009. Micronization of lysozyme by supercritical assisted atomization. *Biotechnology and Bioengineering,* 104**,** 1162-1170.

Andreatta, A. E., Florusse, L. J., Bottini, S. B. & Peters, C. J. 2007. Phase equilibria of dimethyl sulfoxide (DMSO) + carbon dioxide, and DMSO + carbon dioxide + water mixtures. *The Journal of Supercritical Fluids,* 42**,** 60-68.

Badens, E., Boutin, O. & Charbit, G. 2005. Laminar jet dispersion and jet atomization in pressurized carbon dioxide. *Journal of Supercritical Fluids,* 36**,** 81-90.

Bellan, J. 2000. Supercritical (and subcritical) fluid behavior and modeling: drops, streams, shear and mixing layers, jets and sprays. *Progress in Energy and Combustion Science,* 26**,** 329-366.

Blanco, M. D., Sastre, R. L., Teijón, C., Olmo, R. & Teijón, J. M. 2006. Degradation behaviour of microspheres prepared by spray-drying poly(d,l-lactide) and poly(d,l-lactide-co-glycolide) polymers. *International Journal of Pharmaceutics,* 326**,** 139-147.

Bouchard, A., Jovanović, N., Jiskoot, W., Mendes, E., Witkamp, G.-J., Crommelin, D. J. A. & Hofland, G. W. 2007. Lysozyme particle formation during supercritical fluid drying: Particle morphology and molecular integrity. *The Journal of Supercritical Fluids,* 40**,** 293-307.

Bouchard, A., Jovanović, N., Martín, Á., Hofland, G. W., Crommelin, D. J. A., Jiskoot, W. & Witkamp, G.-J. 2008. Effect of the modifier on the particle formation and crystallisation behaviour during precipitation from aqueous solutions. *The Journal of Supercritical Fluids,* 44**,** 409-421.

Braeuer, A., Dowy, S. & Leipertz, A. 2010. Simultaneous Raman and elastic light scattering imaging for particle formation investigation. *Optics Letters,* 35**,** 2553-2555.

Braeuer, A., Dowy, S., Torino, E., Rossmann, M., Luther, S. K., Schluecker, E., Leipertz, A. & Reverchon, E. 2011. Analysis of the supercritical antisolvent mechanisms governing particles precipitation and morphology by in situ laser scattering techniques. *Chemical Engineering Journal,* 173**,** 258-266.

Bristow, S., Shekunov, T., Shekunov, B. Y. & York, P. 2001. Analysis of the supersaturation and precipitation process with supercritical CO2. *The Journal of Supercritical Fluids,* 21**,** 257-271.

Builders, P. F., Kunle, O. O., Okpaku, L. C., Builders, M. I., Attama, A. A. & Adikwu, M. U. 2008. Preparation and evaluation of mucinated sodium alginate microparticles for oral delivery of insulin. *European Journal of Pharmaceutics and Biopharmaceutics,* 70**,** 777-783.

Bummer, P. M. 1996. An FTRI study of the structure of human serum albumin adsorbed to polysulfone. *International Journal of Pharmaceutics,* 132**,** 143-151.

Bünz, A. P., Zitko-Stemberger, N. & Dohrn, R. 1994. Phase equilibria of ternary and quaternary systems containing carbon dioxide, water, isopropanol, and glucose. *The Journal of Supercritical Fluids,* 7**,** 43-50.

Bustami, R., Chan, H.-K., Dehghani, F. & Foster, N. 2000. Generation of Micro-Particles of Proteins for Aerosol Delivery Using High Pressure Modified Carbon Dioxide. *Pharmaceutical Research,* 17**,** 1360-1366.

Bustami, R., Chan, H.-K., Sweeney, T., Dehghani, F. & Foster, N. 2003. Generation of Fine Powders of Recombinant Human Deoxyribonuclease Using the Aerosol Solvent Extraction System. *Pharmaceutical Research,* 20**,** 2028-2035.

Campardelli, R., Adami, R., Della Porta, G. & Reverchon, E. 2012. Nanoparticle precipitation by Supercritical Assisted Injection in a Liquid Antisolvent. *Chemical Engineering Journal,* 192**,** 246-251.

Campardelli, R., Baldino, L. & Reverchon, E. 2015. Supercritical fluids applications in nanomedicine. *The Journal of Supercritical Fluids,* 101**,** 193-214.

Caputo, G., Scognamiglio, M. & De Marco, I. 2012. Nimesulide adsorbed on silica aerogel using supercritical carbon dioxide. *Chemical Engineering Research and Design,* 90**,** 1082-1089.

Chan, L. W., Lee, H. Y. & Heng, P. W. S. 2006. Mechanisms of external and internal gelation and their impact on the functions of alginate as a coat and delivery system. *Carbohydrate Polymers,* 63**,** 176-187.

Chattopadhyay, P. & Gupta, R. B. 2002. Protein nanoparticles formation by supercritical antisolvent with enhanced mass transfer. *AIChE Journal,* 48**,** 235-244.

Chaudhry, Q. & Castle, L. 2011. Food applications of nanotechnologies: An overview of opportunities and challenges for developing countries. *Trends in Food Science & Technology,* 22**,** 595-603.

Chávez, F., Debenedetti, P. G., Luo, J. J., Dave, R. N. & Pfeffer, R. 2003a. Estimation of the Characteristic Time Scales in the Supercritical Antisolvent Process. *Industrial & Engineering Chemistry Research,* 42**,** 3156-3162.

Chávez, F., Debenedetti, P. G., Luo, J. J., Dave, R. N. & Pfeffer, R. 2003b. Estimation of the characteristic time scales in the supercritical antisolvent process. *Industrial and Engineering Chemistry Research,* 42**,** 3156-3162.

Chen, A.-Z., Pu, X.-M., Kang, Y.-Q., Liao, L., Yao, Y.-D. & Yin, G.-F. 2006. Preparation of 5-Fluorouracil-Poly(L-lactide) Microparticles Using Solution-Enhanced Dispersion by Supercritical CO2. *Macromolecular Rapid Communications,* 27**,** 1254-1259.

Chen, G.-D., Zhu, Y.-Y., Cao, Y., Liu, J., Shi, W.-Q., Liu, Z.-M. & Chen, Y.-M. 2015a. Association of dietary consumption and serum levels of vitamin A and β-carotene with bone mineral density in Chinese adults. *Bone,* 79**,** 110-115.

Chen, X.-Y., Shang, Y.-L., Li, Y.-H., Wang, J.-X., Maimouna, A. G., Li, Y.-X., Zou, D., Foster, N. R., Yun, J. & Pu, Y. 2015b. Green preparation of uniform prednisolone nanoparticles using subcritical water. *Chemical Engineering Journal,* 263**,** 20-26.

Chun, B.-S. & Wilkinson, G. T. 1999. Ternary phase equilibria of the iso-propanol+water+carbon dioxide system at high pressure. *Korean Journal of Chemical Engineering* 16**,** 187-192.

Costa, M. S., Duarte, A. R. C., Cardoso, M. M. & Duarte, C. M. M. 2007. Supercritical antisolvent precipitation of PHBV microparticles. *International Journal of Pharmaceutics,* 328**,** 72-77.

Cunningham, F. E., Proctor, V. A. & Goetsch, S. J. 1991. Egg-white lysozyme as a food preservative: an overview. *World's Poultry Science Journal,* 47**,** 141-163.

D. Riestenberg, E. C., M. Gborigi, L. Liang, O. R. West, C. Tsouris 2004. Investigation of jet breakup and droplet size distribution of liquid CO2 and water systems—implications for CO2 hydrate formation for ocean carbon sequestration. *American Mineralogist,* 89**,** 1240–1246.

References

Dash, A. & Cudworth Ii, G. 1998. Therapeutic applications of implantable drug delivery systems. *Journal of Pharmacological and Toxicological Methods,* 40**,** 1-12.

Day, C.-Y., Chang, C. J. & Chen, C.-Y. 1996. Phase Equilibrium of Ethanol + CO2 and Acetone + CO2 at Elevated Pressures. *Journal of Chemical & Engineering Data,* 41**,** 839-843.

De Marco, I., Knauer, O., Cice, F., Braeuer, A. & Reverchon, E. 2012. Interactions of phase equilibria, jet fluid dynamics and mass transfer during supercritical antisolvent micronization: The influence of solvents. *Chemical Engineering Journal,* 203**,** 71-80.

De Marco, I., Prosapio, V., Cice, F. & Reverchon, E. 2013. Use of solvent mixtures in supercritical antisolvent process to modify precipitates morphology: Cellulose acetate microparticles. *The Journal of Supercritical Fluids,* 83**,** 153-160.

De Marco, I. & Reverchon, E. 2011a. Influence of pressure, temperature and concentration on the mechanisms of particle precipitation in supercritical antisolvent micronization. *The Journal of Supercritical Fluids,* 58**,** 295-302.

De Marco, I. & Reverchon, E. 2011b. Nanostructured cellulose acetate filaments produced by supercritical antisolvent precipitation. *The Journal of Supercritical Fluids,* 55**,** 1095-1103.

De Marco, I. & Reverchon, E. 2012. Supercritical carbon dioxide + ethanol mixtures for the antisolvent micronization of hydrosoluble materials. *Chemical Engineering Journal,* 187**,** 401-409.

De Marco, I., Rossmann, M., Prosapio, V., Reverchon, E. & Braeuer, A. 2015. Control of particle size, at micrometric and nanometric range, using supercritical antisolvent precipitation from solvent mixtures: Application to PVP. *Chemical Engineering Journal,* 273**,** 344-352.

Debenedetti, P. G. 1990. Homogeneous nucleation in supercritical fluids. *AIChE Journal,* 36**,** 1289-1298.

Decker, M., Schik, A., Meier, U. E. & Stricker, W. 1998. Quantitative Raman imaging investigations of mixing phenomena in high-pressure cryogenic jets. *Applied Optics,* 37**,** 5620-5627.

Defelice, S. L. 1995. The nutraceutical revolution: its impact on food industry R&D. *Trends in Food Science & Technology,* 6**,** 59-61.

Diette, G. B., Dalal, A. A., D’souza, A. O., Lunacsek, O. E. & Nagar, S. P. 2015. Treatment patterns of chronic obstructive pulmonary disease in employed adults in the United States. *International Journal of Chronic Obstructive Pulmonary Disease,* 10**,** 415-422.

Dong, A., Huang, P. & Caughey, W. S. 1990. Protein secondary structures in water from second-derivative amide I infrared spectra. *Biochemistry,* 29**,** 3303-3308.

Dong, Y., Zhou, Z., Ding, H. & Zhang, S. 2014. Preparation and properties of a pH sensitive carrier based on three kinds of polymer blend to control the release of 5-amino salicylic acid. *Pharmaceutical Development and Technology* 19**,** 960-967.

Dowy, S., Braeuer, A., Reinhold-López, K. & Leipertz, A. 2010. In situ optical monitoring of the solution concentration influence on supercritical particle precipitation. *Journal of Supercritical Fluids,* 55**,** 282-291.

Dowy, S., Braeuer, A., Schatz, R., Schluecker, E. & Leipertz, A. 2009. CO2 partial density distribution during high-pressure mixing with ethanol in the supercritical antisolvent process. *The Journal of Supercritical Fluids,* 48**,** 195-202.

Dowy, S., Torino, E., Luther, S. K., Rossmann, M. & Braeuer, A. 2011. Imaging the supersaturation in high-pressure systems for particle generation. *Chemical Engineering Journal,* 168**,** 896-902.

Dukhin, S. S., Shen, Y., Dave, R. & Pfeffer, R. 2005. Droplet mass transfer, intradroplet nucleation and submicron particle production in two-phase flow of solvent-supercritical antisolvent emulsion. *Colloids and Surfaces A: Physicochemical and Engineering Aspects,* 261**,** 163-176.

Dukhin, S. S., Zhu, C., Dave, R., Pfeffer, R., Luo, J. J., Chávez, F. & Shen, Y. 2003. Dynamic interfacial tension near critical point of a solvent-antisolvent mixture and laminar jet stabilization. *Colloids and Surfaces A: Physicochemical and Engineering Aspects,* 229**,** 181-199.

Durling, N. E., Catchpole, O. J., Tallon, S. J. & Grey, J. B. 2007. Measurement and modelling of the ternary phase equilibria for high pressure carbon dioxide–ethanol–water mixtures. *Fluid Phase Equilibria,* 252**,** 103-113.

E. Carretier, E. B., P. Guichardon, O. Boutin, and G. Charbit 2003. Hydrodynamics of Supercritical Antisolvent Precipitation: Characterization and Influence on Particle Morphology. *Industrial & Engineering Chemistry Research,* 42**,** 331-338.

E. Reverchon, I. D. M. 2011. Mechanisms controlling supercritical antisolvent precipitate morphology. *Chemical Engineering Journal,* 169**,** 358–370.

E. Reverchon, I. D. M., R. Adami, G. Caputo 2008. Expanded micro-particles by supercritical antisolvent precipitation: Interpretation of results. *The Journal of Supercritical Fluids* 44**,** 98–108.

Eckhardt, G. & Wagner, W. G. 1966. On the calculation of absolute Raman scattering cross sections from Raman scattering coefficients. *Journal of Molecular Spectroscopy,* 19**,** 407-411.

Elvassore, N., Bertucco, A. & Caliceti, P. 2001. Production of Protein-Loaded Polymeric Microcapsules by Compressed CO2 in a Mixed

Solvent. *Industrial & Engineering Chemistry Research,* 40, 795-800.

Fraile, M., Martín, Ÿ., Deodato, D., Rodriguez-Rojo, S., Nogueira, I. D., Simplício, A. L., Cocero, M. J. & Duarte, C. M. M. 2013. Production of new hybrid systems for drug delivery by PGSS (Particles from Gas Saturated Solutions) process. *The Journal of Supercritical Fluids,* 81, 226-235.

Franceschi, E., De Cesaro, A. M., Feiten, M., Ferreira, S. R. S., Dariva, C., Kunita, M. H., Rubira, A. F., Muniz, E. C., Corazza, M. L. & Oliveira, J. V. 2008. Precipitation of β-carotene and PHBV and co-precipitation from SEDS technique using supercritical CO2. *The Journal of Supercritical Fluids,* 47, 259-269.

Freiberg, S. & Zhu, X. X. 2004. Polymer microspheres for controlled drug release. *International Journal of Pharmaceutics,* 282, 1-18.

Goh, C. H., Heng, P. W. S. & Chan, L. W. 2012. Alginates as a useful natural polymer for microencapsulation and therapeutic applications. *Carbohydrate Polymers,* 88, 1-12.

Gokhale, A., Khusid, B., Dave, R. N. & Pfeffer, R. 2007. Effect of solvent strength and operating pressure on the formation of submicrometer polymer particles in supercritical microjets. *The Journal of Supercritical Fluids,* 43, 341-356.

Gómez-Gaete, C., Tsapis, N., Besnard, M., Bochot, A. & Fattal, E. 2007. Encapsulation of dexamethasone into biodegradable polymeric nanoparticles. *International Journal of Pharmaceutics,* 331, 153-159.

Gu, Y., Zhou, Y., Tang, H., Rothe, E. W. & Reck, G. P. 2000. Pressure dependence of vibrational Raman scattering of narrow-band, 248-nm, laser light by H2, N2, O2, CO2, CH4, C2H6, and C3H8 as high as 97 bar. *Applied Physics B,* 71, 865-871.

Hakuta, Y., Hayashi, H. & Arai, K. 2003. Fine particle formation using supercritical fluids. *Current Opinion in Solid State and Materials Science,* 7, 341-351.

He, W., Suo, Q., Hong, H., Shan, A., Li, C., Huang, Y., Li, Y. & Zhu, M. 2007. Production of natural carotene-dispersed polymer microparticles by SEDS-PA co-precipitation. *Journal of Materials Science,* 42, 3495-3501.

He, Y., Mi, J. & Zhong, C. 2008. Surface Tension and Tolman Length of Spherical Particulate in Contact with Fluid. *The Journal of Physical Chemistry B,* 112, 7251-7256.

Heidebach, T., Först, P. & Kulozik, U. 2010. Influence of casein-based microencapsulation on freeze-drying and storage of probiotic cells. *Journal of Food Engineering,* 98, 309-316.

Hong, H. L., Suo, Q. L., He, W. Z. & Li, C. P. 2007. Formation of Carotene/Proanthocyanidin Composite Microparticles via the

Solution-Enhanced Dispersion by Supercritical Fluids (SEDS) Process through Prefilming Atomization. *Industrial & Engineering Chemistry Research,* 46**,** 6630-6634.

Hosseini, S. M. H., Emam-Djomeh, Z., Sabatino, P. & Van Der Meeren, P. 2015. Nanocomplexes arising from protein-polysaccharide electrostatic interaction as a promising carrier for nutraceutical compounds. *Food Hydrocolloids,* 50**,** 16-26.

Jackson, M. & Mantsch, H. H. 1991. Beware of proteins in DMSO. *Biochimica et Biophysica Acta (BBA) - Protein Structure and Molecular Enzymology,* 1078**,** 231-235.

Jiang, Z.-L. & Huang, G.-X. 2007. Resonance scattering spectra of micrococcus lysodeikticus and its application to assay of lysozyme activity. *Clinica Chimica Acta,* 376**,** 136-141.

Jovanović, N., Bouchard, A., Hofland, G., Witkamp, G.-J., Crommelin, D. A. & Jiskoot, W. 2004. Stabilization of Proteins in Dry Powder Formulations Using Supercritical Fluid Technology. *Pharmaceutical Research,* 21**,** 1955-1969.

Jung, J. & Perrut, M. 2001. Particle design using supercritical fluids: Literature and patent survey. *The Journal of Supercritical Fluids,* 20**,** 179-219.

Kalogiannis, C. G., Michailof, C. M. & Panayiotou, C. G. 2006. Microencapsulation of Amoxicillin in Poly(l-lactic acid) by Supercritical Antisolvent Precipitation. *Industrial & Engineering Chemistry Research,* 45**,** 8738-8743.

Kayal, S. & Ramanujan, R. V. 2010. Doxorubicin loaded PVA coated iron oxide nanoparticles for targeted drug delivery. *Materials Science and Engineering: C,* 30**,** 484-490.

Keijer, J., Bunschoten, A., Palou, A. & Franssen-Van Hal, N. L. W. 2005. Beta-carotene and the application of transcriptomics in risk–benefit evaluation of natural dietary components. *Biochimica et Biophysica Acta (BBA) - Molecular Basis of Disease,* 1740**,** 139-146.

Kong, J. & Yu, S. 2007. Fourier Transform Infrared Spectroscopic Analysis of Protein Secondary Structures. *Acta Biochimica et Biophysica Sinica,* 39**,** 549-559.

Konynenburg, P. H. V. & Scott, R. L. 1980. Critical Lines and Phase Equilibria in Binary Van Der Waals Mixtures. 298**,** 495-540.

Ledet, G. A., Graves, R. A., Glotser, E. Y., Mandal, T. K. & Bostanian, L. A. 2015a. Preparation and in vitro evaluation of hydrophilic fenretinide nanoparticles. *International Journal of Pharmaceutics* 479**,** 329–337.

Ledet, G. A., Graves, R. A., Glotser, E. Y., Mandal, T. K. & Bostanian, L. A. 2015b. Preparation and in vitro evaluation of hydrophilic fenretinide nanoparticles. *International Journal of Pharmaceutics,* 479**,** 329-337.

Lee, D. J., Telo Da Gama, M. M. & Gubbins, K. E. 1985. Adsorption and surface tension reduction at the vapor-liquid interface. *The Journal of Physical Chemistry,* 89**,** 1514-1519.

Lengsfeld, C. S., Delplanque, J. P., Barocas, V. H. & Randolph, T. W. 2000. Mechanism Governing Microparticle Morphology during Precipitation by a Compressed Antisolvent: Atomization vs Nucleation and Growth. *Journal of Physical Chemistry B,* 104**,** 2725-2735.

Li, C., Wang, W., Wang, X., Jiang, H., Zhu, J. & Lin, S. 2015a. Fabrication of porous polymer microspheres by tuning amphiphilicity of the polymer and emulsion–solvent evaporation processing. *European Polymer Journal,* 68**,** 409-418.

Li, W., Liu, G., Li, L., Wu, J., Lü, Y. & Jiang, Y. 2012. Effect of Process Parameters on Co-precipitation of Paclitaxel and Poly(L-lactic Acid) by Supercritical Antisolvent Process. *Chinese Journal of Chemical Engineering,* 20**,** 803-813.

Li, X., Wang, G., Chen, D. & Lu, Y. 2015b. β-Carotene and astaxanthin with human and bovine serum albumins. *Food Chemistry,* 179**,** 213-221.

Liang, R., Huang, Q., Ma, J., Shoemaker, C. F. & Zhong, F. 2013. Effect of relative humidity on the store stability of spray-dried beta-carotene nanoemulsions. *Food Hydrocolloids,* 33**,** 225-233.

Liapis, A. I. & Bruttini, R. 2009. A mathematical model for the spray freeze drying process: The drying of frozen particles in trays and in vials on trays. *International Journal of Heat and Mass Transfer,* 52**,** 100-111.

Lopera, C. S. M., Guzmàn, O. C., Catalano, R. C. & Gallardo, C. C. 2009. Development and characterization of folic acid microparticles formed by spray-drying with gum arabic and maltodextrin. *Vitae,* 16**,** 55-65.

Manning, M., Patel, K. & Borchardt, R. 1989. Stability of Protein Pharmaceuticals. *Pharmaceutical Research,* 6**,** 903-918.

Marra, F., De Marco, I. & Reverchon, E. 2012. Numerical analysis of the characteristic times controlling supercritical antisolvent micronization. *Chemical Engineering Science,* 71**,** 39-45.

Martín, A. & Cocero, M. J. 2008. Micronization processes with supercritical fluids: Fundamentals and mechanisms. *Advanced Drug Delivery Reviews,* 60**,** 339-350.

Martin, L., Liparoti, S., Della Porta, G., Adami, R., Marqués, J. L., Urieta, J. S., Mainar, A. M. & Reverchon, E. 2013. Rotenone coprecipitation with biodegradable polymers by supercritical assisted atomization. *The Journal of Supercritical Fluids,* 81**,** 48-54.

Mayer, W., Telaar, J., Branam, R., Schneider, G. & Hussong, J. 2003. Raman Measurements of Cryogenic Injection at Supercritical Pressure. *Heat and Mass Transfer,* 39**,** 709-719.

Menrad, K. 2003. Market and marketing of functional food in Europe. *Journal of Food Engineering* 56**,** 181–188.

Montes, A., Gordillo, M. D., Pereyra, C. & Martínez De La Ossa, E. J. 2011. Co-precipitation of amoxicillin and ethyl cellulose microparticles by supercritical antisolvent process. *The Journal of Supercritical Fluids,* 60**,** 75-80.

More, S. M., Kulkarni, R. V., Sa, B. & Kayane, N. V. 2010. Glutaraldehyde-crosslinked poly(vinyl alcohol) hydrogel discs for the controlled release of antidiabetic drug. *Journal of Applied Polymer Science,* 116**,** 1732-1738.

Motwani, S. K., Chopra, S., Talegaonkar, S., Kohli, K., Ahmad, F. J. & Khar, R. K. 2008. Chitosan–sodium alginate nanoparticles as submicroscopic reservoirs for ocular delivery: Formulation, optimisation and in vitro characterisation. *European Journal of Pharmaceutics and Biopharmaceutics,* 68**,** 513-525.

Muhrer, G. & Mazzotti, M. 2003. Precipitation of Lysozyme Nanoparticles from Dimethyl Sulfoxide Using Carbon Dioxide as Antisolvent. *Biotechnology Progress,* 19**,** 549-556.

Mukhopadhyay, M. & Dalvi, S. V. 2005. Analysis of supersaturation and nucleation in a moving solution droplet with flowing supercritical carbon dioxide. *Journal of Chemical Technology & Biotechnology,* 80**,** 445-454.

Muñoz-Fernández, S. & Martín-Mola, E. Uveitis. *Best Practice & Research Clinical Rheumatology,* 20**,** 487-505.

Myerson, A. S. 1993. *Handbook of industrial crystallization,* Butterworth-Heinemann.

Nan, F., Wu, J., Qi, F., Liu, Y., Ngai, T. & Ma, G. 2014. Uniform chitosan-coated alginate particles as emulsifiers for preparation of stable Pickering emulsions with stimulus dependence. *Colloids and Surfaces A: Physicochemical and Engineering Aspects,* 456**,** 246-252.

Nerome, H., Machmudah, S., Wahyudiono, Fukuzato, R., Higashiura, T., Youn, Y.-S., Lee, Y.-W. & Goto, M. 2013. Nanoparticle formation of lycopene/β-cyclodextrin inclusion complex using supercritical antisolvent precipitation. *The Journal of Supercritical Fluids,* 83**,** 97-103.

Nihant, N., Grandfils, C., Jérôme, R. & Teyssié, P. 1995. Microencapsulation by coacervation of poly(lactide-co-glycolide)

IV. Effect of the processing parameters on coacervation and encapsulation. *Journal of Controlled Release,* 35**,** 117-125.

Nykamp, G., Carstensen, U. & Müller, B. W. 2002. Jet milling—a new technique for microparticle preparation. *International Journal of Pharmaceutics,* 242**,** 79-86.

O'donnell, P. B. & Mcginity, J. W. 1997. Preparation of microspheres by the solvent evaporation technique. *Advanced Drug Delivery Reviews,* 28**,** 25-42.

Obrzut, D. L., Bell, P. W., Roberts, C. B. & Duke, S. R. 2007. Effect of process conditions on the spray characteristics of a PLA+methylene chloride solution in the supercritical antisolvent precipitation process. *The Journal of Supercritical Fluids,* 42**,** 299-309.

Oth, M. P. & Moës, A. J. 1985. Enhanced in vitro release of indomethacin from non-aqueous suspensions using indomethacin-polyvinylpyrrolidone coprecipitate. *International Journal of Pharmaceutics,* 24**,** 275-286.

Oxley, J. D. 2012. 6 - Coextrusion for food ingredients and nutraceutical encapsulation: principles and technology. *In:* GARTI, N. & MCCLEMENTS, D. J. (eds.) *Encapsulation Technologies and Delivery Systems for Food Ingredients and Nutraceuticals.* Woodhead Publishing.

Paques, J. P., Van Der Linden, E., Van Rijn, C. J. M. & Sagis, L. M. C. 2014. Preparation methods of alginate nanoparticles. *Advances in Colloid and Interface Science,* 209**,** 163-171.

Park, H. J., Kim, M.-S., Lee, S., Kim, J.-S., Woo, J.-S., Park, J.-S. & Hwang, S.-J. 2007. Recrystallization of fluconazole using the supercritical antisolvent (SAS) process. *International Journal of Pharmaceutics,* 328**,** 152-160.

Parker, F. 1983. *Application of Infrared Spectroscopy in Biochemistry, Biology and Medicine,* Springer Science & Business Media.

Patomchaiviwat, V., Paeratakul, O. & Kulvanich, P. 2008. Formation of Inhalable Rifampicin–Poly(l-lactide) Microparticles by Supercritical Anti-solvent Process. *AAPS PharmSciTech,* 9**,** 1119-1129.

Pérez-Masiá, R., López-Nicolás, R., Periago, M. J., Ros, G., Lagaron, J. M. & López-Rubio, A. 2015. Encapsulation of folic acid in food hydrocolloids through nanospray drying and electrospraying for nutraceutical applications. *Food Chemistry,* 168**,** 124–133.

Peters, T. J. 1985. Serum albumin. *Advanced Protein Chemistry*

Phillips, L. G., Whitehead, D. M. & Kinsella, J. 1994. CHAPTER 2 - Protein Stability. *In:* KINSELLA, L. G. P. M. W. (ed.) *Structure–Function Properties of Food Proteins.* Boston: Academic Press.

Prasertmanakit, S., Praphairaksit, N., Chiangthong, W. & Muangsin, N. 2009. Ethyl Cellulose Microcapsules for Protecting and Controlled Release of Folic Acid. *AAPS PharmSciTech,* 10**,** 1104-1112.

Priamo, W. L., De Cezaro, A. M., Ferreira, S. R. S. & Oliveira, J. V. 2010. Precipitation and encapsulation of β-carotene in PHBV using carbon dioxide as anti-solvent. *The Journal of Supercritical Fluids,* 54**,** 103-109.

Prosapio, V., De Marco, I. & Reverchon, E. 2016a. PVP/corticosteroid microspheres produced by supercritical antisolvent coprecipitation. *Chemical Engineering Journal,* 292**,** 264-275.

Prosapio, V., De Marco, I., Scognamiglio, M. & Reverchon, E. 2015. Folic acid-PVP nanostructured composite microparticles by supercritical antisolvent precipitation. *Chemical Engineering Journal,* 277**,** 286-294.

Prosapio, V., Reverchon, E. & De Marco, I. 2014. Antisolvent micronization of BSA using supercritical mixtures carbon dioxide + organic solvent. *Journal of Supercritical Fluids,* 94**,** 189-197.

Prosapio, V., Reverchon, E. & De Marco, I. 2016b. Polymers' ultrafine particles for drug delivery systems precipitated by supercritical carbon dioxide + organic solvent mixtures. *Powder Technology,* 292**,** 140-148.

Prosapio, V., Reverchon, E. & De Marco, I. 2016c. Production of lysozyme microparticles to be used in functional foods, using an expanded liquid antisolvent process. *The Journal of Supercritical Fluids,* 107**,** 106-113.

Rani, R., Dilbaghi, N., Dhingra, D. & Kumar, S. 2015. Optimization and evaluation of bioactive drug-loaded polymeric nanoparticles for drug delivery. *International Journal of Biological Macromolecules,* 78**,** 173-179.

Rasenack, N., Steckel, H. & Müller, B. W. 2003. Micronization of anti-inflammatory drugs for pulmonary delivery by a controlled crystallization process. *Journal of Pharmaceutical Sciences,* 92**,** 35-44.

Reverchon, E. & Adami, R. 2006. Nanomaterials and supercritical fluids. *The Journal of Supercritical Fluids,* 37**,** 1-22.

Reverchon, E., Adami, R., Caputo, G. & De Marco, I. 2008a. Spherical microparticles production by supercritical antisolvent precipitation: Interpretation of results. *The Journal of Supercritical Fluids,* 47**,** 70-84.

Reverchon, E. & De Marco, I. 2004. Supercritical antisolvent micronization of Cefonicid: thermodynamic interpretation of results. *The Journal of Supercritical Fluids,* 31**,** 207-215.

Reverchon, E., De Marco, I., Adami, R. & Caputo, G. 2008b. Expanded micro-particles by supercritical antisolvent precipitation:

Interpretation of results. *The Journal of Supercritical Fluids,* 44**,** 98-108.

Reverchon, E., De Marco, I. & Torino, E. 2007. Nanoparticles production by supercritical antisolvent precipitation: A general interpretation. *The Journal of Supercritical Fluids,* 43**,** 126-138.

Reverchon, E., Torino, E., Dowy, S., Braeuer, A. & Leipertz, A. 2010. Interactions of phase equilibria, jet fluid dynamics and mass transfer during supercritical antisolvent micronization. *Chemical Engineering Journal,* 156**,** 446-458.

Ribeiro, A. J., Silva, C., Ferreira, D. & Veiga, F. 2005. Chitosan-reinforced alginate microspheres obtained through the emulsification/internal gelation technique. *European Journal of Pharmaceutical Sciences,* 25**,** 31-40.

Riestenberg, D., Chiu, E., Gborigi, M., Liang, L., West, O. R. & Tsouris, C. 2004. Investigation of jet breakup and droplet size distribution of liquid CO2 and water systems—implications for CO2 hydrate formation for ocean carbon sequestration. *American Mineralogist,* 89**,** 1240-1246.

RodríGuez, M., Vila-Jato, J. L. & Torres, D. 1998. Design of a new multiparticulate system for potential site-specific and controlled drug delivery to the colonic region. *Journal of Controlled Release,* 55**,** 67-77.

Rossmann, M. 2015. *Tailor Made Functional Particles by means of Supercritical Antisolvent (SAS) Processing.* Dr.-Ing., Friedrich-Alexander-Universität Erlangen-Nürnberg.

Rossmann, M., Braeuer, A., Dowy, S., Gallinger, T. G., Leipertz, A. & Schluecker, E. 2012. Solute solubility as criterion for the appearance of amorphous particle precipitation or crystallization in the supercritical antisolvent (SAS) process. *The Journal of Supercritical Fluids,* 66**,** 350-358.

Rossmann, M., Braeuer, A. & Schluecker, E. 2014. Supercritical antisolvent micronization of PVP and ibuprofen sodium towards tailored solid dispersions. *The Journal of Supercritical Fluids,* 89**,** 16-27.

Sarkari, M., Darrat, I. & Knutson, B. L. 2000. Generation of microparticles using CO2 and CO2-philic antisolvents. *AIChE Journal,* 46**,** 1850-1859.

Shagholani, H., Ghoreishi, S. M. & Mousazadeh, M. 2015. Improvement of interaction between PVA and chitosan via magnetite nanoparticles for drug delivery application. *International Journal of Biological Macromolecules,* 78**,** 130-136.

Shah, N., Sandhu, H., Choi, D. S., Chokshi, H. & Malik, A. W. 2014. *Amorphous Solid Dispersions: Theory and Practice,* Springer.

Shariati, A. & Peters, C. J. 2003. Recent developments in particle design using supercritical fluids. *Current Opinion in Solid State and Materials Science,* 7**,** 371-383.

Shewan, H. M. & Stokes, J. R. 2013. Review of techniques to manufacture micro-hydrogel particles for the food industry and their applications. *Journal of Food Engineering,* 119**,** 781-792.

Shoyele, S. A. & Cawthorne, S. 2006. Particle engineering techniques for inhaled biopharmaceuticals. *Advanced Drug Delivery Reviews,* 58**,** 1009-1029.

Shugar, D. 1952. The measurement of lysozyme activity and the ultra-violet inactivation of lysozyme. *Biochimica et Biophysica Acta,* 8**,** 302-309.

Silva, C. M., Ribeiro, A. J., Figueiredo, I. V., Gonçalves, A. R. & Veiga, F. 2006. Alginate microspheres prepared by internal gelation: Development and effect on insulin stability. *International Journal of Pharmaceutics,* 311**,** 1-10.

Singh, B., Sharma, V. & Chauhan, D. 2010. Gastroretentive floating sterculia–alginate beads for use in antiulcer drug delivery. *Chemical Engineering Research and Design,* 88**,** 997-1012.

Siró, I., Kápolna, E., Kápolna, B. & Lugasi, A. 2008. Functional food. Product development, marketing and consumer acceptance—A review. *Appetite,* 51**,** 456-467.

Stahl, W. & Sies, H. 2003. Antioxidant activity of carotenoids. *Molecular Aspects of Medicine,* 24**,** 345-351.

Steckel, H., Thies, J. & Müller, B. W. 1997. Micronizing of steroids for pulmonary delivery by supercritical carbon dioxide. *International Journal of Pharmaceutics,* 152**,** 99-110.

Sun, Y., Zhu, L., Wu, T., Cai, T., Gunn, E. M. & Yu, L. 2012. Stability of Amorphous Pharmaceutical Solids: Crystal Growth Mechanisms and Effect of Polymer Additives. *The AAPS Journal,* 14**,** 380-388.

Susi, H. & Michael Byler, D. 1983. Protein structure by Fourier transform infrared spectroscopy: Second derivative spectra. *Biochemical and Biophysical Research Communications,* 115**,** 391-397.

Tabernero, A., Martín Del Valle, E. M. & Galán, M. A. 2012. Supercritical fluids for pharmaceutical particle engineering: Methods, basic fundamentals and modelling. *Chemical Engineering and Processing: Process Intensification,* 60**,** 9-25.

Tajber, L., Corrigan, D. O., Corrigan, O. I. & Healy, A. M. 2009. Spray drying of budesonide, formoterol fumarate and their composites—I. Physicochemical characterisation. *International Journal of Pharmaceutics,* 367**,** 79-85.

Takenouchi, S. & Kennedy, G. C. 1964. *The binary system H2O-CO2 at high temperatures and pressures.*

Teipel, U. 2006. *Energetic materials: Particle processing and characterization*, John Wiley & Sons.

Thiering, R., Dehghani, F., Dillow, A. & Foster, N. R. 2000a. The influence of operating conditions on the dense gas precipitation of model proteins. *Journal of Chemical Technology & Biotechnology,* 75**,** 29-41.

Thiering, R., Dehghani, F., Dillow, A. & Foster, N. R. 2000b. Solvent effects on the controlled dense gas precipitation of model proteins. *Journal of Chemical Technology & Biotechnology,* 75**,** 42-53.

Thorat, A. A. & Dalvi, S. V. 2012. Liquid antisolvent precipitation and stabilization of nanoparticles of poorly water soluble drugs in aqueous suspensions: Recent developments and future perspective. *Chemical Engineering Journal,* 181–182**,** 1-34.

Ting, T.-Y., Gonda, I. & Gipps, E. 1992. Microparticles of Polyvinyl Alcohol for Nasal Delivery. I. Generation by Spray-Drying and Spray-Desolvation. *Pharmaceutical Research,* 9**,** 1330-1335.

Torino, E., De Marco, I. & Reverchon, E. 2010. Organic nanoparticles recovery in supercritical antisolvent precipitation. *The Journal of Supercritical Fluids,* 55**,** 300-306.

Traub, P. & Stephan, K. 1990. High-pressure phase equilibria of the system CO2—water—acetone measured with a new apparatus. *Chemical Engineering Science,* 45**,** 751-758.

Tuğcu-Demiröz, F., Acartürk, F., Takka, S. & Konuş-Boyunağa, Ö. 2007. Evaluation of alginate based mesalazine tablets for intestinal drug delivery. *European Journal of Pharmaceutics and Biopharmaceutics,* 67**,** 491-497.

Tyle, P. 1993. Tactile Pattern RecognitionEffect of size, shape and hardness of particles in suspension on oral texture and palatability. *Acta Psychologica,* 84**,** 111-118.

Urbańska, J., Karewicz, A. & Nowakowska, M. 2014. Polymeric delivery systems for dexamethasone. *Life Sciences,* 96**,** 1-6.

Uzun, İ. N., Sipahigil, O. & Dinçer, S. 2011. Coprecipitation of Cefuroxime Axetil–PVP composite microparticles by batch supercritical antisolvent process. *The Journal of Supercritical Fluids,* 55**,** 1059-1069.

Van Den Mooter, G., Wuyts, M., Blaton, N., Busson, R., Grobet, P., Augustijns, P. & Kinget, R. 2001. Physical stabilisation of amorphous ketoconazole in solid dispersions with polyvinylpyrrolidone K25. *European Journal of Pharmaceutical Sciences,* 12**,** 261-269.

Van Der Plancken, I., Van Loey, A. & Hendrickx, M. E. 2006. Effect of heat-treatment on the physico-chemical properties of egg white proteins: A kinetic study. *Journal of Food Engineering,* 75**,** 316-326.

Vehring, R. 2008. Pharmaceutical Particle Engineering via Spray Drying. *Pharmaceutical Research,* 25**,** 999-1022.

Velaga, S., Berger, R. & Carlfors, J. 2002. Supercritical Fluids Crystallization of Budesonide and Flunisolide. *Pharmaceutical Research,* 19**,** 1564-1571.

Velaga, S. P., Bergh, S. & Carlfors, J. 2004. Stability and aerodynamic behaviour of glucocorticoid particles prepared by a supercritical fluids process. *European Journal of Pharmaceutical Sciences,* 21**,** 501-509.

Vladisavljević, G. T. 2012. Encapsulation application. *In:* DRIOLI, E. & GIORNO, L. (eds.) *Encyclopedia of Membranes.*

Wang, W., Liu, G., Wu, J. & Jiang, Y. 2013. Co-precipitation of 10-hydroxycamptothecin and poly (l-lactic acid) by supercritical CO2 anti-solvent process using dichloromethane/ethanol co-solvent. *The Journal of Supercritical Fluids,* 74**,** 137-144.

Wang, Y., Wang, Y., Yang, J., Pfeffer, R., Dave, R. & Michniak, B. 2006. The application of a supercritical antisolvent process for sustained drug delivery. *Powder Technology,* 164**,** 94-102.

Weidner, E. 2009. High pressure micronization for food applications. *The Journal of Supercritical Fluids,* 47**,** 556-565.

Winters, M. A., Knutson, B. L., Debenedetti, P. G., Sparks, H. G., Przybycien, T. M., Stevenson, C. L. & Prestrelski, S. J. 1996. Precipitation of proteins in supercritical carbon dioxide. *Journal of Pharmaceutical Sciences,* 85**,** 586-594.

Wong, T. W. 2011. Alginate graft copolymers and alginate–co-excipient physical mixture in oral drug delivery. *Journal of Pharmacy and Pharmacology,* 63**,** 1497-1512.

Yang, Y. P., Lotta, L., Beutner, G., Li, X. & Schor, N. F. 2015. Induction of Expression of p75 Neurotrophin Receptor Intracellular Domain Does Not Induce Expression or Enhance Activity of Mitochondrial Complex II. *Oxidative Medicine and Cellular Longevity.*

Yeo, S.-D., Lim, G.-B., Debendetti, P. G. & Bernstein, H. 1993. Formation of microparticulate protein powder using a supercritical fluid antisolvent. *Biotechnology and Bioengineering,* 41**,** 341-346.

Yeoman, A. D., Westbrook, R. H., Zen, Y., Bernal, W., Al-Chalabi, T., Wendon, J. A., O'grady, J. G. & Heneghan, M. A. 2014. Prognosis of acute severe autoimmune hepatitis (AS-AIH): The role of corticosteroids in modifying outcome. *Journal of Hepatology,* 61**,** 876-882.

Yi, J., Lam, T. I., Yokoyama, W., Cheng, L. W. & Zhong, F. 2015. Beta-carotene encapsulated in food protein nanoparticles reduces peroxyl radical oxidation in Caco-2 cells. *Food Hydrocolloids,* 43**,** 31-40.

References

Yoon, J. H., Chun, M. K., Hong, W. H. & Lee, H. 1993. High-pressure phase equilibria for carbon dioxide-methanol-water system: experimental data and critical evaluation of mixing rules. *Industrial & Engineering Chemistry Research,* 32**,** 2881-2887.

York, P., Kompella, U. B. & Shekunov, B. Y. 2002. *Supercritical Fluid Technology for Drug Product Development,* New York: Marcel Dekker.

Yoshikawa, H., Hirano, A., Arakawa, T. & Shiraki, K. 2012. Effects of alcohol on the solubility and structure of native and disulfide-modified bovine serum albumin. *International Journal of Biological Macromolecules,* 50**,** 1286-1291.

Zhang, Q., Han, Y., Wang, W.-C., Zhang, L. & Chang, J. 2009. Preparation of fluorescent polystyrene microspheres by gradual solvent evaporation method. *European Polymer Journal,* 45**,** 550-556.

Zhou, T., Zhou, P., Hua, H. & Liu, X. 2015. Beneficial Effects and Safety of Corticosteroids Combined with Traditional Chinese Medicine for Pemphigus: A Systematic Review. *Evidence-Based Complementary and Alternative Medicine,* 2015**,** 9.

List of symbols

AC:	acetone
ASES:	Aerosol Solvent Extraction System
BSA:	Bovine serum albumin
C:	concentration of solute
CHF:	chloroform
CO_2:	carbon dioxide
D:	nozzle diameter
DLS:	dynamic laser scattering
DMSO:	dimethylsulfoxide
DSC:	differential scanning calorimeter
ELAS:	Expanded Liquid Antisolvent
EMP:	expanded microparticles
EtOH:	ethanol
FTIR:	Fourier transform infrared
H:	enthalpy
HPLC:	high performance liquid chromatography
MCP:	mixture critical point
m.d.:	particle mean diameter
MP:	microparticles
Mw:	molecular weight
NMP:	N-methyl-2-pyrrolidone
NP:	nanoparticles
Oh:	Ohnesorge
P:	pressure
PGSS:	Precipitation from Gas Saturated Solution
PSD:	particle size distribution
PVP:	polyvinyl pirrolidone
Re:	Reynolds number
RESS:	Rapid Expansion of Supercritical Solutions
RESOLV:	Rapid Expansion of a Supercritical Solution into a liquid Solvent
SAA:	Supercritical Assisted Atomization
SAILA:	Supercritical Assisted Injection in a Liquid Antisolvent
SAS:	Supercritical Antisolvent
SAS-EM:	Supercritical AntiSolvent with Enhanced Mass transfer
$scCO_2$:	supercritical carbon dioxide
SCF:	supercritical fluid
s.d.:	standard deviation
SEDS:	Solution Enhanced Dispersion by Supercritical fluids

SEM:	Scanning Electron Microscope
T:	temperature
ν_0:	laser frequency
V:	fluid velocity
VLE:	vapor liquid equilibria
x:	composition
We:	Weber
μ:	viscosity of CO_2-solution mixture
ρ:	fluid density
σ:	surface tension
τ_{jb}:	time of jet break-up
τ_{ts}:	time of surface tension vanishing